

AN ABSTRACT OF THE DISSERTATION OF

Aaron James Reynolds for the degree of Doctor of Philosophy in Nuclear Engineering presented on November 3, 2020.

Title: A Multilevel Nonlinear Projective Method for Circulating Fuel Reactor Kinetics

Abstract approved: _____

Todd S. Palmer

Circulating fuel reactor (CFR) kinetics are characterized by delayed neutron precursor (DNP) drift in addition to the neutronic and thermal hydraulic phenomena typical of other reactor types. This environment can be computationally challenging to model, given that the multiphysics phenomena generally have non-linear interdependencies requiring the use of iterative solution techniques. In this work, a multilevel nonlinear projective method in RZ geometry is presented which calculates a transport solution to the CFR kinetics problem. This approach offers computational savings by coupling the multiphysics phenomena to low-order quasi-diffusion equations. The method is verified with the method of manufactured solutions. A residual-balanced algorithm for multilevel coupling is presented and shown to mitigate oversolving when compared to a standard fixed point iteration scheme. Transient and steady-state simulations demonstrating the influence of

the DNP drift phenomena are shown, as well as a comparison to results from the Molten Salt Reactor Experiment. The importance of capturing transport effects when simulating channel-type CFRs is also investigated, and are found to produce average variations of 2-3% in the two-group fluxes when compared to the P_1 approximation.

©Copyright by Aaron James Reynolds
November 3, 2020
All Rights Reserved

A Multilevel Nonlinear Projective Method for Circulating Fuel
Reactor Kinetics

by
Aaron James Reynolds

A DISSERTATION

submitted to

Oregon State University

in partial fulfillment of
the requirements for the
degree of

Doctor of Philosophy

Presented November 3, 2020
Commencement June 2021

Doctor of Philosophy dissertation of Aaron James Reynolds presented on
November 3, 2020.

APPROVED:

Major Professor, representing Nuclear Engineering

Head of the School of Nuclear Science and Engineering

Dean of the Graduate School

I understand that my dissertation will become part of the permanent collection of Oregon State University libraries. My signature below authorizes release of my dissertation to any reader upon request.

Aaron James Reynolds, Author

ACKNOWLEDGEMENTS

I would like to thank Muriel Condon, who I love dearly, for her bottomless encouragement and patient reminders to maintain my mental and physical health throughout this process. 10/10, would move from Montana to Oregon to Tennessee with you again, and without hesitation.

My parents, James F. Reynolds and Jana A. H. Reynolds, have provided constant support for my pursuits and cathartic conversations on the politics of this fraught era. I hope we can talk idly about the weather sometime soon.

I have benefited from the dogged efforts of many current and former public school teachers who deserve more recognition for their dedication than I can give here, and in general. Mrs. Kimball, Mrs. Chambers, Mrs. Begler, Mrs. Holland, Mrs. Wilkison, Mrs. McCauley, Mrs. Egbert, Mrs. Schluter, Mr. McGinley, Mr. Peterson, Mr. Chart (a math teacher, can you believe that?), Dr. Neiffer, and Señor Lyng: your roles in my education were vital, and I value what you have given me.

Tom Pedersen, Montana Teacher of the Year, wolverine enthusiast, and fount of Crosby, Stills, and Nash trivia, who, in stride, bravely takes high school students into the Glacier and Yellowstone National Parks for days at a time to commune with grizzly bears and wolves, continues to be a role model I emulate in all things but hairline. Perhaps most impressive, Tom, is that you made learning science from an overhead projector just as enchanting. The wilderness I work in now has more bugs than bears, but the curiosity and value system you instilled are still

hard at work.

Dr. Malgo Peszynska outmatched the patience of stone answering the uncountably infinite questions of a fool-hearty engineer exploring the strange new world of numerical analysis. I like to think I have come out the other side a more competent and careful explorer, maybe even a computational scientist, thanks in large part to your efforts.

My advisor, Dr. Todd Palmer, has been a tireless champion of good science and balance (in life and conservation equations). I cannot thank you enough for enabling Muriel and I to pursue our educational goals simultaneously, and for encouraging your students to be kind and inclusive as much as hard-working and insightful. If I can muster a fifth of your intellect and an ounce of your wit, I'll be equally fit for a successful career in reactor physics or late-night television.

Radiation Transport and Reactor Physics research group, where you at? You all are the best. I cannot believe how fortunate I've been in having the camaraderie of so many incredible people. I hope our happy hours continue ad infinitum.

Vote.

TABLE OF CONTENTS

	<u>Page</u>
1 Introduction	1
1.1 A brief history of CFRs	2
1.2 Design challenges	4
1.3 Modeling CFR neutron kinetics	6
1.3.1 Differential scattering cross section	6
1.3.2 Angular neutron emission energy spectrum	7
1.3.3 Delayed neutron precursor drift	8
1.4 Research objectives	10
2 Literature Review	12
2.1 Multigroup diffusion CFR methods	13
2.1.1 Cinsf1D [19]	14
2.1.2 Yamamoto et al. [20]	16
2.1.3 DYN1D-MSR and DYN3D-MSR [21, 22]	17
2.1.4 Nicolino et al. [25]	18
2.1.5 Zhang et al. [26]	19
2.1.6 Kópházi et al. [27]	21
2.1.7 Aufiero et al. [29]	23
2.1.8 Fiorina et al. [31]	24
2.1.9 MOREL [33]	26
2.1.10 Moltres [34]	27
2.1.11 Remarks	28
2.2 Quasi-diffusion [36, 37, 38]	29
2.3 Multilevel methods	31
3 Methods	34
3.1 Multigroup neutron transport	39
3.1.1 Time discretization	39
3.1.2 Angular discretization	41
3.1.3 Spatial discretization	44
3.1.4 Starting angle equation	47
3.1.5 Solving procedure	49
3.2 Multigroup quasi-diffusion	51
3.2.1 Transport coupling	54

TABLE OF CONTENTS (Continued)

	<u>Page</u>
3.2.2 Integrating factor	55
3.2.3 Discretization	57
3.2.4 Linear system	61
3.3 Effective low-order transport	64
3.3.1 One-group QD discretization	67
3.3.2 DNP balance discretization	70
3.3.3 Energy balance discretization	75
3.3.4 Linear system	80
3.4 Steady state formulation	82
3.5 Multilevel algorithms	84
3.6 Implementation details	86
4 Results and Discussion	90
4.1 Method of manufactured solutions verification	90
4.1.1 Neutron transport	92
4.1.2 Quasi-diffusion	100
4.1.3 Heat transfer	107
4.1.4 DNP balance	109
4.2 Residual balance parameter study	112
4.2.1 Transient	114
4.2.2 Steady state	119
4.2.3 Remarks	123
4.3 Transient simulation	123
4.3.1 Startup	125
4.3.2 Steady-state eigenvalue	130
4.4 Steady state simulation of the Molten Salt Reactor Experiment	131
4.4.1 Modeling parameters	132
4.4.2 Loss of reactivity from DNP flow	136
4.4.3 Isothermal eigenvalue	141
4.4.4 Critical system	142
4.4.5 Transport effects	151
4.4.6 Remarks	163

TABLE OF CONTENTS (Continued)

	<u>Page</u>
5 Conclusion	165
5.1 Future work	167
Appendix	180
A Quadrature Set	181
B Simple Corner Balance	182
C Starting Angle Operators	191
D Group Constant Generation with SCALE	194
E QD Boundary Conditions with P_1 Approximation	196

LIST OF FIGURES

<u>Figure</u>		<u>Page</u>
1.1 INOR-8 irradiated in MSRE (left) and unirradiated (right). The irradiated specimen shows significant signs of embrittlement. Tellurium was found to be the cause. [13]	5	
1.2 Differential scattering cross section for stationary fuel. [15]	6	
1.3 Angular neutron emission with stationary nucleus.	7	
1.4 Angular neutron emission with nucleus moving to the right.	8	
1.5 The fission process. [15]	9	
2.1 Reactivity lost through precursor drift. Left: pump start-up event. Right: pump shutdown event. Fig. 9 from [22].	18	
2.2 Power during natural circulation transient. Fig. 9 from [27].	22	
2.3 Comparison of OpenFOAM [29], COMSOL [31], TUDelft [27] codes. Figure 13 from [29].	25	
2.4 Diagram of a multilevel method in 1D.	32	
3.1 Direction of flight $\hat{\Omega}$	36	
3.2 Ordinates in one octant are displayed. Ordinates on different levels are distinguished by color.	42	
3.3 Subcell discretization on a cell (i, j)	44	
3.4 Beginning positions for spatial mesh sweeps depending on the signs of μ_{pq} and ξ_p	50	
3.5 Relationship between the simple corner balance and quasi-diffusion notation. The simple corner balance notation is in orange with uppercase (I, J) indices. The quasi-diffusion notation is in green with lowercase (i, j) indices. For example, a quantity at $(i, j) =$ $(3, 2)$ is consistent with position 4 of $(I, J) = (2, 1)$ in the simple corner balance notation.	55	
3.6 An $N \times M$ mesh. Unknowns are marked with a circle.	62	

LIST OF FIGURES (Continued)

<u>Figure</u>		<u>Page</u>
3.7 Boundary DNP fluxes for a row i . J is the total number of axial cells.		74
3.8 Implementation of discretized boundary conditions for the cell at (I, J) when $\vec{u} > 0$.		78
3.9 Ghost cell definitions for energy flux calculations near problem boundaries.		79
4.1 Simple corner balance convergence study for isotropic MMS problem. Errors are measured from the scalar fluxes.		95
4.2 Simple corner balance convergence study for isotropic MMS problem. Errors are measured from the angular fluxes with direction cosines $(\xi_p, \mu_{pq}) = (-0.971638, -0.167213)$.		96
4.3 Simple corner balance convergence study for anisotropic MMS problem. Errors are measured from the scalar fluxes.		99
4.4 QD convergence study for MMS problems. Errors are measured with the 2-norm from the scalar fluxes and currents.		104
4.5 QD convergence study for MMS problems. Errors are measured with the ∞ -norm from the scalar fluxes and currents.		105
4.6 Heat transfer convergence study for MMS problem.		109
4.7 DNP balance convergence study for MMS problem.		112
4.8 Transient solve times [s] for a variety of balance factors τ .		114
4.9 MGHOST iterations in a transient solve for a variety of balance factors τ .		115
4.10 MGLOQD iterations in a transient solve for a variety of balance factors τ .		116
4.11 ELOT iterations in a transient solve for a variety of balance factors τ .		117
4.12 Transient solve times [s] for a variety of balance factors τ without the interrupt event.		118
4.13 Steady state solve times for a variety of balance factors τ .		119

LIST OF FIGURES (Continued)

<u>Figure</u>	<u>Page</u>
4.14 MGHOT iterations in a transient solve for a variety of balance factors τ .	120
4.15 MGLOQD iterations in a transient solve for a variety of balance factors τ .	120
4.16 ELOT iterations in a transient solve for a variety of balance factors τ .	121
4.17 Residuals for case with ($\tau_{ELOT} = 0$, $\tau_{MGLOQD} = 0$).	122
4.18 Residual behavior for case with ($\tau_{ELOT} = 1$, $\tau_{MGLOQD} = 1E-2$).	122
4.19 Thermal group ν	125
4.20 Core power during startup phase.	126
4.21 Core temperatures at 8.55 s.	126
4.22 Multigroup fluxes at 8.55 s.	127
4.23 Core temperatures at 12.15 s	127
4.24 DNP concentration at 12.15 s for longest-lived (left) and shortest-lived (right) groups.	128
4.25 Multigroup fluxes at 21.75 s	129
4.26 DNP concentration at 21.75 s for longest-lived (left) and shortest-lived (right) groups.	129
4.27 DNP concentration at 53.55 s for longest-lived (left) and shortest-lived (right) groups.	130
4.28 Core power out to 10 minutes.	131
4.29 As-modeled MSRE axis-symmetric geometry. The dark and light regions denote fuel and graphite, respectively. The leftmost channel, which falls on the axis of symmetry, is half width. The control rod, not pictured, would be between the first and second (from the left) fuel channels.	134
4.30 Fast (left) and thermal (right) fluxes with control rod fully withdrawn.	136

LIST OF FIGURES (Continued)

<u>Figure</u>	<u>Page</u>
4.31 Temperature distribution with control rod fully withdrawn.	137
4.32 DNP concentrations for groups 1 and 2 with control rod fully withdrawn.	138
4.33 DNP concentrations for groups 3 and 4 with control rod fully withdrawn.	138
4.34 DNP concentrations for groups 5 and 6 with control rod fully withdrawn.	139
4.35 Fast and thermal fluxes with control rod inserted to 60 cm.	143
4.36 Temperature distribution with control rod inserted to 60 cm.	143
4.37 DNP concentrations for groups 1 and 6 with control rod inserted to 60 cm.	144
4.38 Comparison of temperatures in hottest graphite region (right) and closest fuel channel (left).	146
4.39 Comparison of fast (left) and thermal (right) midplane fluxes	148
4.40 Comparison of fast (left) and thermal (right) centerline fluxes.	149
4.41 Absolute difference in fast and thermal E_{zz} for isothermal calculation.	152
4.42 Absolute difference in fast and thermal E_{rr} for isothermal calculation.	153
4.43 Absolute difference in fast and thermal E_{rz} for isothermal calculation.	153
4.44 Percent difference in isothermal fast and thermal fluxes relative to case with transport coupling.	154
4.45 Percent difference in temperature distribution relative to case with transport coupling.	155
4.46 Percent difference in DNP concentrations for groups 1 and 2 relative to case with transport coupling.	157
4.47 Percent difference in DNP concentrations for groups 3 and 4 relative to case with transport coupling.	157

LIST OF FIGURES (Continued)

<u>Figure</u>	<u>Page</u>
4.48 Percent difference in DNP concentrations for groups 5 and 6 relative to case with transport coupling.	158
4.49 Absolute difference in fast and thermal E_{zz} for critical configuration.	159
4.50 Absolute difference in fast and thermal E_{rr} for critical configuration.	159
4.51 Absolute difference in fast and thermal E_{rz} for critical configuration.	160
4.52 Percent difference in fast and thermal fluxes relative to case with transport coupling for critical configuration.	161
4.53 Left: percent difference in thermal flux around control rod for critical configuration. Right: thermal fluxes around control rod at core midplane.	162
4.54 Midplane (left) and centerline (right) fluxes as calculated with diffusion and transport-derived Eddington factors and boundary conditions.	163

LIST OF TABLES

Table	Page
3.1 Descriptions of the linear operators in Eq. (3.30).	46
3.2 Breakdown of unknowns in multigroup quasidiffusion solve.	62
3.3 Equations used to form the linear system used in solving the multi-group QD level. N_{eq} is the number of times an equation is used in the linear system.	63
3.4 $\Gamma(\theta)$ definitions for a variety of methods The definition for the min-mod fuction is given in Eq. (3.93). Reproduced from [56].	72
3.5 Breakdown of unknowns in effective low-order transport solve. N and M are the number of axial and radial cells and N_D is the number of delayed neutron precursor groups.	
.	80
4.1 Convergence critieria.	90
4.2 Meshes for isotropic MMS mesh refinement study, where $h_s = 0.1$ cm, and $h_t = 1E-4$ s. All simulations use $Z = 1.0$ cm, $R = 1.0$ cm, and $T = 1E-4$ s.	94
4.3 Nuclear data used on the meshes in Table 4.2. c is the parameter that appears in Eq. (4.8a).	94
4.4 Meshes for anisotropic MMS convergence study, where $h_s = 10$ cm, and $h_t = 1E-4$ s. All meshes use $Z = 100$ cm, $R = 100$ cm, and $T = 1E-4$ s.	98
4.5 Nuclear data used on the meshes in Table 4.4.	99
4.6 QD MMS coefficients.	101
4.7 Meshes used in QD MMS convergence study for $C = 0$, where $h_s = 10$ cm and $h_t = 1$ s. All simulations use $Z = 100.0$ cm, $R = 100.0$ cm, and $T = 1.0$ s.	103
4.8 Meshes used in QD MMS convergence study for $C = 1$, where $h_s = 10$ cm and $h_t = 1$ s. All simulations use $Z = 100.0$ cm, $R = 100.0$ cm, and $T = 1.0$ s.	103

LIST OF TABLES (Continued)

Table	Page
4.9 Nuclear data used on the meshes in Tables 4.7 and 4.8.	104
4.10 Convergence rates in the ∞ -norm.	106
4.11 Meshes used in heat transfer MMS convergence study where $h_s = 0.2$ cm and $h_t = 0.2$ s. All simulations use $Z = 1.0$ cm, $R = 1.0$ cm, and $T = 1.0$ s.	108
4.12 Data used on the meshes in Table 4.11.	108
4.13 Meshes used in DNP balance MMS convergence study where $h_s = 0.1$ cm and $h_t = 0.2$ s. All simulations use $Z = 1.0$ cm, $R = 1.0$ cm, and $T = 0.2$ s.	111
4.14 Data used on the meshes in Table 4.13.	111
4.15 Balance factors used in parameter study.	113
4.16 Mesh parameters for residual balance parameter study.	113
4.17 Average solve times for transient case with ($\tau_{ELOT}=1$, $\tau_{MGLOQD}=1$). .	117
4.18 Scattering cross sections for homogeneous problem.	123
4.19 Group constants for homogeneous problem.	124
4.20 Geometry and heat transfer parameters for homogeneous problem. .	124
4.21 Mesh parameters for homogeneous transient.	124
4.22 k_{eff} at steady-state power of 44.83 MW.	130
4.23 As-modeled MSRE parameters.	132
4.24 As-modeled control rod geometry.	134
4.25 As-modeled MSRE material compositions.	135
4.26 ORNL DNP parameters from Haubenreich et al. [64].	135
4.27 Mesh parameter for MSRE simulations.	135
4.28 Reactivity loss from DNP drift. The change in reactivity $\Delta\rho$ is measured relative to the system with $\beta = 0$	140

LIST OF TABLES (Continued)

<u>Table</u>	<u>Page</u>
4.29 Reactivity loss from DNP drift in the MSRE at steady state as calculated by MOST participants and reported experimentally. Adapted from Table 1 in Delpech et al. [17].	140
4.30 Reactivity loss from DNP drift with and without plena modeling as reported by Prince et al. [24].	141
4.31 Isothermal eigenvalues as calculated in this work and by some MOST participants. Adapted from Table 6 in Delpech et al. [17]. Delpech et al. do not identify which decay data was used for these calculations. ENDF decay data was used in QuasiMolto.	142
4.32 Variations in as-modeled MSRE parameters. All models feature 6 DNP groups and 2 neutron energy groups.	145
4.33 Midplane peak fast to thermal flux ratios.	147
4.34 Centerline peak fast to thermal flux ratios.	150
4.35 Isothermal eigenvalues calculated for transport and diffusion simulations.	155
4.36 Reactivity loss from DNP drift using the P1 approximation. The change in reactivity $\Delta\rho$ is measured relative to the system with $\beta = 0$	156
4.37 Eigenvalues of transport and diffusion simulations for approximately critical case.	162
A.1 Level-symmetric S_{12} quadrature set in one octant.	181

LIST OF ALGORITHMS

<u>Algorithm</u>	<u>Page</u>
3.1 Fixed-point iteration for ELOT problem	81
3.2 Power iteration for steady state ELOT problem	84
3.3 Residual-balanced fixed-point iteration for transient solve of multi-level problem.	88
3.4 Residual-balanced fixed-point iteration for steady-state solve of multilevel problem.	89

1 Introduction

Fuel mobility distinguishes circulating fuel reactors (CFRs) from solid fuel reactors (SFRs). In an SFR, such as a boiling water or pressurized water reactor, stationary nuclear fuel generates heat as a product of the fission process. A coolant passes over the fuel and transports energy through a loop where some work is performed. In a CFR, the fuel is not stationary. In some cases, the coolant and fuel are homogeneously mixed in a single fluid traveling the same loop. In others, the fuel and the coolant are separate fluids traveling distinct loops. The distinguishing trait for both is the same - the fuel *moves*.

Three major subcategories exist within the CFR family: molten salt reactors (MSRs), aqueous homogeneous reactors, and liquid metal fueled reactors. They differ from one another by the fluid in which the fuel is entrained. Depending on the particular design, CFRs can have a number of benefits as described by Serp et al. [1]:

- low operating pressure
- actinide burning
- online fission product removal
- ability to drain core inventory
- no fuel fabrication
- online refuelling
- breeder potential
- minimal waste production

There are a number of challenges to the development of CFRs, many related

to materials' considerations that will be mentioned briefly. This work, however, focuses on challenges related to the modeling and simulation of CFR neutron kinetics. Fuel movement introduces delayed neutron precursor (DNP) drift, a phenomena incompatible with conventional reactor analysis tools (i.e. those developed for SFRs). This motivates the development of models and methods to simulate CFRs.

In the remainder of this section, a background on molten salt reactors and circulating fuel reactor kinetics is presented, followed by the research objectives of this work. Section 2 contains a review of past efforts to deterministically model circulating fuel reactors using neutron diffusion theory. In Section 3, a novel method to deterministically model circulating fuel reactor kinetics with neutron transport theory is presented. Results verifying the implementation of the described method, modeling the steady-state behaviour of the Molten Salt Reactor Experiment (MSRE), and investigating the importance of capturing transport phenomena in the modeled problems are presented in Section 4. Finally, concluding remarks are contained in Section 5.

1.1 A brief history of CFRs

Oak Ridge National Laboratory (ORNL) built and operated the first CFR, the Aircraft Reactor Experiment (ARE), in the early 1950's. The fuel, enriched to 93.4% ^{235}U , was contained in molten $\text{NaF-ZrF}_4\text{-UF}_4$ and moderated by BeO blocks [2, 3, 4]. The ARE operated for 100 hours at a maximum temperature and power

of 1600°F and 2.5MW, respectively [5]. The prospects of a nuclear aircraft were abandoned in 1956 when confronted by the challenge of shielding a flight crew, the development of ICBMs that conventionally satisfied the goal of a nuclear aircraft, and budgetary concerns [3].

Shortly after, and utilizing much of the expertise and technology developed during the ARE, ORNL Director Alvin Weinberg began the MSRE to explore the use of CFRs for commercial power generation [6]. The MSRE used “high enriched” [7] uranium fuel, contained within molten LiF-BeF₂-ZrF₄-ThF₄-UF₄, and a graphite moderator [3]. Alvin Weinberg details operation of the MSRE in his book *The First Nuclear Era: The Life and Times of a Technological Fixer*:

“The molten-salt reactor began operation early in 1966 and achieved its maximum power (limited by the size of the air-cooled ultimate heat exchanger) of 7,500 kilowatts in March of that year. It continued to operate remarkably smoothly, though with interruptions for maintenance, until December 1969, when its operation was terminated so that funds could be diverted to the development of more-advanced molten-salt systems. We were delighted with the MSRE. Here we had a high-temperature fluid-fuel reactor that operated reliably and, even in the primitive embodiment represented by the MSRE, had remarkably low fuel costs.”

Despite the enthusiasm of those involved, as of October 2020, the MSRE was the last CFR to be built and operated, although ORNL and others continued to

develop MSR concepts such as the Denatured Molten Salt Reactor and the Molten Salt Breeder Reactor [8, 9].

CFRs gained renewed attention in the early 2000s when MSR concepts were identified by an international forum as Generation IV reactors, characterized by offering potential advancements in (1) sustainability, (2) economics, (3) safety and reliability, and (4) proliferation resistance physical protection [10]. Currently, a number of organizations are developing CFR concepts and technology (most within the MSR subcategory). These organizations include, among others: Thor-Con, Thorencos, Flibe Energy, Terrestrial Energy, GEMSTAR, ORNL, MIT, UC Berkeley, Transatomic Power Corporation (now defunct, but their design work is available to the public), and TerraPower [11].

1.2 Design challenges

Abram and Ion [12] identify a number of challenges to the technological readiness of CFRs and, in particular, MSR concepts. Some of these challenges were recognized during the ARE and the MSRE, as seen in Figure 1.1.

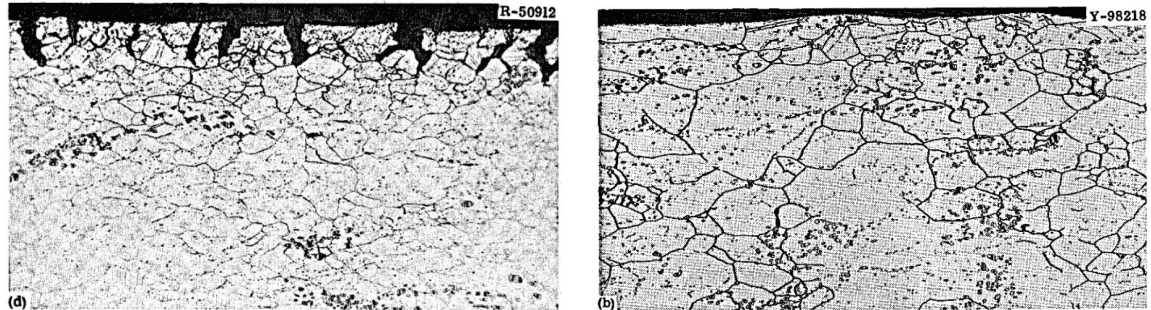


Figure 1.1: INOR-8 irradiated in MSRE (left) and unirradiated (right). The irradiated specimen shows significant signs of embrittlement. Tellurium was found to be the cause. [13]

In many CFR designs, piping and vessel materials are in direct contact with corrosive, high temperature fluids emitting high levels of radiation. Materials or processes must be identified that are capable of withstanding or mitigating these conditions for extended intervals, if not the lifetime of the reactor. Online refueling and fission product removal capabilities require extensive chemical processing equipment capable of enduring comparable conditions to those found in the core. Additionally, regulatory framework for safety qualification of a reactor with the dual purposes of producing power and processing fuel material must be established [1]. In short, material and safety considerations need to be addressed and progress is on-going [1].

Besides challenges to technological readiness, another question regarding a fundamental step in the design process must be considered: how does one accurately model and simulate CFR physics? The remainder of this work considers answers to this question with a particular focus on neutron kinetics.

1.3 Modeling CFR neutron kinetics

Wooten and Powers [14] describe three impacts that fuel movement has on neutron kinetics: (1) changes to the differential scattering cross section, (2) changes to the angular neutron emission energy spectrum, and (3) DNP drift. To accurately model CFR neutron kinetics, the effects of DNP drift must be considered.

1.3.1 Differential scattering cross section

Consider an illustration of the differential scattering cross section $\sigma_s(\hat{\Omega} \rightarrow \hat{\Omega}')$ in Figure 1.2.



Figure 1.2: Differential scattering cross section for stationary fuel. [15]

Here, an incident neutron with direction $\hat{\Omega}$ scatters off a stationary nucleus into direction $\hat{\Omega}'$. For a given neutron beam intensity, the differential scattering cross section $\sigma_s(\hat{\Omega} \rightarrow \hat{\Omega}')$ is the proportionality describing the rate of neutrons scattering from direction $\hat{\Omega}$ to direction $\hat{\Omega}'$.

Now, consider the same scenario, but with a nucleus having some non-zero velocity. This velocity, in most scenarios, will result in a departing direction $\hat{\Omega}^*$ for

the neutron where $\hat{\Omega}^* \neq \hat{\Omega}'$. Due to this velocity, attributable to fuel movement, a new differential scattering cross section $\bar{\sigma}_s(\hat{\Omega} \rightarrow \hat{\Omega}')$ is required to describe the rate of neutrons scattering from direction $\hat{\Omega}$ to direction $\hat{\Omega}'$.

In the context of the CFRs under consideration for this work, however, the neutron speed (2200 m/s for a thermal neutron) is typically three orders of magnitude larger than the nucleus speed (on the order of 1 m/s [16, 8, 9]). As such, one can assume $\hat{\Omega}^* \approx \hat{\Omega}'$ and consider any changes to the differential scattering cross section negligible [15, 14].

1.3.2 Angular neutron emission energy spectrum

Consider a stationary nucleus emitting two mono-energetic neutrons in opposite directions, $-\hat{\Omega}$ and $\hat{\Omega}$, as in Figure 1.3.

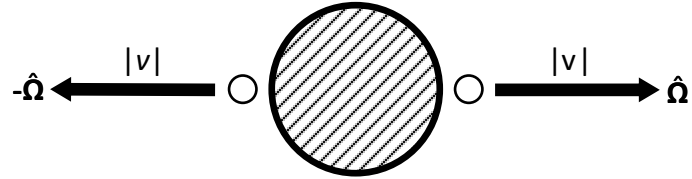


Figure 1.3: Angular neutron emission with stationary nucleus.

Each neutron has speed $|v|$. Now consider Figure 1.4, where the nucleus is moving with a speed $|v_N|$ in the direction $\hat{\Omega}$.

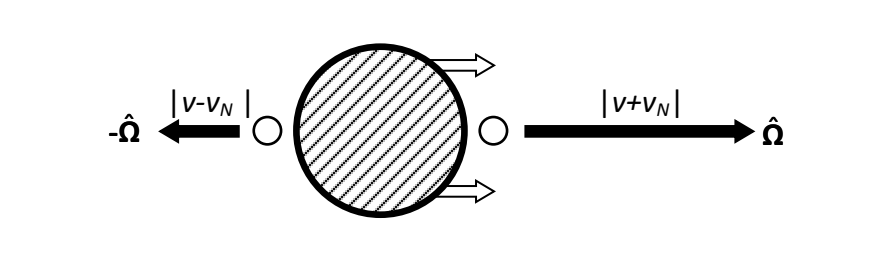


Figure 1.4: Angular neutron emission with nucleus moving to the right.

In this scenario, the neutrons are emitted from a moving reference frame, a context that must be considered. Using classical mechanics, the left and right neutrons are found to have velocities $v - v_N$ and $v + v_N$, respectively. As velocity can be related to kinetic energy with $\frac{1}{2}mv^2$, this can be recognized as this as a change in the angular neutron emission energy spectrum from the stationary nucleus case.

Once again, however, by noting that $|v| \gg |v_N|$ in the case of CFRs, one can consider these effect negligible as $v - v_N \approx v \approx v + v_N$ [15, 14].

1.3.3 Delayed neutron precursor drift

The final effect to consider, and the most important for this work, is DNP drift. To analyze the neutron kinetics of a fission-based system, one must know the neutron flux distribution. In a fission event, depicted in Figure 1.5, an unstable nucleus splits, producing fission products, neutrons, energy, and some subatomic particles [15]. A fraction of the time, a fission product takes the form of a DNP. A DNP has an unstable nucleus which will, after a delay, undergo radioactive decay and

emit a neutron.

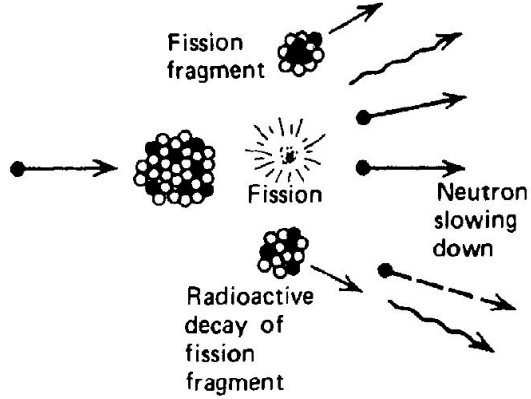


Figure 1.5: The fission process. [15]

In a fission-based nuclear reactor, then, neutrons are generally produced in two ways: (1) promptly, through a fission event, and (2) after a delay following a fission event, through the radioactive decay of DNP s. In an SFR, the DNP s will remain close to the initiating fission event, and it is assumed that the fission and DNP decay events occur, and contribute to the neutron flux, in the same location.

In a CFR, this is not the case. After the initiating fission event in, say, Location A, DNP s are swept away with the movement of the fuel. The DNP s will eventually decay in some Location B. For a CFR, a single fission event will lead to neutron flux contributions in both Locations A and B.

In the previous two cases, concerning changes to the differential scattering cross section and angular neutron emission energy spectrum, the impact of the effects was dependent on the magnitude ratio of the neutron and flow velocities. Here, however, the flow velocity with must be considered respect to the radioactive decay

constant or half-life of the DNPs. The first DNP group, for example, has a half-live of 55 seconds [15]. With a flow velocity on the order of 1 m/s, these precursors have an overwhelming chance to be displaced and alter the neutron flux. Because of this, and the vital role DNPs play in the control and operation of nuclear reactors [15], the DNP drift phenomena must be accounted for.

1.4 Research objectives

Having established the physical basis motivating computational tools for MSRs, the specific objectives of this research are presented.

1. Model and simulate time- and space-dependent CFR physics using neutron transport theory
 - (a) Implement in RZ cylindrical geometry
 - (b) Implement for an arbitrary number of neutron energy and precursor groups
2. Implement multiphysics coupling using a quasi-diffusion (QD) based, multi-level method
3. Validate results against available experimental data from the MSRE

The first two objectives are novelties of this work. Objective (1) is notable as past deterministic efforts to model CFR physics with full time and space dependence have utilized neutron diffusion theory. Using a transport-based model may

resolve consistent discrepancies [17] observed between past efforts and experimental data. Objective (2) seeks optimization of multiphysics coupling, and QD-based, multilevel methods have been found to significantly accelerate the solution of the coupled neutron transport problem [18].

2 Literature Review

There have been a number of efforts to deterministically model CFRs over the years. Wooten and Powers [14] organize these efforts into three categories: (1) multigroup diffusion (MGD) methods, (2) point reactor kinetics (PRK) methods, and (3) quasi-static (QS) methods.

MGD methods consider the space and, typically, time dependence of the independent variables. PRK methods, after a number of assumptions, consider only the time evolution of the independent variables. MGD approaches, which have higher dimensionality relative to PRK approaches, incur higher computational cost. QS methods employ both MGD and PRK methods by periodically updating a quickly-solved PRK method with a MGD simulation.

Of these approaches, only MGD methods provide the full time- *and* space-dependent solutions sought by the proposed method and, as such, the literature reviewed focuses on MGD CFR modeling techniques. Literature on QD and multilevel methodology, topics significant to the method described in this work, will also be reviewed.

(Note: unnamed codes are referred to as ‘the code’ within their section.)

2.1 Multigroup diffusion CFR methods

MGD methods, in general, operate on the coupled system in Eq. (2.1).

$$\begin{aligned} \frac{1}{v_g} \frac{\partial \phi_g}{\partial t} - \nabla \cdot D_g \nabla \phi_g + \sum_{g' \neq g}^G \Sigma_{s,g \rightarrow g'} \phi_g + \Sigma_{a,g} \phi_g = & \sum_{g' \neq g}^G \Sigma_{s,g' \rightarrow g} \phi_{g'} \\ & + (1 - \beta) \chi_{p,g} \sum_{g'=1}^G (\nu \Sigma_f)_{g'} \phi_{g'} + \sum_{i=1}^I \chi_{d,g,i} \lambda_i C_i \end{aligned} \quad (2.1a)$$

$$\frac{\partial C_i}{\partial t} = \beta_i \sum_{g=1}^G (\nu \Sigma_f)_g \phi_g - \lambda_i C_i - \nabla \cdot (C_i \vec{u}) \quad (2.1b)$$

where

v_g	[cm/s]	= neutron velocity in neutron group g ,
ϕ_g	[1/cm ² s]	= scalar neutron flux in neutron group g ,
D_g	[cm]	= diffusion coefficient in neutron group g ,
$\Sigma_{s,g \rightarrow g'}$	[1/cm]	= macroscopic scattering cross section from neutron group g into g' ,
$\Sigma_{a,g}$	[1/cm]	= macroscopic absorption cross section in neutron group g ,
$\Sigma_{s,g' \rightarrow g}$	[1/cm]	= macroscopic scattering cross section from neutron group g' into g ,
β	[unitless]	= delayed neutron fraction,
$\chi_{p,g}$	[unitless]	= probability to produce a fission neutron in neutron group g ,
ν	[unitless]	= average number of fission neutrons,
Σ_f	[1/cm]	= macroscopic fission cross section,
$\chi_{d,g,i}$	[unitless]	= probability to produce a delayed neutron in neutron group g from precursor group i ,
λ_i	[1/s]	= decay constant in precursor group i ,
C_i	[1/cm ³]	= precursor concentration in precursor group i ,
β_i	[unitless]	= delayed neutron fraction in precursor group i ,
\vec{u}	[m/s]	= precursor velocity,

Equation (2.1a) is the multigroup neutron diffusion equation. Eq. (2.1b) is the

DNP balance equation. Generally, the flux ϕ_g has homogeneous Dirichlet boundary conditions and the precursor concentration C_i has a periodic boundary condition. The model formed by the coupled system of these equations differs from the model of an SFR by the inclusion of the fourth term in Eq. (2.1b). This term accounts for precursor advection. Many works also couple the system in Eq. (2.1) to equations describing heat transfer and/or fluid flow.

Note the absence of a term describing the advection of neutrons in (2.1a), despite the neutrons' presence in a moving media. The inclusion of such a term would be erroneous, as the neutron cross sections are formulated in consideration of the relative motion between a neutron and nucleus.

The following sections review in detail a number of contemporary works utilizing variations of this description to model neutron kinetics.

2.1.1 Cinsf1D [19]

In 2003, Lecarpentier and Carpentier presented **Cinsf1D**, a code used to analyze the AMSTER MSR concept. **Cinsf1D** operates on a 1D, two neutron group, and six DNP group formulation of the coupled system in Eq. (2.1) with a few exceptions:

1. Radial leakage coefficients are present in the neutron diffusion equations
2. The system is coupled with equations describing heat transfer for the fuel salt and surrounding material

The final item is of particular importance, as the cross sections present in Eq.

(2.1) have a nontrivial dependence on temperature.

While the methods used to solve the MGD system are not explicitly mentioned, it appears Lecarpentier and Carpentier approximate the spatial and temporal derivatives for the fluxes and precursor concentrations with a mix of implicit finite difference and finite volume methods. The resulting linear system is solved with a Jacobi iteration.

The coupled heat equations are solved explicitly. This introduces the familiar Courant stability condition:

$$\frac{\Delta t}{\Delta x} \vec{u} < 1, \quad (2.2)$$

where Δt and Δx are the temporal and spatial steps respectively.

A comparison between `Cinsf1D` and a PRK model is presented, but Lecarpentier and Carpentier refrain from any claims of validation or verification after deeming the PRK model “oversimplified”. For the purpose of the tool, which seems to focus on design feasibility studies, the authors claim “... the level of precision achieved by [`Cinsf1D`] would seem to be sufficient.”

The stability restriction introduced by the explicit solution to the heat equations could make spatial refinement prohibitively expensive from a computational perspective, as refinement in space would require a commensurate refinement in time.

2.1.2 Yamamoto et al. [20]

In 2006, Yamamoto et al. presented an MSR analysis code and demonstrated the code on an accident scenario. The code features a 2D RZ geometry, two neutron group, and six DNP group formulation of the coupled system in Eq. (2.1). Notable deviations include:

1. The neutron kinetics system is coupled to heat transfer equations for the fuel salt and surrounding material
2. The neutron kinetics system is coupled to equations describing flow of the fuel salt

The coupled system describing neutron kinetics, heat transfer, and fluid flow is discretized with implicit finite volume methods and the resulting linear system is solved using successive over relaxation, an iterative technique. As only implicit methods are used, the stability of this approach is not dependent on the mesh size.

No comparison is made to similar codes, nor to experimental results. Instead, taking advantage of its coupling to the fluid flow equations, the code is used to analyze a blockage accident scenario where an obstruction prevents flow of the fuel salt in sections of the core, a worst case scenario for an MSR. Overall, Yamamoto et al. “confirmed that the self controllability of MSR effectively works during the blockage accident.”

2.1.3 DYN1D-MSR and DYN3D-MSR [21, 22]

In 2005, Krepel et al. presented DYN1D-MSR, which operates on a 1D, two neutron group, six precursor group formulation of Eq. (2.1). Notable deviations include:

1. The neutron kinetics system is coupled to heat transfer equations for the fuel salt and surrounding material
2. The neutron kinetics system is coupled to equations describing flow of the fuel salt

DYN1D-MSR was developed off the DYN3D code, a piece of software for the simulation of light water reactor neutron kinetics and thermal hydraulics [23]. Across the spatial domain of each time step, DYN1D-MSR uses the method of characteristics to solve Eq. (2.1b) and nodal methods to solve Eq. (2.1a). Implicit finite difference methods are used to approximate the derivatives with respect to time.

In 2006, the functionality of DYN1D-MSR was expanded to operate on a 3D formulation of (2.1) in the form of the appropriately-named DYN3D-MSR. DYN3D-MSR also utilizes a mix of characteristic, nodal, and finite difference methods. The thermal hydraulic models, however, are not expanded to 3D; rather a 1D coupling in the direction of fluid flow is used, as in DYN1D-MSR.

DYN1D-MSR and DYN3D-MSR are validated against experimental data from the MSRE [24]. As an example, see Figure 2.1. Results from both codes agree fairly well with experimental data for reactivity lost as a result of precursor drift.

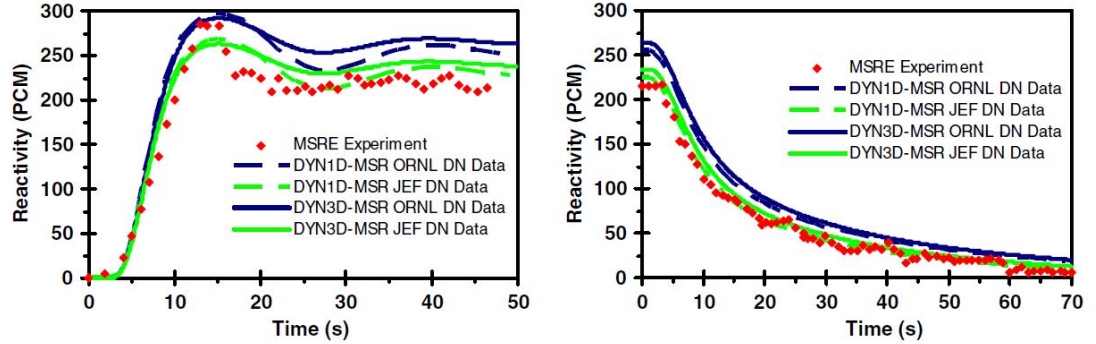


Figure 2.1: Reactivity lost through precursor drift. Left: pump start-up event. Right: pump shutdown event. Fig. 9 from [22].

JEF and ORNL denote different material data sets used for the simulations, the former being more recent. In particular, DYN1D-MSR using JEF captures the average behaviour quite well.

2.1.4 Nicolino et al. [25]

In 2007, Nicolino et al. presented a code which operates on an RZ formulation of the coupled system in Eq. (2.1) for an arbitrary number of neutron energy and DNP groups. The tool was developed with molten salt fast reactor (MSFR) analysis in mind. Notable deviations from Eq. (2.1) include:

1. Density dependence of nuclear data is assumed to be linear
2. The neutron kinetics system is coupled to heat transfer equations for the fuel salt

3. The neutron kinetics system is coupled to equations describing flow of the fuel salt

A single reference point is used for the extrapolation of nuclear data.

In the previous section, which focuses on thermal reactors where flow is constrained by graphite channels, 1D fluid flow equations were used. In MSFR concepts such as MOSART, the primary concept considered by Nicolino et al., these channels are not present, and an RZ formulation is necessary to capture “dynamical evolution” of the reactor.

The coupled system is solved with a fully implicit approach on a uniform grid. Diffusion and advection terms are treated with central differencing and upwinding, respectively. The linear system is solved with the Jacobian Free Newton Krylov algorithm.

Results are presented for a number of MSFR scenarios, but comparisons to other codes are absent, as are comparisons to experimental data. As an MSFR has yet to be built, the latter absence is to be expected.

2.1.5 Zhang et al. [26]

In 2008, Zhang et al. presented a code which operates on an RZ formulation of the coupled system in Eq. (2.1) for two neutron energy groups and six DNP groups. Notable deviations include:

1. Two spurious terms are included on the left-hand side of Eq. (2.1a)

$$\frac{1}{v_g} \frac{\partial(u_z \phi_g)}{\partial z} + \frac{1}{v_g r} \frac{\partial(r u_r \phi_g)}{\partial r}$$

2. The neutron kinetics system is coupled to heat transfer equations for the fuel salt and surrounding material
3. The neutron kinetics system is coupled to equations describing flow of the fuel salt

The terms in the first deviation imply neutrons are subject to the macroscopic effects of fuel salt motion. This is not true, and the above terms should not be included in (2.1a), as observed by Wooten and Powers.

Zhang et al. also elect to use an RZ formulation, instead of 1D, to describe fluid flow. Implicit finite volume methods are used to discretize the coupled system.

The code is validated by comparing to benchmarks and codes designed for solid fuel reactors. The comparison is enabled by assuming the fuel salt velocity to be zero. Comparisons to MSR-specific codes or experimental data are absent. Results are presented for a simplified thermal MSR design. The effects of inflow temperature, inflow velocity, and out-of-core DNP residence time on multiplication factor, neutron fluxes, core temperatures, and delayed neutron precursor are presented. In these results, the flow velocity for the channel-type design considered is found to be uniform, suggesting the 1D fluid flow model employed in other works to be reasonable.

2.1.6 Kópházi et al. [27]

In 2009, Kópházi et al. presented a code which operates on a 3D/1D formulation of the coupled system in Eq. (2.1) for an arbitrary number of neutron energy and DNP groups. Notable deviations include:

1. The neutron diffusion equation, Eq. (2.1a), is solved in the reactor core only, while the DNP balance equation, Eq. (2.1b), is solved throughout the primary circuit of the fuel salt
2. In the discretization of Eq. (2.1b), Kópházi et al. include a ‘fuel fraction parameter’ to allow for Eq. (2.1b) and Eq. (2.1a) to be solved on the same mesh
3. The neutron kinetics system is coupled to heat transfer equations for the fuel salt and surrounding material
4. The neutron diffusion and DNP balance equations are solved in 3D and 1D, respectively

The first point makes this work distinct from previous thermal MSR works which specify a particular DNP concentration boundary condition on the fuel channel inlet to account for out-of-core residence time.

The reactor is modeled as a rough solid cylinder of graphite with axial fuel channels. A 1D heat conduction model is used in the fuel channels, and a 3D heat conduction model is used in the graphite. This differs from previous works as multiple thermally connected fuel channels are modeled at once, as opposed

to considering a single fuel channel or a simplified geometry. The fuel velocity is taken as an input from the user.

The neutron kinetics system is solved using implicit finite volume methods through DALTON_{MSR}, a modified version of the 3D multigroup diffusion code DALTON [28]. The heat transfer equations are solved with THERM [28], which uses implicit methods. The combined system is solved with iteration between the two codes.

The code was validated by comparing calculated feedback coefficients and power during a natural circulation transient to data collected from the MSRE. The latter comparison can be seen in Figure 2.2.

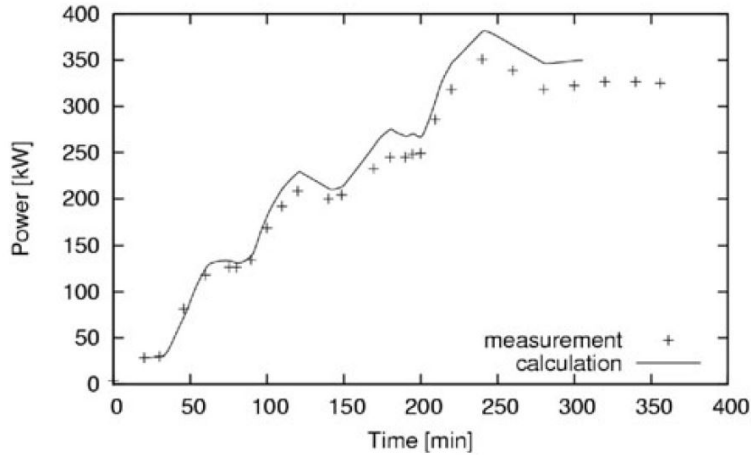


Figure 2.2: Power during natural circulation transient. Fig. 9 from [27].

The measured and calculated values agree fairly well.

Kópházi et al. present results considering a number of different scenarios, one of which is a debris-induced incident where the flow in a number of fuel channels is severely limited. This scenario is similar to that considered by Yamamoto et al. in

[20]. Kópházi et al. found thermal coupling of the fuel channels, present in their work through heat conduction in the graphite moderator, to play an important role in the analysis of this reactor-safety scenario.

2.1.7 Aufiero et al. [29]

In 2014, Aufiero et al. presented a code which operates on a 3D formulation of the coupled system in Eq. (2.1) for a single neutron energy group and eight DNP groups. The code is designed primarily for analysis of MSFRs. Notable deviations from Eq. (2.1) include:

1. Temperature dependence of nuclear data is assumed to be logarithmic
2. Density dependence of nuclear data is assumed to be linear
3. A turbulent diffusion term is added to the right-hand side of Eq. (2.1b)

$$\nabla \cdot \frac{\nu_T}{Sc_t} \nabla C_i,$$

where ν_T is eddy viscosity and Sc_t is the turbulent Schmidt number

4. The neutron kinetics system is coupled to heat transfer equations for the fuel salt and heat exchangers
5. The neutron kinetics system is coupled to equations describing flow of the fuel salt

A single reference point is used for extrapolation of nuclear data.

Aufiero et al. implement and solve the coupled neutron kinetics and thermal hydraulics system in OpenFOAM [30], an open-source tool capable of solving coupled systems of partial differential equations with a variety of techniques. An implicit Runge-Kutta scheme was selected in this case. Solving the entire system with OpenFOAM avoids the operator splitting as seen in [27], for example, where the neutron kinetics systems is solved first and used as an input to the thermal hydraulics solver. Solving the system together avoids “inaccurate results in the case of strong feedback between the physics.”

As experimental data of an MSFR is lacking, Aufiero et al. compare results to two other codes designed for MSFR analysis. The fuel temperature at nominal conditions is considered, in addition to average fuel temperature and power during a reactivity insertion event. The three codes are in reasonable agreement. The comparison for average fuel temperature can be seen in Figure 2.3.

2.1.8 Fiorina et al. [31]

In 2014, Fiorina et al. presented a code developed at *Politecnico di Milano* which operates on a 2D formulation of the coupled system in Eq. (2.1) in RZ geometry with six neutron energy groups and eight DNP groups. This code was developed for analysis of MSFRs. Notable deviations from Eq. (2.1) include:

1. Equations describing decay heat are included
2. Temperature dependence of nuclear data is assumed to be logarithmic

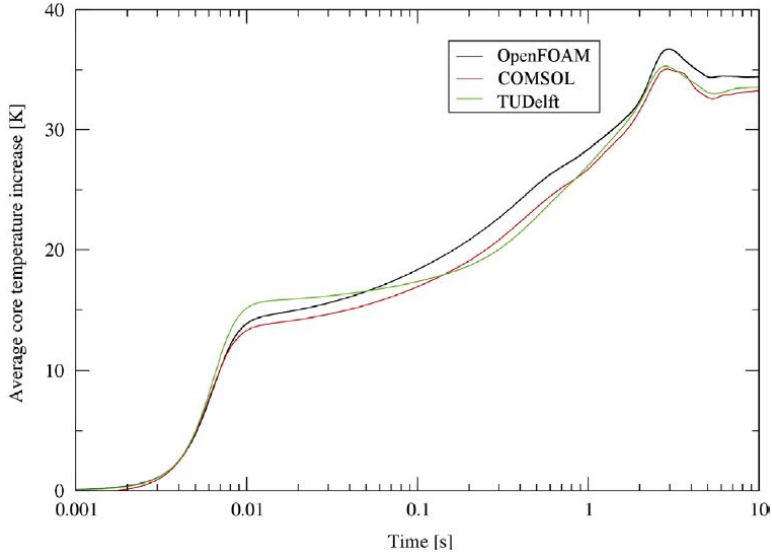


Figure 2.3: Comparison of OpenFOAM [29], COMSOL [31], TUDelft [27] codes. Figure 13 from [29].

3. Density dependence of nuclear data is assumed to be linear
4. A turbulent diffusion term is added to the right-hand side of Eq. (2.1b)

$$\nabla \cdot \frac{\nu_T}{Sc_t} \nabla C_i,$$

5. The neutron kinetics system is coupled to heat transfer equations for the fuel salt and secondary loops
6. The neutron kinetics system is coupled to equations describing flow of the fuel salt and secondary loops

Two reference points are used for interpolation of nuclear data. The neutron kinetics system is coupled to 2D, RZ equations describing fluid flow and heat

transfer to the fuel salt and secondary loops. The fully coupled system is solved with finite elements using COMSOL [32].

Fiorina et al. compare computational results of the *Politecnico di Milano* code to those found with the code developed by Kópházi et al. in [27] (potentially an earlier version of the code than discussed in the prior section). Steady state and a number of transient scenarios are considered. Both codes are in good agreement for the cases presented. A comparison of the two codes can be seen in Figure 2.3, where the *Politecnico di Milano* code is labeled COMSOL and the code by Kópházi et al. is labeled TUDelft.

In most of the cases considered, the effects of decay heat were “found to be negligible.”

2.1.9 MOREL [33]

In 2014, Zhuang et al. presented MOREL, a code which operates on a 3D/1D formulation of Eq. (2.1) for an arbitrary number of neutron energy and DNP groups. Notable deviations include:

1. The diffusion coefficient D_g is independent of space
2. Eq. (2.1a), the neutron diffusion equation, is solved in 3D, and Eq. (2.1b), the DNP balance equation, is solved in 1D

The neutron kinetics system is not coupled to the any thermal hydraulics equations. Instead, variables such as velocity and density are selected based on MSRE

operational data. The solution to the neutron kinetics system seems to be split. The neutron diffusion equation is discretized in time with an implicit finite difference method, and the resulting form is solved with the nodal diffusion code TABFEN. The DNP balance equation is then solved using the method of characteristics. Burnup and fuel processing are also considered by Zhuang et al., although the exact equations describing these mechanisms are not given.

The steady state operation and burnup of MOREL were validated by comparison to a Monte Carlo simulation with depletion coupling. Transient validation of MOREL was achieved by comparison to data from the MSRE. Some analysis is performed for the Thorium Molten Salt Reactor project, as well. Zhuang et al. conclude that the validation “results prove that MOREL code can be used for the analysis of MSR.”

2.1.10 Moltres [34]

In 2018, Lindsay et al. presented **Moltres**, an open-source code which operates on a 3D-1D/1D formulation of Eq. (2.1) for an arbitrary number of neutron energy and DNP groups. Notable deviations include:

1. The neutron kinetics system is coupled to heat transfer equations for the fuel salt and surrounding material
2. **Moltres** can solve in 1D, 2D, and 3D geometries for Eq. (2.1a), the neutron diffusion equation

3. Eq. (2.1b), the DNP balance equation, is solved in 1D

Although not explicitly stated, fuel salt velocity is assumed to be an input. The fully coupled system is implemented and solved in MOOSE [35]. MOOSE leverages a number of software packages and toolkits to solve partial differential equations using finite elements, and has the capability to do so in parallel using MPI. The solution can be found explicitly or implicitly.

Lindsay et al. present results for a design closely resembling the MSRE, and verify **Moltres** by comparison to design calculations for the MSRE. Lindsay et al. conclude the variations observed are “acceptable for the purpose of this work.” A scaling performance study is also conducted to evaluate the parallel capabilities of **Moltres**, and it was found to exhibit strong scaling characteristics.

2.1.11 Remarks

The approaches of the preceding works vary greatly; even the basic formulation of Eq. (2.1) spans from 1D-3D in Cartesian to cylindrical geometry with a single to an arbitrary number of neutron energy groups. Finite differences, volumes, and elements are all used to solve the coupled neutron kinetics systems. Some of the works create their own solvers, and others leverage existing PDE and ODE solvers such as COMSOL or MOOSE.

There are, however, a number of categorical and total similarities among the reviewed codes. Codes developed for channel-type MSR mostly utilized 1D descriptions of fuel flow, and compared well to experimental data. Codes developed

for MSFRs required 2D fluid flow equations to capture the dynamics of these designs. Nearly all works favored fully implicit methods for their unconditional stability, and coupled Eq. (2.1) to an equation(s) describing heat transfer in the system.

All the codes share a criticism - they are computationally expensive [14]. Multiphysics phenomena are coupled to the MGD equations, a coupling that often requires an iterative solver or linear assumptions regarding the temperature dependence of nuclear data. The former results in a costly computation and the latter in a limited analysis. Implementing an acceleration method could greatly reduce computational cost.

A literature review of topics pertinent to the proposed method is now presented.

2.2 Quasi-diffusion [36, 37, 38]

In 1964, Gol'Din presented the quasi-diffusion method for accelerating the solution of the neutron transport equation. A steady state instance of the neutron transport equation in one dimension is given in Eq. (2.3).

$$\mu \frac{\partial(\psi)}{\partial x} + \Sigma_t \psi = \frac{1}{2} [\Sigma_s \phi + Q]. \quad (2.3)$$

The QD methodology begins by taking the zeroth and first angular moments of the neutron transport equation. The zeroth, unweighted angular moment of Eq.

(2.3) is given in Eq. (2.4).

$$\frac{\partial J}{\partial x} + \Sigma_t \phi = \Sigma_s \phi + Q, \quad (2.4)$$

where the definitions for scalar neutron flux ϕ and net neutron current J have been used,

$$\phi = \int \psi d\mu, \quad J = \int \mu \psi d\mu. \quad (2.5)$$

The first angular moment, weighted by μ , of Eq. (2.3) is given in Eq. (2.6).

$$\frac{\partial(E\phi)}{\partial x} + \Sigma_t J = 0, \quad (2.6)$$

where the Eddington factor E is defined as

$$E = \frac{\int \mu^2 \psi d\mu}{\int \psi d\mu}. \quad (2.7)$$

The system formed by Eqs. (2.4) and (2.6) can be used as an acceleration scheme for finding the solution of Eq. (2.3), and reproduces the transport effects exactly as the system is formed without approximation. The solution process is given below.

1. An initial guess ϕ^l is made
2. The transport equation Eq. (2.3) is solved for $\psi^{l+1/2}$ using ϕ^l
3. Eddington factors are calculated using $\psi^{l+1/2}$

4. The QD Eqs. (2.4), (2.6) are solved for a new ϕ^{l+1}

5. $l = l + 1$, repeat steps 2 → 4 until $||\phi^l - \phi^{l-1}|| < \epsilon$

As the QD system is only weakly dependent on the angular flux ψ (through the Eddington factor E and boundary conditions), the “iterational process is rapidly convergent.” [36]

QD can also be applied to the solution of the multigroup neutron transport equations [37, 38]. The process is analogous to that described here for a single-group, but with transport and QD equations for each neutron energy group.

2.3 Multilevel methods

The QD method has been used extensively in the formulation of multilevel methods to solve a variety of multiphysics problems. These multilevel methods have been used to solve the neutron transport and burnup problems [39], radiation hydro-dynamics problems [40, 41, 42, 43, 44, 45], and, more recently, the neutron transport and heat transfer problem [18].

Multilevel methods take a problem of high-order and formulate a low-order problem whose solution can be found more quickly. The solution of the low-order problem is then used to accelerate the solution of the high-order problem. The solution procedure presented in the previous section follows this pattern. Where the previous section featured only two levels, however, the QD-based multilevel methods discussed here typically have three, as in Figure 2.4.

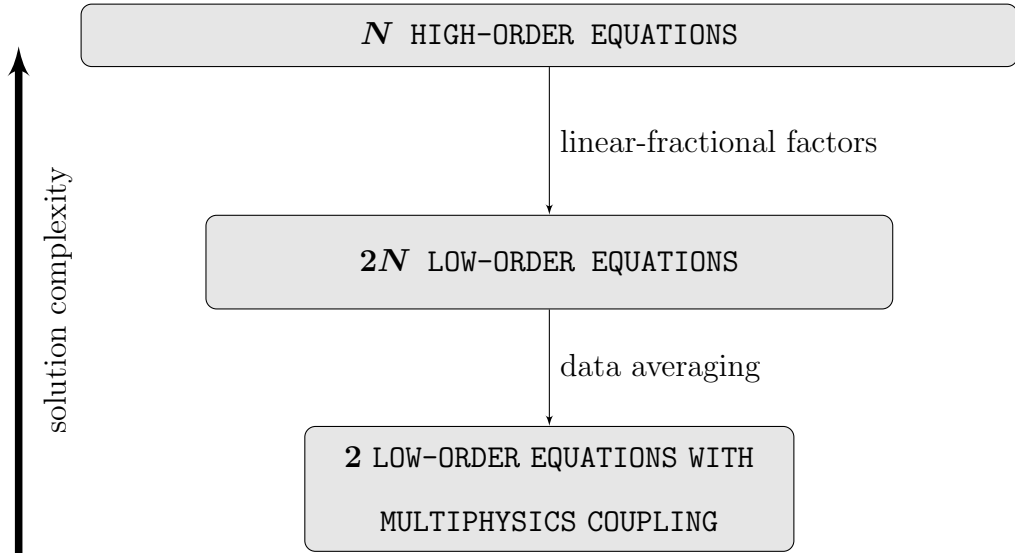


Figure 2.4: Diagram of a multilevel method in 1D.

The top-level, high-order problem, such as a system of multigroup neutron transport equations, is solved first. The solution to the high-order problem is used to formulate the mid-level problem through the calculation of linear fractional factors, such as the Eddington factors E . The solution to the mid-level problem is then used to formulate the low-level problem through data averaging and calculation of effective total parameters such as total scalar neutron flux.

Multiphysics coupling occurs in the low-level problem; two low-order equations are coupled to the multiphysics equations for the given application, e.g. burnup, precursor balance, heat transfer, etc. This is advantageous as neutronically, among the three levels, a single solve of the low-level problem requires the least computational cost. As mentioned before, multiphysics coupling, particularly with nuclear

data, is often non-linear and requires the use of an iterative solver. By implementing multiphysics coupling in the low-level problem, the computational cost of the iterative solve is reduced.

3 Methods

Eqs. (3.1a), (3.1b), and (3.1c) represent a model in RZ geometry of CFR neutron kinetics coupled to a basic equation governing heat transfer. The fuel flow is assumed to be purely axial. Sources terms within the neutron transport equation are assumed to be isotropic.

$$\begin{aligned} \frac{1}{v_g} \frac{\partial}{\partial t} \psi_g(\hat{\Omega}, r, z, t) + \frac{\mu}{r} \frac{\partial}{\partial r} \left(r \psi_g(\hat{\Omega}, r, z, t) \right) + \xi \frac{\partial}{\partial z} \psi_g(\hat{\Omega}, r, z, t) - \frac{1}{r} \frac{\partial}{\partial \omega} \left(\eta \psi_g(\hat{\Omega}, r, z, t) \right) \\ + \Sigma_{t,g}(r, z, t) \psi_g(\hat{\Omega}, r, z, t) = \frac{1}{\int_{\hat{\Omega}} d\hat{\Omega}} \left(\sum_{g'=1}^G \Sigma_{s,g' \rightarrow g}(r, z, t) \int_{\hat{\Omega}} \psi_{g'}(\hat{\Omega}', r, z, t) d\hat{\Omega}' \right. \\ \left. + \chi_g^p(r, z, t) \sum_{g'=1}^G (1 - \beta_{g'}) \nu_{f,g'}(r, z, t) \Sigma_{f,g'}(r, z, t) \int_{\hat{\Omega}} \psi_{g'}(\hat{\Omega}', r, z, t) d\hat{\Omega}' \right. \\ \left. + \sum_{d=1}^{N_d} \lambda_d \chi_g^d(r, z, t) C_d(r, z, t) \right), \quad g = 1, \dots, G, \quad (3.1a) \end{aligned}$$

$$\begin{aligned} \frac{\partial}{\partial t} C_d(r, z, t) + \frac{\partial}{\partial z} (\vec{u}(r, z, t) C_d(r, z, t)) = -\lambda_d C_d(r, z, t) \\ + \sum_{g'=1}^G \beta_{d,g'} \nu_{f,g} \Sigma_{f,g'}(r, z, t) \int_{\hat{\Omega}} \psi_{g'}(\hat{\Omega}', r, z, t) d\hat{\Omega}', \quad d = 1, \dots, N_d, \quad (3.1b) \end{aligned}$$

$$\begin{aligned}
& \frac{\partial}{\partial t} (\rho(r, z, t) c_p(r, z, t) T(r, z, t)) - \frac{\kappa(r, z, t)}{r} \frac{\partial}{\partial r} \left(r \frac{\partial}{\partial r} T(r, z, t) \right) \\
& - \kappa \frac{\partial^2}{\partial z^2} T(r, z, t) + \frac{\partial}{\partial z} (\vec{u}(r, z, t) \rho(r, z, t) c_p(r, z, t) T(r, z, t)) \\
& = Q_\gamma(r, z, t) + Q_f(r, z, t), \quad (3.1c)
\end{aligned}$$

where the fission and moderator energy deposition terms are

$$Q_f(r, z, t) = \sum_{g'=1}^G \omega_f \Sigma_{f,g'}(r, z, t) \int_{\hat{\Omega}} \psi_{g'}(\hat{\Omega}', r, z, t) d\hat{\Omega}', \quad (3.2)$$

$$Q_m(r, z, t) = \begin{cases} \frac{\gamma}{V_{\text{core}}} \int_{\text{core}} Q_f(r, z, t) dV, & \text{in moderator} \\ 0, & \text{otherwise} \end{cases}, \quad (3.3)$$

and

ψ_g	[1/cm ² s]	= angular neutron flux in neutron group g ,
β_g	[unitless]	= cumulative DNP fraction angular neutron flux in neutron group g ,
$\beta_{d,g}$	[unitless]	= DNP fraction for DNP group d in neutron group g ,
ρ	[kg/cm ³]	= material density,
κ	[W/cm K]	= thermal conductivity,
c_p	[J/K kg]	= specific heat,
ω_f	[J/fission]	= energy released in fission event,
γ	[unitless]	= graphite to fuel power density ratio.

The definition of Q_m assumes the energy deposited in the moderator (through gamma and neutron irradiation) is a fraction γ of the total fission energy deposited

in the core [34]. The approach of Cammi et al. [46] is used to define the value for $\gamma = 0.0144$, which is taken from design calculations for a molten salt breeder reactor [9].

The direction of flight, $\hat{\Omega}$, is characterized by the azimuthal and polar angles ω and θ , which define the direction cosines $(\hat{\Omega}_r, \hat{\Omega}_\gamma, \hat{\Omega}_z) = (\mu, \eta, \xi)$.

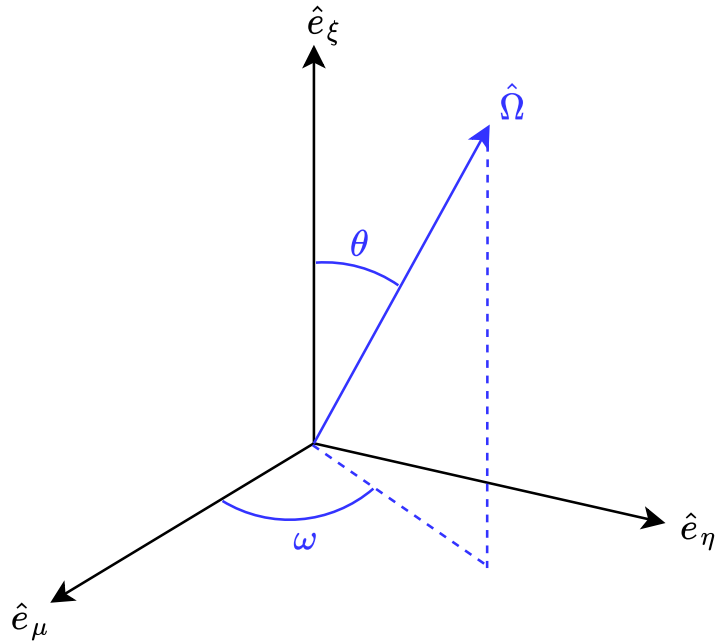


Figure 3.1: Direction of flight $\hat{\Omega}$.

$$\mu = \sin(\theta) \cos(\omega) = \sqrt{(1 - \xi^2)} \cos(\omega), \quad (3.4)$$

$$\eta = \sin(\theta) \sin(\omega) = \sqrt{(1 - \xi^2)} \sin(\omega), \quad (3.5)$$

$$\xi = \cos(\theta). \quad (3.6)$$

In this work, the following boundary conditions are used.

$$\left[\psi_g(\hat{\Omega}, r, z, t) = \psi_g(\hat{\Omega}', r, z, t) \right]_{r=0} = 0, \quad \hat{n} \cdot \hat{\Omega} < 0. \quad (3.7a)$$

$$\hat{n} \cdot \hat{\Omega} = -\hat{n} \cdot \hat{\Omega}', \quad (3.7b)$$

$$(\hat{\Omega} \times \hat{\Omega}') \cdot \hat{n} = 0, \quad (3.7c)$$

$$\psi_g(\hat{\Omega}, r, z, t)|_{(r,z) \in \delta D, r \neq 0} = \psi_{g,\text{incident}}, \quad \hat{n} \cdot \hat{\Omega} < 0. \quad (3.7d)$$

where \hat{n} is the boundary surface normal. Eqs. (3.7a) - (3.7c) impose a reflective boundary condition, as described by Lewis and Miller [47], on the angular flux along the z -axis, where $\hat{\Omega}'$ is the incident angle. Eq. (3.7d) imposes Dirichlet conditions on the incident angular fluxes of the remaining boundaries.

$$T(r, z, t) = \begin{cases} T^{\text{in}}, & z = 0 \\ T^{\text{wall}}, & r = R \end{cases}, \quad (3.8a)$$

$$\left[\frac{\partial}{\partial r} T(r, z, t) \right]_{r=0} = 0, \quad (3.8b)$$

$$\left[\frac{\partial}{\partial z} T(r, z, t) \right]_{z=z} = 0. \quad (3.8c)$$

Eq. (3.8a) imposes Dirichlet conditions on the inlet and wall temperature, Eq. (3.8b) imposes a reflective condition on the temperature along the z -axis, and Eq.

(3.8c) imposes a free outflow condition.

$$C_d(r, z, t)|_{z=0} = C_d^{\text{in}}, \quad (3.9a)$$

$$\left[\frac{\partial}{\partial r} C_d(r, z, t) \right]_{z=Z} = 0. \quad (3.9b)$$

Finally, Eqs. (3.9a) and (3.9b) impose Dirichlet and free outflow conditions on the inlet and outlet DNP concentrations, respectively. Note that Eqs. (3.8) and (3.9) assume a positive flow velocity u . In the event of negative u , the axial conditions are swapped.

The coupled system in Eq. (3.1) accompanied by the boundary conditions in Eqs. (3.7), (3.8), and (3.9) is solved with a multilevel approach that requires solutions at three levels. The first level requires solving the multigroup neutron transport equations, the second requires solving the multigroup QD equations, and the third level requires solving single group QD equations coupled to the multiphysics phenomena.

The proceeding sections describe the solution methods at each of the levels and are followed by a description of the overall solution algorithm. A steady-state variant of the method is also detailed.

3.1 Multigroup neutron transport

At the multigroup high-order transport (MGHOT) level, modified versions of the equations in Eq. (3.1a) are solved.

$$\begin{aligned} \frac{1}{v_g} \frac{\partial}{\partial t} \psi_g + \frac{\mu}{r} \frac{\partial}{\partial r} (r \psi_g) + \xi \frac{\partial}{\partial z} \psi_g - \frac{1}{r} \frac{\partial}{\partial \omega} (\eta \psi_g) + \Sigma_{t,g} \psi_g \\ = \frac{1}{\int_{\hat{\Omega}} d\hat{\Omega}} \left[\left(\bar{\Sigma}_{s,g} + \chi_g^p \overline{(1-\beta) \nu \Sigma_f} \right) \phi + \sum_{d=1}^{N_d} \lambda_d \chi_g^d C_d \right], \quad g = 1, \dots, N_G. \end{aligned} \quad (3.10)$$

Variable dependencies have been dropped for compactness. The scattering and fission source terms are calculated using the grey group flux ϕ , defined in Section 3.3. The scattering and the fission source coefficients are averages weighted by the group fluxes ϕ_g , defined in Section 3.2.

$$\bar{\Sigma}_{s,g} = \frac{\sum_{g'=1}^G \Sigma_{s,g' \rightarrow g} \phi_{g'}}{\sum_{g'=1}^G \phi_{g'}} \quad (3.11)$$

$$\overline{(1-\beta) \nu \Sigma_f} = \frac{\sum_{g'=1}^G (1-\beta_g) \nu_{f,g} \Sigma_{f,g} \phi_{g'}}{\sum_{g'=1}^G \phi_{g'}} \quad (3.12)$$

3.1.1 Time discretization

The time derivative is approximated by assuming ψ_g has an exponential dependence with respect to time.

$$\psi_g(\hat{\Omega}, r, z, t) = \psi_{g,\alpha}(\hat{\Omega}, r, z) e^{\alpha_g(r,z,t)t}, \quad (3.13)$$

where

$$\alpha_g(r, z, t) = \frac{1}{\phi_g(r, z, t)} \frac{\partial \phi_g(r, z, t)}{\partial t}. \quad (3.14)$$

Substituting this expression into Eq. (3.10) yields

$$\begin{aligned} & \frac{\mu}{r} \frac{\partial}{\partial r} (r \psi_g) + \xi \frac{\partial}{\partial z} \psi_g - \frac{1}{r} \frac{\partial}{\partial \omega} (\eta \psi_g) + \tilde{\Sigma}_{t,g} \psi_g \\ &= \frac{1}{\int_{\hat{\Omega}} d\hat{\Omega}} \left[\left(\bar{\Sigma}_{s,g} + \chi_g^p \overline{(1-\beta) \nu \Sigma_f} \right) \phi + \sum_{d=1}^{N_d} \lambda_d \chi_g^d C_d \right], \quad g = 1, \dots, N_G, \end{aligned} \quad (3.15)$$

where

$$\tilde{\Sigma}_{t,g} = \begin{cases} \Sigma_{t,g} + \alpha_g, & \text{for } \Sigma_{t,g} + \alpha_g > 10^{-4}, \\ 0, & \text{otherwise} \end{cases} \quad (3.16)$$

$\tilde{\Sigma}_{t,g}$ can be interpreted as the effective total cross section. Considering this interpretation, negative values would be non-physical and have been found to produce instabilities [47, 48], motivating the second condition in Eq. (3.16).

The discretized α -eigenvalue is shown in Eq. (3.17).

$$\alpha_g(r_i, z_j, t^n) \approx \alpha_{g,ij}^n = \frac{1}{\Delta t^n} \ln \frac{\phi_{g,ij}^n}{\phi_{g,ij}^{n-1}}. \quad (3.17)$$

If encountered, the second condition in Eq. (3.16) may be avoided by sufficient refinement of the temporal mesh.

3.1.2 Angular discretization

Using the S_n approximation [15], Eq. (3.15) is solved at a discrete number of angles.

$$\begin{aligned} \frac{\mu_{pq}}{r} \frac{\partial}{\partial r} (r \psi_{g,pq}) + \xi_p \frac{\partial}{\partial z} \psi_{g,pq} - \frac{1}{r} \frac{\partial}{\partial \omega} (\eta_{pq} \psi_{g,pq}) + \tilde{\Sigma}_{t,g} \psi_{g,pq} \\ = \frac{1}{4} \left[\left(\bar{\Sigma}_{s,g} + \chi_g^p (1 - \beta) \nu \Sigma_f \right) \phi + \sum_{d=1}^{N_d} \lambda_d \chi_g^d C_d \right], \quad g = 1, \dots, G, \end{aligned} \quad (3.18)$$

$\psi_{g,pq}$ is the angular flux in direction $\hat{\Omega}_{pq}$, which is characterized by the direction cosines $(\mu_{pq}, \eta_{pq}, \xi_p)$. The evaluated angles are determined from a level-symmetric quadrature set with $n = 12$, where the ordinates on level p share constant ξ_p as depicted in Figure 3.2. This property is critical to the approximation of the angular derivative to be described shortly. Note that in Eq. (3.18), $\int_{\hat{\Omega}} d\hat{\Omega} = 4.0$ based on the selection of weights for the quadrature set. The full quadrature set is in Table A.1 of Appendix A.

The approach of Lewis and Miller [47] is used to approximate the derivative with respect to ω , which assumes

$$-\frac{1}{r} \frac{\partial}{\partial \omega} (\eta \psi_{g,pq})|_{\omega=\omega_{pq}} \approx \frac{\epsilon_{q+1/2}^p \psi_{g,p,q+1/2} - \epsilon_{q-1/2}^p \psi_{g,p,q-1/2}}{rw_{pq}}. \quad (3.19)$$

Note that if the half angles $q + 1/2$ and $q - 1/2$ did not exist on the same level p , the approximation in Eq. (3.19) would not be valid, as their differing azimuthal angles would need to be considered, as noted by Lewis and Miller. Introduction

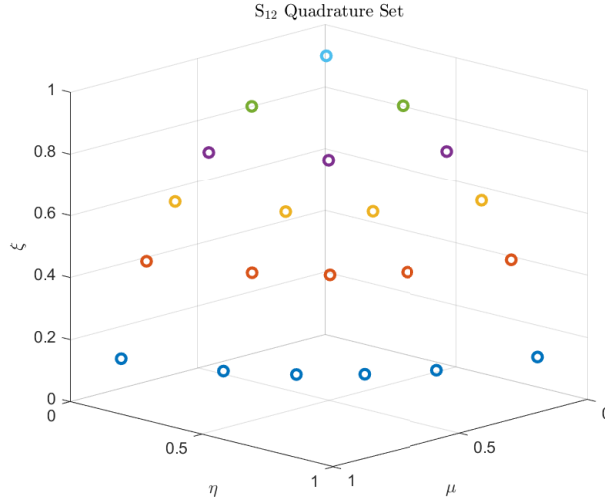


Figure 3.2: Ordinates in one octant are displayed. Ordinates on different levels are distinguished by color.

of the differencing coefficients $\epsilon_{q\pm 1/2}^p$ allows for evaluation of the angular derivative while satisfying the solution in an uniform infinite medium and conserving neutrons without disallowing the use of a level-symmetric quadrature set. These constraints form a basis for defining the differencing coefficients. In a uniform infinite medium problem with constant angular flux $\psi_{g,pq}$, the streaming term should disappear.

$$\frac{\mu_{pq}}{r} \frac{\partial}{\partial r} (r\psi_{g,pq}) + \xi_p \frac{\partial}{\partial z} \psi_{g,pq} + \frac{\epsilon_{q+1/2}^p \psi_{g,pq} - \epsilon_{q-1/2}^p \psi_{g,pq}}{rw_{pq}} = 0, \quad (3.20)$$

$$\mu_{pq} w_{pq} + \epsilon_{q+1/2}^p - \epsilon_{q-1/2}^p = 0, \quad (3.21)$$

$$\epsilon_{q+1/2}^p = \epsilon_{q-1/2}^p - \mu_{pq} w_{pq}. \quad (3.22)$$

Once a boundary $\epsilon_{1/2}^p$ is defined for a level p , the remaining coefficients follow

recursively. To define the boundary values neutron conservation is enforced. This results in setting

$$\epsilon_{1/2}^p = 0, \quad p = 1, 2, \dots, N. \quad (3.23)$$

The weighted diamond difference scheme of Morel and Montry [49] is used to relate the half-angle fluxes $\psi_{g,p,q\pm 1/2}$ to ψ_{pq} .

$$\psi_{g,pq} = \tau_{pq}\psi_{g,p,q+1/2} + (1 - \tau_{pq})\psi_{g,p,q-1/2}, \quad (3.24)$$

where

$$\tau_{pq} = \frac{\mu_{pq} - \mu_{p,q-1/2}}{\mu_{p,q+1/2} - \mu_{p,q-1/2}}, \quad (3.25)$$

$$\mu_{p,q+1/2} = \sqrt{1 - \xi_p^2} \cos(\varphi_{p,q+1/2}), \quad (3.26)$$

$$\varphi_{p,q+1/2} = \varphi_{p,q-1/2} + \pi \frac{w_{pq}}{w_p}, \quad (3.27)$$

$$w_p = \sum_{q=1}^{N_p} w_{p,q}, \quad (3.28)$$

and N_p is the number of quadrature points in level p .

Substituting the approximation to the angular derivative into Eq. (3.18) produces Eq. (3.29).

$$\begin{aligned} & \frac{\mu_{pq}}{r} \frac{\partial}{\partial r} (r \psi_{g,pq}) + \xi_p \frac{\partial}{\partial z} \psi_{g,pq} + \frac{\epsilon_{q+1/2}^p \psi_{g,p,q+1/2} - \epsilon_{q-1/2}^p \psi_{g,p,q-1/2}}{rw_{pq}} + \tilde{\Sigma}_{t,g} \psi_{g,pq} \\ &= \frac{1}{4} \left[\left(\bar{\Sigma}_{s,g} + \chi_g^p \overline{(1 - \beta) \nu \Sigma_f} \right) \phi + \sum_{d=1}^{N_d} \lambda_d \chi_g^d C_d \right], \quad g = 1, \dots, G. \end{aligned} \quad (3.29)$$

3.1.3 Spatial discretization

The simple corner balance (SCB) method of Adams [50] is used to discretize spatially. The approach in RZ geometry is described by Palmer and Adams [51] and used here. SCB is a subcell, finite-volume method that proceeds by dividing each cell into corners, as in Figure 3.3.

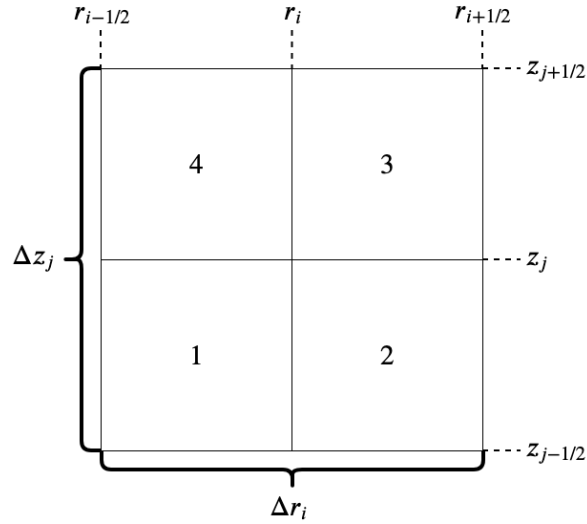


Figure 3.3: Subcell discretization on a cell (i, j)

Eq. (3.18) is integrated over each of the corners and a number of 4x4 linear operators relating the integrals are introduced to produce Eq. (3.30).

$$\begin{aligned} \mu_{pq} L_{ij}^r \vec{\psi}_{pqij}^r + \xi_p L_{ij}^z \vec{\psi}_{pqij}^z + R_{ij} \frac{\epsilon_{q+1/2}^p \vec{\psi}_{p,q+1/2,ij} - \epsilon_{q-1/2}^p \vec{\psi}_{p,q-1/2,ij}}{w_{pq}} \\ + [\mu_{pq} K_{ij}^r + \xi_p K_{ij}^z + \bar{\Sigma}_t T_{ij}] \vec{\psi}_{pqij} = \frac{1}{4} T_{ij} \vec{Q}_{ij} \end{aligned} \quad (3.30)$$

where

$$\vec{\psi}_{pqij}^r = \left[\psi_{pqij,1W} \ \psi_{pqij,2E} \ \psi_{pqij,3E} \ \psi_{pqij,4W} \right]^T, \quad (3.31a)$$

$$\vec{\psi}_{pqij}^z = \left[\psi_{pqij,1S} \ \psi_{pqij,2S} \ \psi_{pqij,3N} \ \psi_{pqij,4N} \right]^T, \quad (3.31b)$$

$$\vec{\psi}_{p,q+1/2,ij} = \left[\psi_{p,q+1/2,ij,1} \ \psi_{p,q+1/2,ij,2} \ \psi_{p,q+1/2,ij,3} \ \psi_{p,q+1/2,ij,4} \right]^T, \quad (3.31c)$$

$$\vec{\psi}_{p,q-1/2,ij} = \left[\psi_{p,q-1/2,ij,1} \ \psi_{p,q-1/2,ij,2} \ \psi_{p,q-1/2,ij,3} \ \psi_{p,q-1/2,ij,4} \right]^T, \quad (3.31d)$$

$$\vec{\psi}_{pqij} = \left[\psi_{pqij,1} \ \psi_{pqij,2} \ \psi_{pqij,3} \ \psi_{pqij,4} \right]^T, \quad (3.31e)$$

$$\vec{Q}_{ij} = \left[Q_{ij,1} \ Q_{ij,2} \ Q_{ij,3} \ Q_{ij,4} \right]^T. \quad (3.31f)$$

$\vec{\psi}_{pqij}^r$ and $\vec{\psi}_{pqij}^z$ are vectors containing the surface-averaged radial and axial out-of-cell angular fluxes in each corner, $\vec{\psi}_{p,q+1/2,ij}$ and $\vec{\psi}_{p,q-1/2,ij}$ are vectors containing the volume-averaged half-angle fluxes in each corner, $\vec{\psi}_{pqij}$ is a vector containing the volume-averaged angular fluxes in each corner, and \vec{Q}_{ij} is a vector containing the volume-averaged source terms in each corner. Note, in abuse of notation in the above definitions, the group indices g have been removed. A derivation of Eq. (3.30) and the linear operators, which are described in Table 3.1, can be found in Appendix B.

Table 3.1: Descriptions of the linear operators in Eq. (3.30).

Linear operator	Description
L_{ij}^r	radial out-of-cell leakage
L_{ij}^z	axial out-of-cell leakage
K_{ij}^r	radial within-cell leakage
K_{ij}^z	axial within-cell leakage
T_{ij}	collision
R_{ij}^r	angular redistribution

The elements of $\vec{\psi}_{pqij}^z$ and $\vec{\psi}_{pqij}^z$ are related to the volume-averaged angular fluxes in each corner using the upwinding method defined in Eq. (3.32).

$$\begin{bmatrix} \psi_{pqij,1W} \\ \psi_{pqij,2E} \\ \psi_{pqij,3E} \\ \psi_{pqij,4W} \end{bmatrix} = \begin{cases} \begin{bmatrix} \psi_{p,q,i,j,1} & \psi_{p,q,i+1,j,1} & \psi_{p,q,i+1,j,4} & \psi_{p,q,i,j,4} \end{bmatrix}^T, & \mu < 0 \\ \begin{bmatrix} \psi_{p,q,i-1,j,2} & \psi_{p,q,i,j,2} & \psi_{p,q,i,j,3} & \psi_{p,q,i-1,j,3} \end{bmatrix}^T, & \mu > 0 \end{cases} \quad (3.32a)$$

$$\begin{bmatrix} \psi_{pqij,1S} \\ \psi_{pqij,2S} \\ \psi_{pqij,3N} \\ \psi_{pqij,4N} \end{bmatrix} = \begin{cases} \begin{bmatrix} \psi_{p,q,i,j,1} & \psi_{p,q,i,j,2} & \psi_{p,q,i,j-1,2} & \psi_{p,q,i,j-1,1} \end{bmatrix}^T, & \xi < 0 \\ \begin{bmatrix} \psi_{p,q,i,j+1,4} & \psi_{p,q,i,j+1,3} & \psi_{p,q,i,j,3} & \psi_{p,q,i,j,4} \end{bmatrix}^T, & \xi > 0 \end{cases} \quad (3.32b)$$

Values falling on the problem boundary are defined by the boundary condition for the angular flux.

Inserting the diamond differencing relation in Eq. (3.24) to Eq. (3.30) yields

$$\begin{aligned} \mu_{pq} L_{ij}^r \vec{\psi}_{pqij}^r + \xi_p L_{ij}^z \vec{\psi}_{pqij}^z + R_{ij} \frac{\left[\frac{\epsilon_{q+1/2}^p}{\tau_{p,q}} (\tau_{pq} - 1) - \epsilon_{q-1/2}^p \right]}{w_{pq}} \vec{\psi}_{p,q-1/2,ij} \\ + \left[\mu_{pq} K_{ij}^r + \xi_p K_{ij}^z + \bar{\Sigma}_t T_{ij} + \frac{\epsilon_{q+1/2}^p}{w_{pq} \tau_{p,q}} R_{ij} \right] \vec{\psi}_{pqij} = \frac{1}{4\pi} T_{ij} \vec{Q}_{pqij}. \end{aligned} \quad (3.33)$$

Eq. (3.33) is solved for each cell in a sweep of the spatial mesh. N sweeps are required for the N ordinates in the quadrature set. The nature and order of each sweep depends on $\hat{\Omega}_{pq}$ and are detailed at the end of this section. Before Eq. (3.33) can be solved, however, solutions for the starting angle fluxes $\vec{\psi}_{p,1/2,ij}$ are needed, after which $\vec{\psi}_{p,q-1/2,ij}$ where $q \neq 1$ can be determined using the diamond difference relation in Eq. (3.24) once the volume-average angular fluxes $\vec{\psi}_{pqij}$ are known.

3.1.4 Starting angle equation

The starting angle equation is found by evaluating Eq. (3.15) at $\omega = \pi$.

$$-\sqrt{(1 - \xi_p^2)} \frac{\partial}{\partial r} \psi_{p,1/2} + \xi_p \frac{\partial}{\partial z} \psi_{p,1/2} + \bar{\Sigma}_t \psi_{p,1/2} = Q \quad (3.34)$$

Applying the simple corner balance approach yields

$$\begin{aligned} \sqrt{(1 - \xi_p^2)} L_{ij}^r \vec{\psi}_{p,1/2,ij}^r + \xi_p L_{ij}^z \vec{\psi}_{p,1/2,ij}^z + \left[\sqrt{(1 - \xi_p^2)} K_{ij}^r \right. \\ \left. + \xi_p K_{ij}^z + \bar{\Sigma}_t T_{ij}^1 + \sqrt{(1 - \xi_p^2)} T_{ij}^2 \right] \vec{\psi}_{p,1/2,ij} = T_{ij}^1 \vec{Q}_{ij}, \end{aligned} \quad (3.35)$$

where

$$\vec{\psi}_{p,1/2,ij}^r = \begin{bmatrix} \psi_{p,1/2,ij,1W} & \psi_{p,1/2,ij,2E} & \psi_{p,1/2,ij,3E} & \psi_{p,1/2,ij,4W} \end{bmatrix}^T, \quad (3.36a)$$

$$\vec{\psi}_{p,1/2,ij}^z = \begin{bmatrix} \psi_{p,1/2,ij,1S} & \psi_{p,1/2,ij,2S} & \psi_{p,1/2,ij,3N} & \psi_{p,1/2,ij,4N} \end{bmatrix}^T, \quad (3.36b)$$

$$\vec{\psi}_{p,1/2,ij} = \begin{bmatrix} \psi_{p,1/2,ij,1} & \psi_{p,1/2,ij,2} & \psi_{p,1/2,ij,3} & \psi_{p,1/2,ij,4} \end{bmatrix}^T. \quad (3.36c)$$

Note that some of linear operators in Eq. (3.35) differ from those in Eq. (3.30). The linear operators specific to the starting angle equation are detailed in Appendix C.

The upwinding definitions are

$$\begin{bmatrix} \psi_{p,1/2,ij,1W} \\ \psi_{p,1/2,ij,2E} \\ \psi_{p,1/2,ij,3E} \\ \psi_{p,1/2,ij,4W} \end{bmatrix} = \begin{bmatrix} \psi_{p,1/2,ij,1} \\ \psi_{p,1/2,i+1,j,1} \\ \psi_{p,1/2,i+1,j,4} \\ \psi_{p,1/2,ij,4} \end{bmatrix}, \quad (3.37a)$$

$$\begin{bmatrix} \psi_{p,1/2,ij,1S} \\ \psi_{p,1/2,ij,2S} \\ \psi_{p,1/2,ij,3N} \\ \psi_{p,1/2,ij,4N} \end{bmatrix} = \begin{cases} \begin{bmatrix} \psi_{p,1/2,ij,1} & \psi_{p,1/2,ij,2} & \psi_{p,1/2,ij-1,2} & \psi_{p,1/2,ij-1,1} \end{bmatrix}^T, & \xi < 0 \\ \begin{bmatrix} \psi_{p,1/2,i,j+1,4} & \psi_{p,1/2,i,j+1,3} & \psi_{p,1/2,ij,3} & \psi_{p,1/2,ij,4} \end{bmatrix}^T, & \xi > 0 \end{cases}. \quad (3.37b)$$

Eq. (3.37a) is a result of $\mu|_{\omega=\pi} < 0$. As with Eq. (3.33), sweeps across the spatial

mesh are performed and Eq. (3.35) is solved for each cell for each angle. Once the starting angle solves are completed, the sweeps involving Eq. (3.33) can be performed.

3.1.5 Solving procedure

The process to solve Eq. (3.29) over the spatial domain for every ordinate at some time is detailed below.

1. Solve starting angle equations
 - For all ξ_p , sweep spatial mesh solving for all $\vec{\psi}_{p,1/2,ij}$
2. Solve neutron transport equations for $\mu_{pq} < 0$
 - For all (μ_{pq}, ξ_p) where $\mu_{pq} < 0$
 - Sweep spatial mesh solving for all $\vec{\psi}_{p,q,ij}$
 - Calculate $\psi_{p,q+1/2,i,j}$ with weighted diamond difference for $\vec{\psi}_{p,q+1,ij}$
 - sweep
3. Using solutions for angular fluxes where $\mu_{pq} < 0$, define reflecting boundary conditions for $\mu_{pq} > 0$ sweeps.
4. Solve neutron transport equations for $\mu_{pq} > 0$
 - For all (μ_{pq}, ξ_p) where $\mu_{pq} > 0$,
 - Sweep spatial mesh solving for all $\vec{\psi}_{p,q,ij}$

- Calculate $\psi_{p,q+1/2,i,j}$ with weighted diamond difference for $\vec{\psi}_{p,q+1/2,i,j}$
- sweep

The spatial mesh sweeps begin in the corner of the problem where boundary conditions define the exterior surface-averaged fluxes for the particular angle being considered. This is why, in the procedure above, the solves for $\mu_{pq} < 0$ must be conducted first; those solutions are needed to evaluate the reflecting boundary conditions for $\mu_{pq} > 0$. Figure 3.4 shows the starting corner for the possible combinations of positive and negative μ_{pq} and ξ_p .

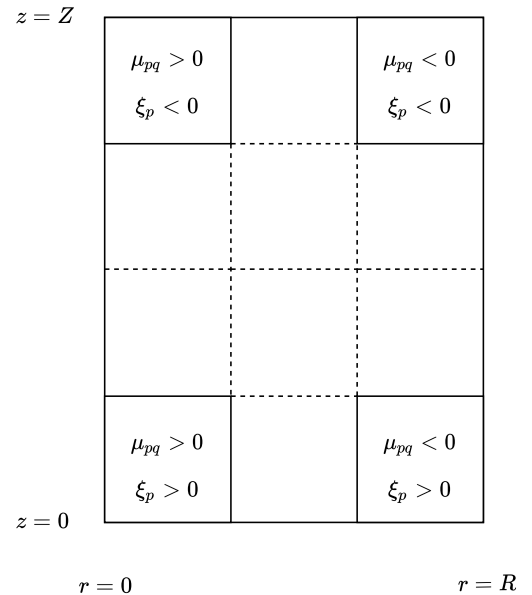


Figure 3.4: Beginning positions for spatial mesh sweeps depending on the signs of μ_{pq} and ξ_p .

3.2 Multigroup quasi-diffusion

The multigroup low-order QD (MGLOQD) problem in RZ geometry is found by taking weighted angular moments of the multigroup neutron transport equation (Eq. (3.10)) and utilizing the definitions for scalar flux and the net currents in Eq. (3.38).

$$\int_{\hat{\Omega}} \psi_g \, d\hat{\Omega} = \phi_g, \quad (3.38a)$$

$$\int_{\hat{\Omega}} \mu \, \psi_g \, d\hat{\Omega} = J_{g,r}, \quad (3.38b)$$

$$\int_{\hat{\Omega}} \xi \, \psi_g \, d\hat{\Omega} = J_{g,z}, \quad (3.38c)$$

$$\int_{\hat{\Omega}} \eta \, \psi_g \, d\hat{\Omega} = J_{g,\gamma}. \quad (3.38d)$$

The first QD equation is found by taking the angular moment weighted by 1.

$$\frac{1}{v} \frac{\partial}{\partial t} \phi_g + \frac{1}{r} \frac{\partial}{\partial r} (r J_{r,g}) + \frac{\partial}{\partial z} J_{z,g} + \Sigma_{t,g} \phi_g = Q_g. \quad (3.39)$$

The second QD equation is found by taking the angular moment weighted by μ .

$$\begin{aligned} \frac{1}{v} \frac{\partial}{\partial t} J_{r,g} + \int_{\hat{\Omega}} \frac{\partial}{\partial r} (\mu^2 \psi_g) \, d\hat{\Omega} + \int_{\hat{\Omega}} \frac{\partial}{\partial z} (\mu \xi \psi_g) \, d\hat{\Omega} \\ + \frac{1}{r} \int_{\hat{\Omega}} (2\mu^2 + \xi^2 - 1) \psi_g \, d\hat{\Omega} + \Sigma_{t,g} J_{r,g} = 0. \end{aligned} \quad (3.40)$$

Finally, the third QD equation is obtained by taking the angular moment weighted by ξ .

$$\frac{1}{v} \frac{\partial}{\partial t} J_{z,g} + \int_{\hat{\Omega}} \frac{1}{r} \frac{\partial}{\partial r} (r \mu \xi \psi_g) d\hat{\Omega} + \int_{\hat{\Omega}} \frac{\partial}{\partial z} (\xi^2 \psi_g) d\hat{\Omega} + \Sigma_{t,g} J_{z,g} = 0. \quad (3.41)$$

After introducing three definitions for the Eddington factors

$$E_{rr,g} = \frac{\int_{\hat{\Omega}} \mu^2 \psi_g d\hat{\Omega}}{\int_{\hat{\Omega}} \psi_g d\hat{\Omega}}, \quad (3.42a)$$

$$E_{zz,g} = \frac{\int_{\hat{\Omega}} \xi^2 \psi_g d\hat{\Omega}}{\int_{\hat{\Omega}} \psi_g d\hat{\Omega}}, \quad (3.42b)$$

$$E_{rz,g} = \frac{\int_{\hat{\Omega}} \mu \xi \psi_g d\hat{\Omega}}{\int_{\hat{\Omega}} \psi_g d\hat{\Omega}}, \quad (3.42c)$$

Eqs. (3.39), (3.40), and (3.41) are used to formulate the low order QD system.

$$\frac{1}{v_g} \frac{\partial}{\partial t} \phi_g + \frac{1}{r} \frac{\partial}{\partial r} (r J_{r,g}) + \frac{\partial}{\partial z} J_{z,g} + \Sigma_{t,g} \phi_g = Q_g, \quad (3.43a)$$

$$\frac{1}{v_g} \frac{\partial}{\partial t} J_{r,g} + \frac{\partial}{\partial r} (E_{rr,g} \phi_g) + \frac{\partial}{\partial z} (E_{rz,g} \phi_g) + \frac{G}{r} E_{rr,g} \phi_g + \Sigma_{t,g} J_{r,g} = 0, \quad (3.43b)$$

$$\frac{1}{v_g} \frac{\partial}{\partial t} J_{z,g} + \frac{1}{r} \frac{\partial}{\partial r} (r E_{rz,g} \phi_g) + \frac{\partial}{\partial z} (E_{zz,g} \phi_g) + \Sigma_{t,g} J_{z,g} = 0, \quad (3.43c)$$

where

$$G_g = 1 + \frac{E_{rr,g} + E_{zz,g} - 1}{E_{rr,g}}. \quad (3.44)$$

The mixed boundary conditions presented by Gol'din [36] are used on outside boundaries, and the inside boundary is reflective.

$$\hat{n} \cdot \mathbf{J}_g|_{(r,z) \in \delta D} = \begin{cases} [\mathbb{C}_g (\phi_g - \phi_g^{\text{in}}) + J_g^{\text{in}}], & r \neq 0 \\ 0, & r = 0 \end{cases}, \quad (3.45)$$

where

$$\mathbb{C}_g = \frac{\int_{\hat{n} \cdot \hat{\Omega} > 0} \hat{n} \cdot \hat{\Omega} \psi_g d\hat{\Omega}}{\int_{\hat{n} \cdot \hat{\Omega} > 0} \psi_g d\hat{\Omega}}, \quad (3.46a)$$

$$\phi_g^{\text{in}} = \int_{\hat{n} \cdot \hat{\Omega} < 0} \psi_g d\hat{\Omega}, \quad (3.46b)$$

$$J_g^{\text{in}} = \int_{\hat{n} \cdot \hat{\Omega} < 0} \hat{n} \cdot \hat{\Omega} \psi_g d\hat{\Omega}. \quad (3.46c)$$

The source term Q_g of Eq. (3.39) is formulated using the grey group flux ϕ and ψ_g , differentiating it from the source term in Eq. (3.15).

$$Q_g = \sum_{g'=1}^g \Sigma_{s,g' \rightarrow g} \phi_{g'} + \left(\frac{\sum_{g'=g+1}^G \Sigma_{s,g' \rightarrow g} \phi_{g'}}{\sum_{g'=g+1}^G \phi_{g'}} + \chi_g^p (1 - \beta) \nu \Sigma_f \right) \phi + \sum_{d=1}^{N_d} \lambda_d \chi_g^d C_d. \quad (3.47)$$

Down and within-group scattering sources are calculating using group fluxes while upscattering and fission sources are calculated using the grey group flux. The upscatter coefficient is calculated with a simple flux-weighted average.

3.2.1 Transport coupling

The multigroup QD system of Eq. (3.43) is a low-order formulation of Eq. (3.15) and, up to this point, has been formulated without approximation. The reduction in order occurs as Eq. (3.43) has no dependence on angle. Where the solution to the transport problem required a sweep across the quadrature set, no such sweep is required here, an obvious advantage computationally.

Transport effects, however, are still captured. The angular dependence of the transport solution is projected into the low-order, multigroup problem using a number of linear fractional functionals - the Eddington factors and boundary parameters defined in Eqs. (3.42) and (3.46).

Although some estimate of the transport solution is still required to formulate the low-order problem, the estimate need not be converged with respect the angular group flux ψ_g . Instead, only the estimates of the Eddington factors, calculated with ψ_g , be converged. This requirement is less onerous as the Eddington factors are weakly dependent on the transport solution as noted by Adams and Larsen [52]. Combined with a single group QD formulation with multiphysics coupling, described in Section 3.3, these low-order formulations accelerate the solution of the original problem in Eq. (3.1a).

Note that the QD mesh is defined by the subcell mesh of the transport problem, as shown in Figure 3.5. Section 3.1 describes cells which are composed of four corners. In this work, the corner values are not combined to define cell values; the corner values of the transport solution are used directly to define the fractional

functionals on the QD mesh.

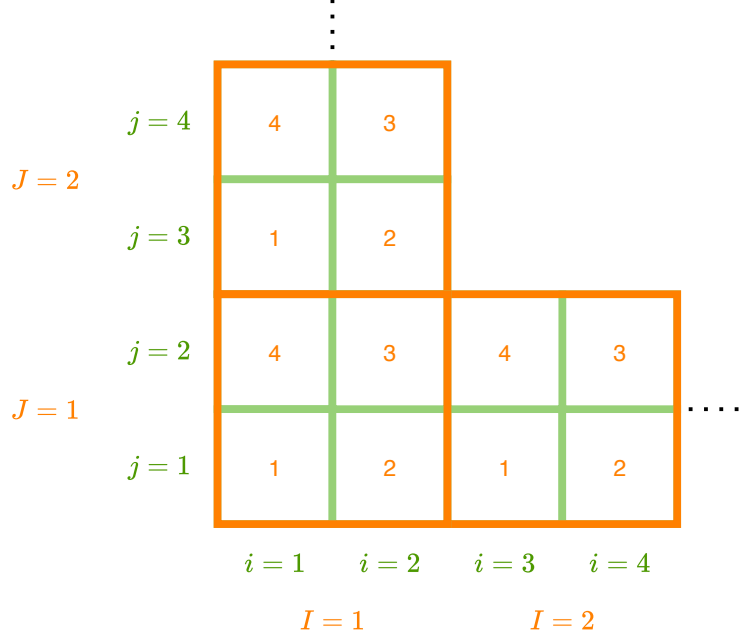


Figure 3.5: Relationship between the simple corner balance and quasi-diffusion notation. The simple corner balance notation is in orange with uppercase (I, J) indices. The quasi-diffusion notation is in green with lowercase (i, j) indices. For example, a quantity at $(i, j) = (3, 2)$ is consistent with position 4 of $(I, J) = (2, 1)$ in the simple corner balance notation.

3.2.2 Integrating factor

The approach of Jones et al. [53] is utilized to simplify Eq. (3.43b) through the use of an integrating factor

$$h_{g,ij}(r) = r^{\bar{G}_{g,ij}}, \text{ for } r, z \in C_{ij}, \quad (3.48)$$

where

$$\overline{G}_{g,ij} = \frac{\int_i \int_j r G_g \, dz \, dr}{\int_i \int_j r \, dz \, dr} \quad (3.49)$$

and the short hand

$$\int_i \equiv \int_{r_{i-1/2}}^{r_{i+1/2}}, \quad \int_j \equiv \int_{z_{j-1/2}}^{z_{j+1/2}}$$

has been introduced. Multiplying by the intergrating factor, combining the second and fourth terms of Eq. (3.43b) using the product rule, and then dividing by the integrating factor yields Eq. (3.51).

$$\frac{1}{v_g} \frac{\partial}{\partial t} J_{r,g} + \frac{1}{h_{g,ij}} \frac{\partial}{\partial r} (h_{g,ij} E_{rr,g} \phi_g) + \frac{\partial}{\partial z} (E_{rz,g} \phi_g) + \Sigma_{t,g} J_{r,g} = 0. \quad (3.51)$$

Similarly following the approach of Jones et al., an alternate expression for $h_{g,ij}$, Eq. (3.52) with $P = 2$, is used when evaluating in cells with a face on the reflecting boundary ($r = 0$). This ensures ensure that the $\overline{G}_{g,ij}/r$ component of the derivative in the second term of Eq. (3.51) doesn't become unstable.

$$h_{g,ij}(r) = \exp \left(g_0 \frac{r^P}{P} + g_1 \frac{r^{P+1}}{P+1} \right), \quad (3.52)$$

where g_0 and g_1 satisfy

$$r_{i+1/2}^P (g_0 + g_1 r_{i+1/2}) = G_g (r_{i+1/2}, z_j), \quad (3.53a)$$

$$r_i^P (g_0 + g_1 r_i) = G_g (r_i, z_j), \quad (3.53b)$$

reproducing G_g at r_i and $r_{i+1/2}$.

With the integrating factor, the multigroup QD system becomes

$$\frac{1}{v_g} \frac{\partial}{\partial t} \phi_g + \frac{1}{r} \frac{\partial}{\partial r} (r J_{r,g}) + \frac{\partial}{\partial z} J_{z,g} + \Sigma_{t,g} \phi_g = Q_g, \quad (3.54a)$$

$$\frac{1}{v_g} \frac{\partial}{\partial t} J_{r,g} + \frac{1}{h_{g,ij}} \frac{\partial}{\partial r} (h_{g,ij} E_{rr,g} \phi_g) + \frac{\partial}{\partial z} (E_{rz,g} \phi_g) + \Sigma_{t,g} J_{r,g} = 0. \quad (3.54b)$$

$$\frac{1}{v_g} \frac{\partial}{\partial t} J_{z,g} + \frac{1}{r} \frac{\partial}{\partial r} (r E_{rz,g} \phi_g) + \frac{\partial}{\partial z} (E_{zz,g} \phi_g) + \Sigma_{t,g} J_{z,g} = 0. \quad (3.54c)$$

3.2.3 Discretization

First, the introduction of definitions for the volume-averaged flux and source,

$$\phi_{ij}^n = \frac{1}{V_{ij}} \int_i r \int_j \phi^n \, dz \, dr, \quad (3.55)$$

$$Q_{ij}^n = \frac{1}{V_{ij}} \int_i r \int_j Q^n \, dz \, dr, \quad (3.56)$$

the surface-averaged fluxes,

$$\phi_{i+1/2,j}^n = \frac{2\pi r_{i+1/2}}{A_{i+1/2,j}} \int_j \phi^n \, dz, \quad (3.57)$$

$$\phi_{i,j+1/2}^n = \frac{2\pi}{B_i} \int_i r \, \phi^n \, dr, \quad (3.58)$$

and the surface-averaged currents,

$$J_{r,i+1/2,j}^n = \frac{2\pi r_{i+1/2}}{A_{i+1/2,j}} \int_j J_r^n dz, \quad (3.59)$$

$$J_{z,i,j+1/2}^n = \frac{2\pi}{B_i} \int_i r J_z^n dr, \quad (3.60)$$

where

$$V_{ij} = 2\pi \int_i r \int_j dz dr, \quad (3.61)$$

and $A_{i+1/2,j}$ and B_i are the vertical and horizontal surface areas,

$$A_{i+1/2,j} = 2\pi r_{i+1/2} \int_j dz, \quad (3.62)$$

$$B_i = 2\pi \int_i r dr. \quad (3.63)$$

The group index g has been left off for compactness.

The definitions for cell and interface Eddington factors, which are calculated from the transport solution, are also introduced. As the corner values of the transport solution are used directly, the volume-weighted, arithmetic mean of the volume-averaged angular fluxes on either side of an interface is used for calculating the interface Eddington factors.

$$E_{xy,ij} = \frac{\sum_{p=0}^P \sum_{q=0}^{Q_p} \hat{\Omega}_{x,pq} \hat{\Omega}_{y,pq} \psi_{pq,ij} w_{pq}}{\sum_{p=0}^P \sum_{q=0}^{Q_p} \psi_{pq,ij} w_{pq}}, \quad (3.64a)$$

$$E_{xy,i+1/2,j} = \frac{\sum_{p=0}^P \sum_{q=0}^{Q_p} \hat{\Omega}_{x,pq} \hat{\Omega}_{y,pq} \psi_{pq,i+1/2,j} w_{pq}}{\sum_{p=0}^P \sum_{q=0}^{Q_p} \psi_{pq,i+1/2,j} w_{pq}}, \quad (3.64b)$$

where

$$\psi_{pq,i+1/2,j} = \frac{V_{ij}\psi_{pq,ij} + V_{i+1,j}\psi_{pq,i+1,j}}{V_{ij} + V_{i+1,j}}. \quad (3.65)$$

and $x, y \in (r, z)$. An analogous expression to Eq. (3.64b) is used for horizontal interfaces. Note that the (i, j) notation used on angular fluxes differs from that of Section 3.1. Here, (i, j) reference a cell on the QD mesh, as mentioned in Section 3.2.1.

Eq. (3.54a), the zeroth moment QD equation, is discretized by integrating over a unit cell with bounds $r \in [r_{i-\frac{1}{2}}, r_{i+\frac{1}{2}}]$, $z \in [z_{j-\frac{1}{2}}, z_{j+\frac{1}{2}}]$ over a time step $t \in [t^{n-1}, t^n]$. An implicit time scheme is used.

$$\begin{aligned} & \frac{V_{ij}}{v} (\phi_{ij}^n - \phi_{ij}^{n-1}) + 2\pi\Delta z_j (r_{i+\frac{1}{2}} J_{i+\frac{1}{2},j}^n - r_{i-\frac{1}{2}} J_{i-\frac{1}{2},j}^n) \\ & + \Delta t^n \pi (r_{i+\frac{1}{2}}^2 - r_{i-\frac{1}{2}}^2) (J_{i,j+\frac{1}{2}}^n - J_{i,j-\frac{1}{2}}^n) + \Delta t^n V_{ij} \Sigma_t \phi_{ij}^n = \Delta t^n V_{ij} Q_{ij}^n. \end{aligned} \quad (3.66)$$

The approach of Morel [54] is used, adapted for our simpler structured mesh, in discretizing the first moment equations, namely to approximate the spatial derivatives. The result is a discretized first moment equation for each face of the cell, with straight-forward differencing schemes to approximate the spatial derivatives.

$$\begin{aligned} & \frac{1}{v\Delta t} (J_{r,i+\frac{1}{2},j}^n - J_{r,i-\frac{1}{2},j}^{n-1}) + \frac{1}{h_{i+\frac{1}{2},j}} \frac{h_{i+\frac{1}{2},j} E_{rr,i+\frac{1}{2},j}^n \phi_{i+\frac{1}{2},j}^n - h_{ij} E_{rr,ij}^n \phi_{ij}^n}{r_{i+\frac{1}{2}} - r_i} \\ & + \frac{E_{rz,i,j+\frac{1}{2}}^n \phi_{i,j+\frac{1}{2}}^n - E_{rz,i,j-\frac{1}{2}}^n \phi_{i,j-\frac{1}{2}}^n}{\Delta z_{ij}} + \Sigma_t J_{r,i+\frac{1}{2},j}^n = 0, \end{aligned} \quad (3.67a)$$

$$\begin{aligned} \frac{1}{v\Delta t} \left(J_{r,i-\frac{1}{2},j}^n - J_{r,i-\frac{1}{2},j}^{n-1} \right) + \frac{1}{h_{i-\frac{1}{2},j}} \frac{h_{ij} E_{rr,ij}^n \phi_{ij}^n - h_{i-\frac{1}{2},j} E_{rr,i-\frac{1}{2},j}^n \phi_{i-\frac{1}{2},j}^n}{r_i - r_{i-\frac{1}{2}}} \\ + \frac{E_{rz,i,j+\frac{1}{2}}^n \phi_{i,j+\frac{1}{2}}^n - E_{rz,i,j-\frac{1}{2}}^n \phi_{i,j-\frac{1}{2}}^n}{\Delta z_{ij}} + \Sigma_t J_{r,i-\frac{1}{2},j}^n = 0, \quad (3.67b) \end{aligned}$$

$$\begin{aligned} \frac{1}{v\Delta t} \left(J_{z,i,j+\frac{1}{2}}^n - J_{z,i,j+\frac{1}{2}}^{n-1} \right) + \frac{1}{r_i} \frac{r_{i+\frac{1}{2}} E_{rz,i+\frac{1}{2},j}^n \phi_{i+\frac{1}{2},j}^n - r_{i-\frac{1}{2}} E_{rz,i-\frac{1}{2},j}^n \phi_{i-\frac{1}{2},j}^n}{\Delta r_{ij}} \\ + \frac{E_{zz,i,j+\frac{1}{2}}^n \phi_{i,j+\frac{1}{2}}^n - E_{zz,i,j-\frac{1}{2}}^n \phi_{i,j-\frac{1}{2}}^n}{z_{j+\frac{1}{2}} - z_j} + \Sigma_t J_{z,i,j+\frac{1}{2}}^n = 0, \quad (3.67c) \end{aligned}$$

$$\begin{aligned} \frac{1}{v\Delta t} \left(J_{z,i,j-\frac{1}{2}}^n - J_{z,i,j-\frac{1}{2}}^{n-1} \right) + \frac{1}{r_i} \frac{r_{i+\frac{1}{2}} E_{rz,i+\frac{1}{2},j}^n \phi_{i+\frac{1}{2},j}^n - r_{i-\frac{1}{2}} E_{rz,i-\frac{1}{2},j}^n \phi_{i-\frac{1}{2},j}^n}{\Delta r_{ij}} \\ + \frac{E_{zz,ij}^n \phi_{ij}^n - E_{zz,i,j-\frac{1}{2}}^n \phi_{i,j-\frac{1}{2}}^n}{z_j - z_{j-\frac{1}{2}}} + \Sigma_t J_{z,i,j-\frac{1}{2}}^n = 0, \quad (3.67d) \end{aligned}$$

Boundary and interface conditions provide the remaining equations to solve Eq. (3.54) in one cell. On shared faces, current and flux continuity are enforced.

$$J_{z,i,j+\frac{1}{2}}^n = J_{z,i,(j+1)-\frac{1}{2}}^n, \quad (3.68a)$$

$$J_{r,i+\frac{1}{2},j}^n = J_{r,(i+1)-\frac{1}{2},j}^n, \quad (3.68b)$$

$$\phi_{i,j+\frac{1}{2}}^n = \phi_{i,(j+1)-\frac{1}{2}}^n, \quad (3.68c)$$

$$\phi_{i+\frac{1}{2},j}^n = \phi_{(i+1)-\frac{1}{2},j}^n, \quad (3.68d)$$

The discretized boundary condition is

$$\hat{n}_{ij,f} \cdot \mathbf{J}_{g,ij,f}|_{(r,z) \in \delta D} = \begin{cases} [\mathbb{C}_{g,ij,f} (\phi_{g,ij,f} - \phi_{g,ij,f}^{\text{in}}) + J_{g,ij,f}^{\text{in}}], & r_{i,f} \neq 0 \\ 0, & r_{i,f} = 0 \end{cases}, \quad (3.69)$$

where

$$\mathbb{C}_{g,ij,f} = \frac{\sum_{\hat{n} \cdot \hat{\Omega} > 0} \hat{n}_{ij,f} \cdot \hat{\Omega}_{pq} \psi_{g,ij,f,pq} w_{pq}}{\sum_{\hat{n} \cdot \hat{\Omega} > 0} \psi_{g,ij,f,pq} w_{pq}}, \quad (3.70a)$$

$$\phi_{g,ij,f}^{\text{in}} = \sum_{\hat{n} \cdot \hat{\Omega} < 0} \psi_{g,ij,f,pq} w_{pq}, \quad (3.70b)$$

$$J_{g,ij,f}^{\text{in}} = \sum_{\hat{n} \cdot \hat{\Omega} < 0} \hat{n}_{ij,f} \cdot \hat{\Omega}_{pq} \psi_{g,ij,f,pq} w_{pq}, \quad (3.70c)$$

and the ij, f subscript indicates a parameter evaluation at a boundary face of cell ij .

3.2.4 Linear system

Assuming redundant unknowns have been eliminated, an orthogonal rectangular NxM mesh, pictured in Figure 3.6, for a problem with G neutron energy groups has $G(5NM+2N+2M)$ unknowns. Details on these unknowns are listed in Table 3.2.

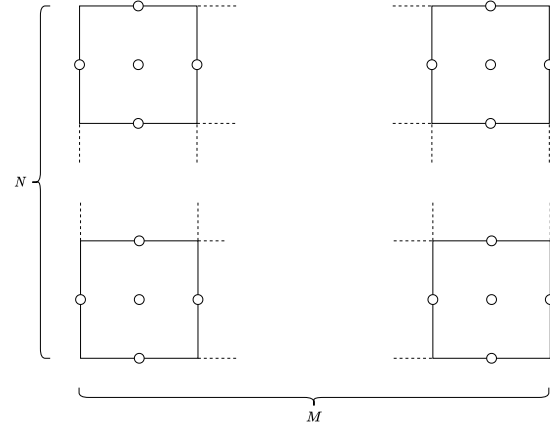


Figure 3.6: An $N \times M$ mesh. Unknowns are marked with a circle.

Table 3.2: Breakdown of unknowns in multigroup quasidiffusion solve.

Variable	Number of unknowns
Volume-averaged fluxes	GNM
Surface-averaged fluxes	$G(2NM+N+M)$
Surface averaged currents	$G(2NM+N+M)$

The linear system to approximate the solution for the multigroup QD level, Eq. (3.54), is formed with the conditions detailed in Table 3.3.

Table 3.3: Equations used to form the linear system used in solving the multigroup QD level. N_{eq} is the number of times an equation is used in the linear system.

Condition	Full system N_{eq}	Reduced system N_{eq}
Eq. (3.66): zeroth moment	GNM	GNM
Eq. (3.67): first moment	4GNM	0
Eq. (3.67): interface condition	0	G(2NM-N-M)
Eq. (3.69): boundary condition	2G(N+M)	2G(N+M)

As found by Jones [55], a reduced system can be formed which completely eliminates the surface currents. This is accomplished by using Eq. (3.67), the first moment equations, to obtain expressions for the surface-averaged currents at t_n in terms of the surface- and volume-averaged fluxes at t_n and the surface-averaged currents at t_{n-1} . These expressions are used in place of the surface-averaged currents at t_n in Eq. (3.66), the zeroth moment equation, and to enforce current continuity on shared faces, i.e. the interface conditions mentioned in Table 3.3.

Without the currents, the reduced system has $G(3NM+N+M)$ unknowns, which will likely yield increased computational efficiency. After solving for the surface- and volume-averaged fluxes, those values are used to back calculate the surface-averaged currents at t_n , with simple matrix multiplication, to be used in solving for the next time step.

3.3 Effective low-order transport

The effective low-order transport (ELOT) problem is composed of one-group QD equations, the heat equation, and the DNP balance equations. The system is formulated with collapsed data calculated from the multigroup data, scalar fluxes, and net currents to preserve reaction rates.

$$\frac{1}{v} \frac{\partial}{\partial t} \phi + \frac{1}{r} \frac{\partial}{\partial r} (r J_r) + \frac{\partial}{\partial z} J_z + \bar{\Sigma}_a \phi = \overline{(1 - \beta) \nu \Sigma_f} \phi + \sum_{d=1}^{N_D} \lambda_d C_d, \quad (3.71a)$$

$$\frac{1}{\tilde{v}} \frac{\partial}{\partial t} (J_r) + \frac{1}{h_i} \frac{\partial}{\partial r} (h_i \bar{E}_{rr} \phi) + \frac{\partial}{\partial z} (\bar{E}_{rz} \phi) + \hat{\Sigma}_{tr} J_r + \hat{\zeta} \phi = 0, \quad (3.71b)$$

$$\frac{1}{\tilde{v}} \frac{\partial}{\partial t} (J_z) + \frac{1}{r} \frac{\partial}{\partial r} (r \bar{E}_{rz} \phi) + \frac{\partial}{\partial z} (\bar{E}_{zz} \phi) + \tilde{\Sigma}_{tr} J_z + \tilde{\zeta} \phi = 0, \quad (3.71c)$$

$$\frac{\partial}{\partial t} C_d + \frac{\partial}{\partial z} (\vec{u} C_d) = -\lambda_d C_d + \overline{\beta \nu \Sigma_f} \phi, \quad d = 1, \dots, N_d, \quad (3.71d)$$

$$\frac{\partial}{\partial t} (\rho c_p T) - \frac{\kappa}{r} \frac{\partial}{\partial r} \left(r \frac{\partial}{\partial r} T \right) - \kappa \frac{\partial^2}{\partial z^2} T + \frac{\partial}{\partial z} (\vec{u} \rho c_p T) = Q_m + Q_f, \quad (3.71e)$$

where

$$\bar{\Sigma}_a = \frac{\sum_{g=1}^G (\Sigma_{t,g} - \Sigma_{s,g}) \phi_g}{\sum_{g=1}^G \phi_g}, \quad (3.72a)$$

$$\overline{(1 - \beta) \nu \Sigma_f} = \frac{\sum_{g=1}^G (1 - \beta_g) \nu_g \Sigma_{f,g} \phi_g}{\sum_{g=1}^G \phi_g}, \quad (3.72b)$$

$$\hat{\Sigma}_{tr} = \frac{\sum_{g=1}^G \Sigma_{t,g} |J_{r,g}|}{\sum_{g=1}^G |J_{r,g}|}, \quad (3.72c)$$

$$\tilde{\Sigma}_{tr} = \frac{\sum_{g=1}^G \Sigma_{t,g} |J_{z,g}|}{\sum_{g=1}^G |J_{z,g}|}, \quad (3.72d)$$

$$\bar{v} = \frac{\sum_{g=1}^G \phi_g}{\sum_{g=1}^G (\phi_g / v_g)}, \quad (3.72e)$$

$$\hat{v} = \frac{\sum_{g=1}^G |J_{r,g}|}{\sum_{g=1}^G (|J_{r,g}| / v_g)}, \quad (3.72f)$$

$$\tilde{v} = \frac{\sum_{g=1}^G |J_{z,g}|}{\sum_{g=1}^G (|J_{z,g}| / v_g)}, \quad (3.72g)$$

$$\bar{E}_{xy} = \frac{\sum_{g=1}^G E_{xy} \phi_g}{\sum_{g=1}^G \phi_g}, \text{ for } x, y \in \{r, z\}, \quad (3.72h)$$

and

$$\hat{\zeta} = \hat{\zeta}_1 + \hat{\zeta}_2, \quad (3.73a)$$

$$\tilde{\zeta} = \tilde{\zeta}_1 + \tilde{\zeta}_2, \quad (3.73b)$$

where

$$\hat{\zeta}_1 = \frac{\frac{\partial}{\partial t} \left(\sum_{g=1}^G \left[\frac{1}{v_g} - \frac{1}{\hat{v}} \right] J_{r,g} \right)}{\sum_{g=1}^G \phi_g}, \quad \hat{\zeta}_2 = \frac{\sum_{g=1}^G \left[\Sigma_{t,g} - \hat{\Sigma}_{tr} \right] J_{r,g}}{\sum_{g=1}^G \phi_g}, \quad (3.74a)$$

$$\tilde{\zeta}_1 = \frac{\frac{\partial}{\partial t} \left(\sum_{g=1}^G \left[\frac{1}{v_g} - \frac{1}{\hat{v}} \right] J_{z,g} \right)}{\sum_{g=1}^G \phi_g}, \quad \tilde{\zeta}_2 = \frac{\sum_{g=1}^G \left[\Sigma_{t,g} - \tilde{\Sigma}_{tr} \right] J_{z,g}}{\sum_{g=1}^G \phi_g}. \quad (3.74b)$$

The ζ terms in Eqs. (3.71b) and (3.71c) allow for reaction rates to be preserved between the multigroup and one-group formulation while collapsing some data (Eqs. (3.72c), (3.72d), (3.72f), (3.72g)) with respect to the absolute value of the currents. If one performed the collapse without taking the absolute value, negative collapsed cross sections and particle speed may result, both of which are non-

physical.

The fission and moderator energy source terms in Eq. (3.71e) are

$$Q_f = \omega_f \bar{\Sigma}_f \phi, \quad (3.75)$$

$$Q_m = \begin{cases} \frac{\gamma}{V_{\text{core}}} \int_{\text{core}} Q_f \, dV, & \text{in moderator} \\ 0, & \text{otherwise} \end{cases}, \quad (3.76)$$

where

$$\bar{\Sigma}_F = \frac{\sum_{g=1}^G \Sigma_{f,g} \phi_g}{\sum_{g=1}^G \phi_g}. \quad (3.77)$$

and $\gamma = 0.0144$, as mentioned in Section 3.

The boundary conditions for Eqs. (3.71a), (3.71b), and (3.71c), the QD equations, are

$$\hat{n} \cdot \mathbf{J}|_{(r,z) \in \delta D} = \begin{cases} \left[\tilde{\mathbb{C}} (\phi - \phi^{\text{in}}) + J^{\text{in}} \right], & r \neq 0 \\ 0, & r = 0 \end{cases}, \quad (3.78)$$

where

$$\tilde{\mathbb{C}} = \frac{\sum_{g=1}^G \mathbb{C}_g (\phi_g - \phi_g^{\text{in}})}{\sum_{g=1}^G (\phi_g - \phi_g^{\text{in}})}, \quad (3.79a)$$

$$\phi^{\text{in}} = \sum_{g=1}^G \phi_g^{\text{in}}, \quad (3.79b)$$

$$J^{\text{in}} = \sum_{g=1}^G J_g^{\text{in}}. \quad (3.79c)$$

The boundary conditions for the DNP and energy balance equations are unchanged from Eqs. (3.9) and (3.8). They are reproduced here for convenience.

$$C_d|_{z=0} = C_d^{\text{in}},$$

$$\left[\frac{\partial}{\partial r} C_d \right]_{z=Z} = 0,$$

$$T = \begin{cases} T_{\text{in}}, & z = 0 \\ T_{\text{wall}}, & r = R \end{cases},$$

$$\left[\frac{\partial}{\partial r} T \right]_{r=0} = 0,$$

$$\left[\frac{\partial}{\partial z} T \right]_{z=Z} = 0.$$

3.3.1 One-group QD discretization

The discretizations for the one-group QD equations largely follow those described in Section 3.2.3. The discretized zeroth moment equation, Eq. (3.80), differs from the multigroup equivalent in the approximation to the time derivative; the collapsed neutron speeds at t^n and t^{n-1} factor into the one-group formulation.

$$\begin{aligned}
& V_{ij} \left(\frac{\phi_{ij}^n}{\bar{v}^n} - \frac{\phi_{ij}^{n-1}}{\bar{v}^{n-1}} \right) + 2\pi \Delta z_j \left(r_{i+\frac{1}{2}} J_{i+\frac{1}{2},j}^n - r_{i-\frac{1}{2}} J_{i-\frac{1}{2},j}^n \right) \\
& + \Delta t^n \pi \left(r_{i+\frac{1}{2}}^2 - r_{i-\frac{1}{2}}^2 \right) \left(J_{i,j+\frac{1}{2}}^n - J_{i,j-\frac{1}{2}}^n \right) + \Delta t^n V_{ij} \Sigma_t \phi_{ij}^n = \Delta t^n V_{ij} Q_{ij}^n. \quad (3.80)
\end{aligned}$$

The discretized first moment equations, Eq. (3.81), differ by inclusion of the ξ terms as well as in the approximation to the time derivative, where the group currents at t^{n-1} are used in place of the one-group current J^{n-1} .

$$\begin{aligned}
& \frac{1}{\Delta t^n} \left(\frac{J_{r,i+\frac{1}{2},j}^n}{\hat{v}^n} - \sum_{g=1}^G \frac{J_{r,g,i+\frac{1}{2},j}^{n-1}}{v_g} \right) + \frac{1}{h_{i+\frac{1}{2},j}^R} \frac{h_{i+\frac{1}{2},j}^R E_{rr,i+\frac{1}{2},j}^n \phi_{i+\frac{1}{2},j}^n - h_{ij}^R E_{rr,ij}^n \phi_{ij}^n}{r_{i+\frac{1}{2}} - r_i} \\
& + \frac{E_{rz,i,j+\frac{1}{2}}^n \phi_{i,j+\frac{1}{2}}^n - E_{rz,i,j-\frac{1}{2}}^n \phi_{i,j-\frac{1}{2}}^n}{\Delta z_j} + \hat{\Sigma}_{tr,i+\frac{1}{2},j} J_{r,i+\frac{1}{2},j}^n + \hat{\xi}_{i+\frac{1}{2},j} \phi_{i+\frac{1}{2},j}^n = 0, \quad (3.81a)
\end{aligned}$$

$$\begin{aligned}
& \frac{1}{\Delta t^n} \left(\frac{J_{r,i-\frac{1}{2},j}^n}{\hat{v}^n} - \sum_{g=1}^G \frac{J_{r,g,i-\frac{1}{2},j}^{n-1}}{v_g} \right) + \frac{1}{h_{i-\frac{1}{2},j}^L} \frac{h_{ij}^L E_{rr,ij}^n \phi_{ij}^n - h_{i-\frac{1}{2},j}^L E_{rr,i-\frac{1}{2},j}^n \phi_{i-\frac{1}{2},j}^n}{r_i - r_{i-\frac{1}{2}}} \\
& + \frac{E_{rz,i,j+\frac{1}{2}}^n \phi_{i,j+\frac{1}{2}}^n - E_{rz,i,j-\frac{1}{2}}^n \phi_{i,j-\frac{1}{2}}^n}{\Delta z_j} + \hat{\Sigma}_{tr,i-\frac{1}{2},j} J_{r,i-\frac{1}{2},j}^n + \hat{\xi}_{i-\frac{1}{2},j} \phi_{i-\frac{1}{2},j}^n = 0, \quad (3.81b)
\end{aligned}$$

$$\begin{aligned}
& \frac{1}{\Delta t^n} \left(\frac{J_{z,i,j+\frac{1}{2}}^n}{\tilde{v}^n} - \sum_{g=1}^G \frac{J_{z,g,i,j+\frac{1}{2}}^{n-1}}{v_g} \right) + \frac{1}{r_i} \frac{r_{i+\frac{1}{2}} E_{rz,i+\frac{1}{2},j}^n \phi_{i+\frac{1}{2},j}^n - r_{i-\frac{1}{2}} E_{rz,i-\frac{1}{2},j}^n \phi_{i-\frac{1}{2},j}^n}{\Delta r_i} \\
& + \frac{E_{zz,i,j+\frac{1}{2}}^n \phi_{i,j+\frac{1}{2}}^n - E_{zz,ij}^n \phi_{ij}^n}{z_{j+\frac{1}{2}} - z_j} + \tilde{\Sigma}_{tr,i,j+\frac{1}{2}} J_{z,i,j+\frac{1}{2}}^n + \tilde{\xi}_{i,j+\frac{1}{2}} \phi_{i,j+\frac{1}{2}}^n = 0, \quad (3.81c)
\end{aligned}$$

$$\begin{aligned} & \frac{1}{\Delta t^n} \left(\frac{J_{z,i,j-\frac{1}{2}}^n}{\tilde{v}^n} - \sum_{g=1}^G \frac{J_{z,g,i,j-\frac{1}{2}}^{n-1}}{v_g} \right) + \frac{1}{r_i} \frac{r_{i+\frac{1}{2}} E_{rz,i+\frac{1}{2},j}^n \phi_{i+\frac{1}{2},j}^n - r_{i-\frac{1}{2}} E_{rz,i-\frac{1}{2},j}^n \phi_{i-\frac{1}{2},j}^n}{\Delta r_i} \\ & + \frac{E_{zz,ij}^n \phi_{ij}^n - E_{zz,i,j-\frac{1}{2}}^n \phi_{i,j-\frac{1}{2}}^n}{z_j - z_{j-\frac{1}{2}}} + \tilde{\Sigma}_{tr,i,j-\frac{1}{2}} J_{z,i,j-\frac{1}{2}}^n + \tilde{\xi}_{i,j-\frac{1}{2}} \phi_{i,j-\frac{1}{2}}^n = 0. \quad (3.81d) \end{aligned}$$

The R and L superscripts on the integrating factors h denote the use of G^R or G^L , which satisfy

$$\left(\frac{r_i}{r_{i+\frac{1}{2}}} \right)^{G^R} = \frac{\sum_{g=1}^{N_g} \left(\frac{r_i}{r_{i+\frac{1}{2}}} \right)^{G_g} E_{rr,i+\frac{1}{2},j}^n \phi_{i+\frac{1}{2},j}^n}{\sum_{g=1}^{N_g} E_{rr,i+\frac{1}{2},j}^n \phi_{i+\frac{1}{2},j}^n}, \quad (3.82)$$

$$\left(\frac{r_i}{r_{i-\frac{1}{2}}} \right)^{G^L} = \frac{\sum_{g=1}^{N_g} \left(\frac{r_i}{r_{i-\frac{1}{2}}} \right)^{G_g} E_{rr,i-\frac{1}{2},j}^n \phi_{i-\frac{1}{2},j}^n}{\sum_{g=1}^{N_g} E_{rr,i-\frac{1}{2},j}^n \phi_{i-\frac{1}{2},j}^n}. \quad (3.83)$$

This two-sided collapse of G is necessary to preserve reaction rates between the MGLOQD and ELOT levels.

As described in Section 3.2.4, the first moment equations can be used to find expressions for the surface-averaged currents at t^n , and those expressions can be used to eliminate dependence on the surface-averaged currents at t^n entirely. Doing so and formulating a linear system with evaluations of the discretized equations across an NxM spatial mesh yields a system of size 3NM+N+M. Additional details on the full linear system, which also governs the temperatures and DNP concentrations, are presented in Section 3.3.4.

3.3.2 DNP balance discretization

The DNP balance equations are discretized with a finite volume approach. Integrating Eq. (3.71d) over a cell with $r \in (r_{i-1/2}, r_{i+1/2})$, $z \in (z_{j-1/2}, z_{j+1/2})$ from $t \in (t^{n+1}, t^n)$ yields

$$\begin{aligned} (C_{d,ij}^n - C_{d,ij}^{n-1}) + \frac{2\pi \Delta t^n}{V_{ij}} \int_i r \int_j \frac{\partial}{\partial z} (\vec{u} C_d) dz dr \\ = \Delta t^n (-\lambda_d C_{d,ij}^n + \overline{\beta \nu \Sigma_f}_d \phi_{ij}^n), \end{aligned} \quad (3.84)$$

where

$$C_{d,ij}^n = \frac{2\pi}{V_{ij}} \int_i r \int_j C_d^n dz dr. \quad (3.85)$$

The approach described by Leveque [56] is used to approximate the advection term.

$$\frac{2\pi \Delta t^n}{V_{ij}} \int_i r \int_j \frac{\partial}{\partial z} (\vec{u} C_d) dz dr \approx \frac{\Delta t^n}{\Delta z_j} \left(F_{i,j+1/2}^{n-1} - F_{i,j-1/2}^{n-1} \right), \quad (3.86)$$

where

$$F_{i,j-\frac{1}{2}}^{n-1} = \vec{u}_{i,W} C_{d,i,W}^{n-1} + \frac{1}{2} |\vec{u}_{i,W}| \left(1 - \frac{\vec{u}_{i,W} \Delta t^n}{\Delta z_j} \right) \delta_{i,j-\frac{1}{2}}^{n-1}, \quad (3.87)$$

and W is the index of the upwind cell,

$$W = \begin{cases} j-1 & \vec{u} > 0 \\ j & \vec{u} < 0 \end{cases}, \quad (3.88)$$

and

$$\delta_{i,j-\frac{1}{2}}^{n-1} = \Gamma\left(\theta_{i,j-\frac{1}{2}}^{n-1}\right) \Delta C_{d,i,j-\frac{1}{2}}^{n-1}, \quad (3.89)$$

where

$$\Delta C_{d,i,j-\frac{1}{2}}^{n-1} = C_{d,i,j}^{n-1} - C_{d,i,j-1}^{n-1}, \quad (3.90)$$

$$\theta_{i,j-\frac{1}{2}}^{n-1} = \frac{\Delta C_{d,i,J-\frac{1}{2}}^{n-1}}{\Delta C_{d,i,j-\frac{1}{2}}^{n-1}}, \quad (3.91)$$

and J represents the upwind interface

$$J = \begin{cases} i-1 & \vec{u} > 0 \\ i+1 & \vec{u} < 0 \end{cases}. \quad (3.92)$$

The use of Eqs. (3.86) - (3.92) allows for a number of commonly used methods, see Table 3.4, to be implemented depending on the definition of $\Gamma(\theta)$.

Table 3.4: $\Gamma(\theta)$ definitions for a variety of methods. The definition for the minmod function is given in Eq. (3.93). Reproduced from [56].

Method	$\Gamma(\theta)$
Upwind	0
Lax-Wendroff	1
Beam-Warming	θ
Fromm	$\frac{1}{2}(1 + \theta)$
minmod	$\text{minmod}(1, \theta)$
<i>superbee</i>	$\max(0, \min(1, 2\theta), \min(2, \theta))$
MC	$\max(0, \min((1 + \theta)/2, 2, 2\theta))$
van Leer	$\frac{\theta + \theta }{1 + \theta }$

$$\text{minmod}(a, b) = \begin{cases} a & \text{if } |a| < |b| \text{ and } |ab| > 0 \\ b & \text{if } |b| < |a| \text{ and } |ab| > 0 \\ 0 & \text{if } |ab| \leq 0 \end{cases} \quad (3.93)$$

Initially, the upwind method was investigated. Unfortunately, the diffusive properties of the scheme led to a dramatic flattening of ‘pulses’ except with the use of prohibitively small time steps. Additionally, the upwind method is only a first-order approximation.

The Lax-Wendroff method, a second-order approximation, was also investigated. While lacking the unattractive diffusive properties of the upwind method,

the Lax-Wendroff method is prone to ringing near discontinuities [56], such as those that may occur at the boundary between the recirculation and core loops. This ringing can produce negative, non-physical precursor concentrations, which can in turn produce negative, non-physical scalar fluxes.

The minmod, *superbee*, MC, and van Leer approaches of Table 3.4 fall into a family of high-resolution limiters [56]. In general, these methods toggle between the aforementioned methods where appropriate. Where the solution is smooth, a second-order method such as Lax-Wendroff is used, and where the solution is characterized by large gradients, a method that introduces some numerical diffusion, such as the upwind method, is used. This permits second-order accuracy and avoids undue numerical diffusion where possible while avoiding non-physical ringing.

The *superbee* method, chosen for its ability to preserve pulse height, is used in this work. Substituting the approximation to the advection term into Eq. (3.84) yields

$$(C_{d,ij}^n - C_{d,ij}^{n-1}) + \frac{\Delta t^n}{\Delta z_j} (F_{i,j+1/2}^{n-1} - F_{i,j-1/2}^{n-1}) = \Delta t^n (-\lambda_d C_{d,ij}^n + \overline{\beta \nu \Sigma_f} \phi_{ij}^n). \quad (3.94)$$

The discretized periodic boundary conditions are enforced when calculating DNP fluxes $F_{i,j\pm 1/2}^{n-1}$ close to the boundaries.

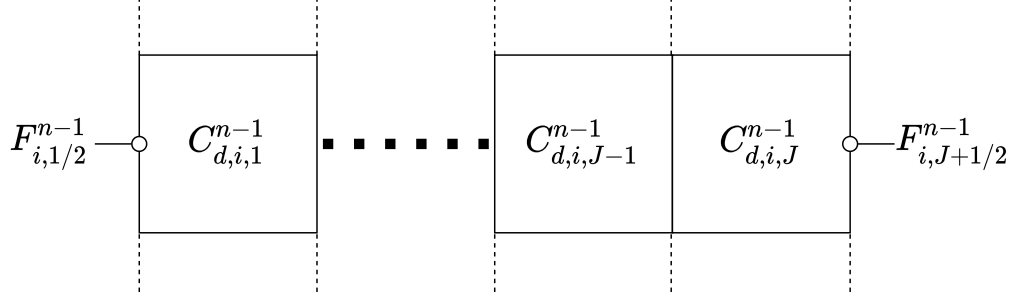


Figure 3.7: Boundary DNP fluxes for a row i . J is the total number of axial cells.

For the case when $\vec{u} > 0$, the boundary DNP flux $F_{i,1/2}^{n-1}$ depicted in Figure 3.7 is calculated with

$$\delta_{i,\frac{1}{2}}^{n-1} = \Gamma\left(\theta_{i,\frac{1}{2}}^{n-1}\right) (C_{d,i,j}^{n-1} - C_{d,i,J}^{n-1}), \quad (3.95a)$$

$$\theta_{i,\frac{1}{2}}^{n-1} = \frac{C_{d,i,J}^{n-1} - C_{d,i,J-1}^{n-1}}{C_{d,i,1}^{n-1} - C_{d,i,J}^{n-1}}. \quad (3.95b)$$

Similar expressions derived for $F_{i,J+1/2}^{n-1}$ are identical to those in Eq. (3.95). This is reassuring, as the periodic boundary condition implies the $(i, 1/2)$ and $(1, J + 1/2)$ surfaces are coincident, and therefore the DNP fluxes calculated on those surfaces should match.

Note that the advection term in Eq. (3.94) is modeled explicitly. This requires the selections for Δz_j and Δt^n to satisfy the CFL condition [56]. On a uniform mesh, this condition is

$$\left| \frac{\vec{u} \cdot \Delta t}{\Delta z} \right| \leq 1. \quad (3.96)$$

3.3.3 Energy balance discretization

The heat transfer equation is also discretized with a finite volume approach. Integrating Eq. (3.71e) over a cell with $r \in (r_{i-1/2}, r_{i+1/2})$, $z \in (z_{j-1/2}, z_{j+1/2})$ from $t \in (t^{n+1}, t^n)$ yields

$$\begin{aligned} \rho c_p (T^n - T^{n-1}) & - \frac{2\pi\Delta t^n}{V_{ij}} \int_i r \int_j \left(\frac{\kappa}{r} \frac{\partial}{\partial r} \left(r \frac{\partial}{\partial r} T^n \right) + \kappa \frac{\partial^2}{\partial z^2} T^n \right) dz dr \\ & + \frac{2\pi\Delta t^n}{V_{ij}} \int_i r \int_j \frac{\partial}{\partial z} (\vec{u} \rho c_p T^{n-1}) dz dr = \Delta t^n (Q_{m,ij}^n + Q_{f,ij}^n), \end{aligned} \quad (3.97)$$

where

$$T_{ij}^n = \frac{2\pi}{V_{ij}} \int_i r \int_j T^n dz dr. \quad (3.98)$$

The diffusion operator is approximated with the second-order, five-point stencil described by Morel et al. [57].

$$\begin{aligned} 2\pi \int_i r \int_j \left(\frac{\kappa}{r} \frac{\partial}{\partial r} \left(r \frac{\partial}{\partial r} T^n \right) + \kappa \frac{\partial^2}{\partial z^2} T^n \right) dz dr \\ \approx 2 \left(\frac{\Delta r_i}{\kappa_{ij}} + \frac{\Delta r_{i+1}}{\kappa_{i+1,j}} \right)^{-1} (T_{i+1,j}^n - T_{ij}^n) A^R \\ - 2 \left(\frac{\Delta r_i}{\kappa_{ij}} + \frac{\Delta r_{i-1}}{\kappa_{i-1,j}} \right)^{-1} (T_{ij}^n - T_{i-1,j}^n) A^L \\ + 2 \left(\frac{\Delta z_j}{\kappa_{ij}} + \frac{\Delta z_{j+1}}{\kappa_{i,j+1}} \right)^{-1} (T_{i,j+1}^n - T_{ij}^n) A^T \\ - 2 \left(\frac{\Delta z_j}{\kappa_{ij}} + \frac{\Delta z_{j-1}}{\kappa_{i,j-1}} \right)^{-1} (T_{ij}^n - T_{i,j-1}^n) A^B, \end{aligned} \quad (3.99)$$

where A^R , A^L , A^T , and A^B represent the surface areas of the right, left, top, and bottom faces of the cell at (i, j) .

The advection term is approximated with the same approach detailed in Section 3.3.2 for the DNP balance equation.

$$\frac{2\pi\Delta t^n}{V_{ij}} \int_i r \int_j \frac{\partial}{\partial z} (\vec{u}\rho c_p T^{n-1}) dz dr \approx \frac{\Delta t^n}{\Delta z_j} (F_{i,j+1/2}^{n-1} - F_{i,j-1/2}^{n-1}), \quad (3.100)$$

In the context of the heat transfer equation

$$F_{i,j-\frac{1}{2}}^n = (\vec{u}\rho c_p)_{i,W} T_{i,W}^n + \frac{1}{2} |(\vec{u}\rho c_p)_{i,W}| \left(1 - \frac{(\vec{u}\rho c_p)_{i,W} \Delta t}{\Delta x} \right) \delta_{i,j-\frac{1}{2}}^n \quad (3.101)$$

where

$$\delta_{i,j-\frac{1}{2}}^n = \Gamma \left(\theta_{i,j-\frac{1}{2}}^n \right) \Delta T_{i,j-\frac{1}{2}}^n, \quad (3.102)$$

$$\theta_{i,j-\frac{1}{2}}^n = \frac{\Delta T_{i,J-\frac{1}{2}}^n}{\Delta T_{i,j-\frac{1}{2}}^n}. \quad (3.103)$$

The superbee method is also used here. Substituting the approximations for the diffusion and advection terms into Eq. (3.97) yields Eq. (3.104)

$$\begin{aligned} & \rho c_p (T_{ij}^n - T_{ij}^{n-1}) - \frac{\Delta t^n}{V_{ij}} \left[\kappa_{i+1/2,j} \frac{T_{i+1,j}^n - T_{ij}^n}{\Delta r_{i+1/2}} A^R - \kappa_{i-1/2,j} \frac{T_{ij}^n - T_{i-1,j}^n}{\Delta r_{i-1/2}} A^L \right. \\ & \quad \left. + \kappa_{i,j+1/2} \frac{T_{i,j+1}^n - T_{ij}^n}{\Delta z_{j+1/2}} A^T - \kappa_{i,j-1/2} \frac{T_{ij}^n - T_{i,j-1}^n}{\Delta z_{j-1/2}} A^B \right] \\ & \quad + \frac{\Delta t^n}{\Delta z_j} (F_{i,j+1/2}^{n-1} - F_{i,j-1/2}^{n-1}) = \Delta t^n (Q_{m,ij}^n + Q_{f,ij}^n), \end{aligned} \quad (3.104)$$

where

$$\kappa_{i+1/2,j} = \left[\left(\frac{\Delta r_i}{\kappa_{ij}} + \frac{\Delta r_{i+1}}{\kappa_{i+1,j}} \right) \frac{1}{\Delta r_i + \Delta r_{i+1}} \right]^{-1}, \quad (3.105)$$

$$\Delta r_{i+1/2} = \frac{1}{2} (\Delta r_i + \Delta r_{i+1}). \quad (3.106)$$

The discretized Dirichlet and reflecting boundary conditions for $\vec{u} > 0$ are implemented by enforcing

$$T_f^n = \begin{cases} T_{\text{wall}} & \text{for } r_F = R, \\ T_{\text{inlet}} & \text{for } z_F = 0, \\ T_{\text{cell}}^n & \text{for } r_F = 0, \\ T_{\text{cell}}^n & \text{for } z_F = Z, \end{cases} \quad (3.107)$$

and using data (κ and Δr or Δz) defined in the boundary-adjacent cell. T_f^n is the temperature at a cell face which falls on the problem boundary and T_{cell}^n is the temperature in the cell to which that face belongs.

These conditions are demonstrated by evaluating Eq. (3.107) for the cell at (I, J) , depicted in Figure 3.8, which has Dirichlet (at the right face) and reflecting (at the top face) boundaries.

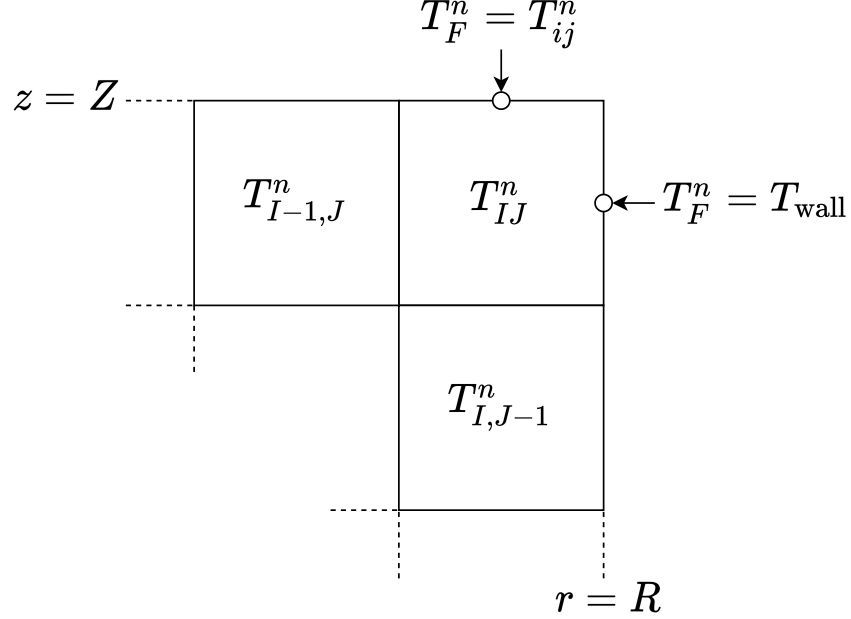


Figure 3.8: Implementation of discretized boundary conditions for the cell at (I, J) when $\vec{u} > 0$.

$$\begin{aligned}
 \rho c_p (T_{IJ}^n - T_{IJ}^{n-1}) - \frac{\Delta t^n}{V_{IJ}} & \left[\kappa_{IJ} \frac{T_{\text{wall}} - T_{ij}^n}{\Delta r_I} A^R \right. \\
 & - \kappa_{i-1/2,j} \frac{T_{IJ}^n - T_{I-1,J}^n}{\Delta r_{I-1/2}} A^L + \kappa_{I,J+1/2} \frac{T_{IJ}^n - T_{I,J-1}^n}{\Delta z_{J-1/2}} A^B \left. \right] \\
 & + \frac{\Delta t^n}{\Delta z_J} (F_{I,J+1/2}^{n-1} - F_{I,J-1/2}^{n-1}) = \Delta t^n (Q_{m,IJ}^n + Q_{f,IJ}^n), \quad (3.108)
 \end{aligned}$$

Note that Eq. (3.108) lacks an A^T term. This is a result of substituting $T_f^n = T_{I,J+1/2}^n = T_{IJ}^n$ in accordance with Eq. (3.107). Doing so eliminates the A^T term

entirely.

$$\kappa_{IJ} \frac{T_{I,J+1/2}^n - T_{ij}^n}{\Delta z_J} A^T = \kappa_{IJ} \frac{T_{ij}^n - T_{ij}^n}{\Delta z_J} A^T = 0.$$

Additional boundary considerations are necessary for calculating the energy fluxes $F_{i,j\pm 1/2}^n$. As the heat transfer equation does not have a periodic boundary condition, the approach here differs from the boundary treatment described for the DNP fluxes in Section 3.3.2. Near boundaries, the energy flux calculations use temperatures beyond the problem boundary, in so-called ghost cells. Temperatures in ghost cells before the inlet are assumed to be identical to the inlet temperature, and temperatures in ghost cells after the outlet are assumed to be identical to the outlet temperature. This scheme is depicted in Figure 3.9.

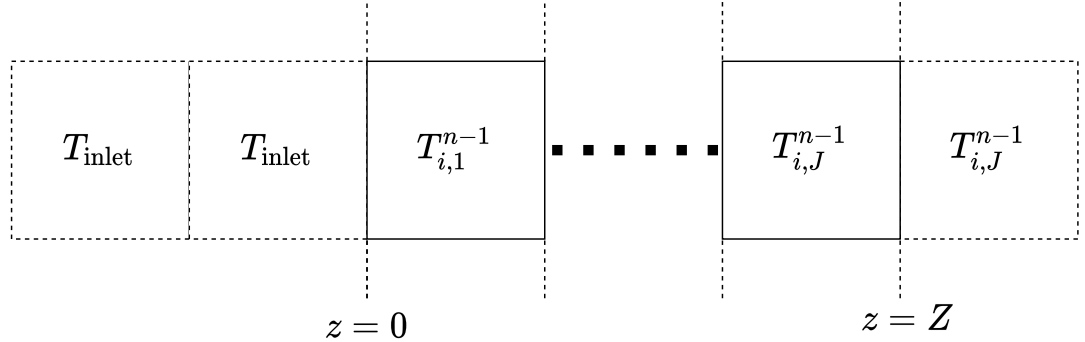


Figure 3.9: Ghost cell definitions for energy flux calculations near problem boundaries.

Finally, note the explicit approximation for the energy fluxes in Eq. (3.104). This introduces another CFL condition for stability.

$$\left| \frac{\vec{u} \cdot \rho c_p \Delta t}{\Delta z} \right| \leq 1. \quad (3.109)$$

3.3.4 Linear system

By evaluating Eqs. (3.80), (3.81), (3.94), and (3.104) across the spatial mesh, a linear system is constructed to solve for estimates of the in-core fluxes, DNP concentrations, and temperature in each cell at time t^n . Details of the unknowns in the linear system are presented in Table 3.5.

Table 3.5: Breakdown of unknowns in effective low-order transport solve. N and M are the number of axial and radial cells and N_D is the number of delayed neutron precursor groups.

Category	Number of unknowns
Scalar fluxes	$3NM + N + M$
DNP concentrations	$N_D NM$
Temperatures	NM
Total	$(4 + N_D) NM + N + M$

Note that the size of the system is no longer dependent on the number of neutron energy groups.

The DNP concentrations in the recirculation loop are not included in Table 3.5, as they are computed with a separate solve. By assuming neutron fluxes in the recirculation loop to be negligible, coupling to the QD and heat transfer equations is eliminated.

$$\frac{\partial}{\partial t} C_d + \frac{\partial}{\partial z} (\vec{u} C_d) = -\lambda_d C_d, \quad d = 1, \dots, N_d, \quad (3.110)$$

A separate linear system is formed by evaluating a discretized version of Eq. (3.110) in each cell of the recirculation loop. The linear system, as it depends only upon the DNP concentrations of the recirculation system, is of size $(N_{\text{recirc}}M_{\text{recirc}})^2$.

This two solve approach was implemented in an effort to reduce computational expense. Assuming Gaussian elimination [58], which has computational complexity of $O(p^3)$ where p is the total number of unknowns, is used to solve the described systems, the two solve approach would be cheaper as

$$(5NM + N + M)^3 + (N_{\text{recirc}}M_{\text{recirc}})^3 < (5NM + N_{\text{recirc}}M_{\text{recirc}} + N + M)^3.$$

The overall solution process requires an iterative solver as the nuclear data often has a non-linear dependence on temperature. In this work, simple fixed-point iteration (FPI) is used. The fixed-point iteration solve process for known multigroup fluxes, boundary factors, and Eddington factors is detailed in Algorithm 3.1.

Algorithm 3.1: Fixed-point iteration for ELOT problem

Result: Solutions for ϕ^n , C_d^n , and T^n at $t^n = t^1, \dots, t^N$.

```

1 for  $n = 1 : N$  do
2   Initialize  $\phi_0^n$ ,  $C_0^n$ , and  $T_0^n$ 
3   while  $|1 - \phi_k^n / \phi_{k-1}^n| > \epsilon_\phi$  or  $|1 - T_k^n / T_{k-1}^n| > \epsilon_T$  do
4      $k = k + 1$ 
5     Evaluate nuclear data  $\Sigma_k$  at  $T_{k-1}^n$ 
6     Solve for  $\phi_k^n$ ,  $C_k^n$ , and  $T_k^n$  using  $\Sigma_k$ 
7   end
8 end
```

For the general case, the multigroup fluxes, boundary factors, and Eddington

factors are not so simply known, and solutions at the MGHOT and MGLOQD levels are needed to define these parameters. The precise details of the multilevel algorithm are provided in Section 3.5.

3.4 Steady state formulation

A steady state capability utilizing k -eigenvalue formulations of the MGHOT, MGLOQD, and ELOT levels was also developed and implemented. The steady-state MGHOT system is shown in Eq. (3.111).

$$\begin{aligned} \frac{\mu}{r} \frac{\partial}{\partial r} (r \psi_g) + \xi \frac{\partial}{\partial z} \psi_g - \frac{1}{r} \frac{\partial}{\partial \omega} (\eta \psi_g) + \Sigma_{t,g} \psi_g \\ = \frac{1}{\int_{\hat{\Omega}} d\hat{\Omega}} \left[\left(\bar{\Sigma}_{s,g} + \frac{\chi_g^p}{k} \overline{(1-\beta) \nu \Sigma_f} \right) \phi + \sum_{d=1}^{N_d} \chi_g^d \lambda_d C_d \right], \quad (3.111) \end{aligned}$$

where $g = 1, \dots, G$. The steady-state MGLOQD system is shown in Eq. (3.112).

$$\frac{1}{r} \frac{\partial}{\partial r} (r J_{r,g}) + \frac{\partial}{\partial z} J_{z,g} + \Sigma_{t,g} \phi_g = Q_g, \quad (3.112a)$$

$$\frac{1}{h_{g,ij}} \frac{\partial}{\partial r} (h_{g,ij} E_{rr,g} \phi_g) + \frac{\partial}{\partial z} (E_{rz,g} \phi_g) + \Sigma_{t,g} J_{r,g} = 0. \quad (3.112b)$$

$$\frac{1}{r} \frac{\partial}{\partial r} (r E_{rz,g} \phi_g) + \frac{\partial}{\partial z} (E_{zz,g} \phi_g) + \Sigma_{t,g} J_{z,g} = 0, \quad (3.112c)$$

where $g = 1, \dots, G$, and

$$Q_g = \sum_{g'=1}^g \Sigma_{s,g' \rightarrow g} \phi_{g'} + \left(\frac{\sum_{g'=g+1}^G \Sigma_{s,g' \rightarrow g} \phi_{g'}}{\sum_{g'=g+1}^G \phi_{g'}} + \frac{\chi_g^p}{k} \frac{(1-\beta) \nu \Sigma_f}{(1-\beta) \nu \Sigma_f} \right) \phi + \sum_{d=1}^{N_d} \chi_g^d \lambda_d C_d. \quad (3.113)$$

The steady-state ELOT system is shown in Eq. (3.114).

$$\frac{1}{r} \frac{\partial}{\partial r} (r J_r) + \frac{\partial}{\partial z} J_z + \bar{\Sigma}_a \phi = \frac{(1-\beta) \nu \Sigma_f}{k} \phi + \sum_{d=1}^{N_d} \lambda_d C_d, \quad (3.114a)$$

$$\frac{1}{h_i} \frac{\partial}{\partial r} (h_i \bar{E}_{rr} \phi) + \frac{\partial}{\partial z} (\bar{E}_{rz} \phi) + \hat{\Sigma}_{tr} J_r + \hat{\zeta} \phi = 0, \quad (3.114b)$$

$$\frac{1}{r} \frac{\partial}{\partial r} (r \bar{E}_{rz} \phi) + \frac{\partial}{\partial z} (\bar{E}_{zz} \phi) + \tilde{\Sigma}_{tr} J_z + \tilde{\zeta} \phi = 0, \quad (3.114c)$$

$$\frac{\partial}{\partial z} (\vec{u} C_d) = -\lambda_d C_d + \frac{\beta \nu \Sigma_f}{k} \phi, \quad d = 1, \dots, N_d, \quad (3.114d)$$

$$\frac{\kappa}{r} \frac{\partial}{\partial r} \left(r \frac{\partial}{\partial r} T \right) - \kappa \frac{\partial^2}{\partial z^2} T + \frac{\partial}{\partial z} (\vec{u} \rho c_p T) = Q_\gamma + Q_f, \quad (3.114e)$$

where

$$\hat{\zeta} = \frac{\sum_{g=1}^G [\Sigma_{t,g} - \hat{\Sigma}_{tr}] J_{r,g}}{\sum_{g=1}^G \phi_g}, \quad (3.115a)$$

$$\tilde{\zeta} = \frac{\sum_{g=1}^G [\Sigma_{t,g} - \tilde{\Sigma}_{tr}] J_{z,g}}{\sum_{g=1}^G \phi_g}. \quad (3.115b)$$

The boundary conditions, and angular and spatial discretizations at each level are identical to those used in the transient systems. The eigenvalue is determined using power iteration at the ELOT level as detailed in Algorithm 2.

Algorithm 3.2: Power iteration for steady state ELOT problem

Result: Steady state solutions for ϕ , C_d , and T

```

1 j = 0
2 Initialize eigenvalue  $k_0$ , temperature  $T_0$ , and fission source  $F_0$ 
3 while  $\|1 - \phi_j/\phi_{j-1}\| > \epsilon_\phi$  or  $\|1 - T_j/T_{j-1}\| > \epsilon_T$  or  $\|1 - k_j/k_{j-1}\| > \epsilon_k$  do
4    $j = j + 1$ 
5   Evaluate nuclear data  $\Sigma_j$  at  $T_{j-1}$ 
6   Solve for  $\phi_k$ ,  $C_k$ , and  $T_k$  using  $\Sigma_j$  and  $k_{j-1}$ 
7    $k_j = k_{j-1} \frac{F_j}{F_{j-1}}$ 
8 end

```

3.5 Multilevel algorithms

A generalized multilevel algorithm for a transient solve is presented in Algorithm 3, where

$$r_{\phi,1} = \|1 - \phi_k^n / \phi_{k-1}^n\|, \quad (3.116a)$$

$$r_{\phi,2} = \|1 - \phi_{k,l}^n / \phi_{k,l-1}^n\|, \quad (3.116b)$$

$$r_{\phi,3} = \|1 - \phi_{k,l,m}^n / \phi_{k,l,m-1}^n\|, \quad (3.116c)$$

$$r_{T,1} = \|1 - T_k^n / T_{k-1}^n\|, \quad (3.116d)$$

$$r_{T,2} = \|1 - T_{k,l}^n / T_{k,l-1}^n\|, \quad (3.116e)$$

$$r_{T,3} = \|1 - T_{k,l,m}^n / T_{k,l,m-1}^n\|, \quad (3.116f)$$

are the flux and temperature residuals at the MGHOT (1), MGLOQD (2), and ELOT (3) levels and the convergence criteria are

$$\epsilon_\phi(r_\phi; \tau_\phi, \epsilon_\phi^{\text{abs}}) = \max(r_\phi \tau_\phi, \epsilon_\phi^{\text{abs}}), \quad (3.117\text{a})$$

$$\epsilon_T(r_T; \tau_T, \epsilon_T^{\text{abs}}) = \max(r_T \tau_T, \epsilon_T^{\text{abs}}). \quad (3.117\text{b})$$

The use of parameterized functions for the convergence criteria on inner loops allows for the iterative performance to be optimized through specification of the balance factors τ . This residual balance approach is described by Senecal and Ji [59].

Eq. (3.117) returns coarser convergence criteria when the solution is far from convergence, and, as the residuals decrease, will eventually return the absolute convergence criteria. The intention is to avoid unnecessary refinement of the solution at inner levels when the solutions at outer levels are still evolving.

The balance factors τ range from 0 to 1. Regardless of τ , one iteration is performed at each inner level, with additional iterations encouraged by smaller values of τ . For example, if $\tau_{\phi,3} = \tau_{T,3} = 10^{-4}$, iterations will continue on the ELOT level until r_3 is four orders of magnitude smaller than r_2 . If $\tau_{\phi,3} = \tau_{T,3} = 1$, any convergence in the ELOT level beyond that in the MGLOQD level ($r_3 < r_2$) will terminate ELOT iterations and computations will move out to the MGLOQD level.

Interrupt actions are defined on Lines 22 and 30; if the ratio of the current and previous residuals exceeds θ , the solve is reset to the nearest outer level. This

condition can occur when data calculated at an outer level significantly alters a solution at an inner level, a correction which may be best considered with immediacy in the outer level. The selection of θ defines which corrections are significant. For $\theta = 1$, for example, any increase in residuals on the ELOT or MGLOQD levels will trigger an interrupt.

The steady-state solution algorithm, which closely resembles the transient algorithm, is detailed in Algorithm 4. The major difference between the two, besides the lack of a loop over time in the steady-state algorithm, is on Line 20 of Algorithm 4. This line describes the update to the eigenvalue using the power iteration approach, where F is the fission source in the ELOT problem. Convergence of the eigenvalue is measured with

$$r_{k_{\text{eff}}} = |1 - k_{\text{eff}}^{k,l,m} / k_{\text{eff}}^{k,l,m-1}|, \quad (3.118a)$$

$$\epsilon_{k_{\text{eff}}} (r; \tau_{k_{\text{eff}}}, \epsilon_{k_{\text{eff}}}^{\text{abs}}) = \max (r_{k_{\text{eff}}}, \tau_{k_{\text{eff}}}, \epsilon_{k_{\text{eff}}}^{\text{abs}}). \quad (3.118b)$$

Note that for $\theta = \infty$ and $\tau = 0$, both of the algorithms reduce to fixed-point iteration.

3.6 Implementation details

The methods described in Sections 3.1, 3.2, 3.3, 3.4, and 3.5 were implemented in the open-source software QuasiMolto¹. QuasiMolto is written in C++, built with

¹<https://github.com/aaronjamesreynolds/QuasiMolto>

the CMake compiler, and features continuous integration testing through Travis CI. The Eigen C++ library [60] is used extensively throughout QuasiMolto.

For the purposes of developing a computational tool, Eigen offers a variety of assets such as built-in solvers, sparse data types, and convenient matrix manipulations. The rapid development performed in this work was greatly served by this broad utility. However, while Eigen does feature some parallelism, it is not of the same level offered by high-performance computing libraries such as PETSc or hypre [61, 62]. Additionally, parallelizing the procedure by which linear systems are built would require a non-trivial development effort.

For the transient presented in Section 4.3, which features a single material, the capabilities of Eigen were sufficient. Transient simulations of the MSRE, for example, would require a finer mesh to resolve geometric features, resulting in linear systems of a size better served by the scalability of the high-performance libraries mentioned.

Algorithm 3.3: Residual-balanced fixed-point iteration for transient solve of multilevel problem.

Result: Solutions for ϕ^n , $C^{d,n}$, and T^n at $t^n = t^1, \dots, t^N$.

```

1  for  $n = 1 : N$  do
2    Initialize iterates of  $\phi^n$ ,  $C^{d,n}$ , and  $T^n$ 
3    while  $r_{\phi,1} > \epsilon_{\phi}^{abs}$  or  $r_{T,1} > \epsilon_T^{abs}$  do
4      Multigroup High-Order Transport
5       $k = k + 1$ 
6      Solve for  $\psi_k^{g,n}$  using  $\phi_{k-1}^n$ ,  $C_{k-1}^{d,n}$ ,  $T_{k-1}^n$ , and  $\tilde{\Sigma}_{k-1}^n$ 
7      Calculate group Eddington and boundary factors  $E_k^{g,n}$  and  $C_k^{g,n}$  using  $\psi_k^n$ 
8
9      while  $r_{\phi,2} > \epsilon_{\phi,2} (r_{\phi,1}; \tau_{\phi,2}, \epsilon_{\phi}^{abs})$  or  $r_{T,2} > \epsilon_{T,2} (r_{T,1}; \tau_{T,2}, \epsilon_T^{abs})$  do
10        Multigroup Low-Order Quasi-Diffusion
11         $l = l + 1$ 
12        Solve for  $\phi_{k,l}^{g,n}$  using  $E_k^{g,n}$ ,  $C_k^{g,n}$ ,  $\phi_{k,l-1}^n$ ,  $C_{k,l-1}^{d,n}$ ,  $T_{k,l-1}^n$ , and  $\tilde{\Sigma}_{k,l-1}^n$ 
13        Calculate collapsed Eddington and boundary factors  $\tilde{E}_{k,l}^n$  and  $\tilde{C}_{k,l}^n$  using
14           $E_k^{g,n}$ ,  $C_k^{g,n}$ , and  $\phi_k^{g,n}$ 
15        while  $r_{\phi,3} > \epsilon_{\phi,3} (r_{\phi,2}; \tau_{\phi,3}, \epsilon_{\phi}^{abs})$  or  $r_{T,3} > \epsilon_{T,3} (r_{T,2}; \tau_{T,3}, \epsilon_T^{abs})$  do
16          Effective Low-Order Transport
17           $m = m + 1$ 
18          Calculate collapsed nuclear data  $\tilde{\Sigma}_{k,l,m}^n$  using  $\phi_{k,l}^{g,n}$  and  $T_{k,l,m-1}^{g,n}$ 
19          Solve for  $\phi_{k,l,m}^n$ ,  $C_{k,l,m}^{d,n}$ , and  $T_{k,l,m}^n$  using  $\tilde{E}_{k,l}^n$ ,  $\tilde{C}_{k,l}^n$ , and  $\tilde{\Sigma}_{k,l,m}^n$ 
20
21          if  $r_{\phi,3}/r_{\phi,3}^{prev} > \theta$  or  $r_{T,3}/r_{T,3}^{prev} > \theta$  then
22            | Break to MGLOQD
23
24        end
25         $m = 0$ 
26        Update MGQD iterates:
27         $\phi_{k,l}^n = \phi_{k,l,m}^n$ ,  $C_{k,l}^{d,n} = C_{k,l,m}^{d,n}$ ,  $T_{k,l}^n = T_{k,l,m}^n$ ,  $\tilde{\Sigma}_{k,l}^n = \tilde{\Sigma}_{k,l,m}^n$ 
28
29        if  $r_{\phi,2}/r_{\phi,2}^{prev} > \theta$  or  $r_{T,2}/r_{T,2}^{prev} > \theta$  then
30          | Break to MGHOT
31
32      end
33       $l = 0$ 
34      Update MGT iterates:
35       $\phi_k^n = \phi_{k,l,m}^n$ ,  $C_k^{d,n} = C_{k,l,m}^{d,n}$ ,  $T_k^n = T_{k,l,m}^n$ ,  $\tilde{\Sigma}_k^n = \tilde{\Sigma}_{k,l,m}^n$ 
36    end
37     $k = 0$ 
38 end

```

Algorithm 3.4: Residual-balanced fixed-point iteration for steady-state solve of multilevel problem.

```

Result: Steady-state solutions for  $\phi$ ,  $C^d$ , and  $T$ 
1 for  $n = 1 : N$  do
2   Initialize iterates of  $\phi$ ,  $C^d$ , and  $T$ 
3   while  $r_{\phi,1} > \epsilon_{\phi}^{abs}$  or  $r_{T,1} > \epsilon_T^{abs}$  or  $r_{k_{eff}} > \epsilon_k^{abs}$  do
4     Multigroup High-Order Transport
5      $k = k + 1$ 
6     Solve for  $\psi_k^g$  using  $\phi_{k-1}$ ,  $C_{k-1}^d$ ,  $T_{k-1}$ ,  $k_{eff}^{k-1}$  and  $\tilde{\Sigma}_{k-1}$ 
7     Calculate group Eddington and boundary factors  $E_k^g$  and  $C_k^g$  using  $\psi_k$ 
8
9     while  $r_{\phi,2} > \epsilon_{\phi,2}(r_{\phi,1}; \tau_{\phi,2}, \epsilon_{\phi}^{abs})$  or  $r_{T,2} > \epsilon_T(r_{T,1}; \tau_{T,2}, \epsilon_T^{abs})$  do
10    Multigroup Low-Order Quasi-Diffusion
11     $l = l + 1$ 
12    Solve for  $\phi_{k,l}^g$  using  $E_k^g$ ,  $C_k^g$ ,  $\phi_{k,l-1}$ ,  $C_{k,l-1}^d$ ,  $T_{k,l-1}$ ,  $k_{eff}^{k,l-1}$ , and  $\tilde{\Sigma}_{k,l-1}$ 
13    Calculate collapsed Eddington and boundary factors  $\tilde{E}_{k,l}$  and  $\tilde{C}_{k,l}$  using
14       $E_k^g$ ,  $C_k^g$ , and  $\phi_k^g$ 
15    while  $r_{\phi,3} > \epsilon_{\phi}(r_{\phi,2}; \tau_{\phi,3}, \epsilon_{\phi}^{abs})$  or  $r_{T,3} > \epsilon_T(r_{T,2}; \tau_{T,3}, \epsilon_T^{abs})$  or
16       $r_{k_{eff}} > \epsilon_{k_{eff}}(r_{\phi,2}; \tau_{k_{eff}}, \epsilon_{k_{eff}}^{abs})$  do
17      Effective Low-Order Transport
18       $m = m + 1$ 
19      Calculate collapsed nuclear data  $\tilde{\Sigma}_{k,l,m}$  using  $\phi_{k,l}^g$  and  $T_{k,l,m-1}^g$ 
20      Solve for  $\phi_{k,l,m}$ ,  $C_{k,l,m}^d$ , and  $T_{k,l,m}^n$  using  $\tilde{E}_{k,l}$ ,  $\tilde{C}_{k,l}$ ,  $k_{eff}^{k,l,m-1}$ , and  $\tilde{\Sigma}_{k,l,m}$ 
21       $k_{eff}^{k,l,m} = k_{eff}^{k,l,m-1} \frac{F_{k,l,m}}{F_{k,l,m-1}}$ 
22      if  $r_{\phi,3}/r_{\phi,3}^{prev} > \theta$  or  $r_{T,3}/r_{T,3}^{prev} > \theta$  then
23        | Break to MGLOQD
24
25    end
26     $m = 0$ 
27    Update MGQD iterates:
28     $\phi_{k,l} = \phi_{k,l,m}$ ,  $C_{k,l}^d = C_{k,l,m}^d$ ,  $T_{k,l} = T_{k,l,m}$ ,  $k_{eff}^{k,l} = k_{eff}^{k,l,m}$ ,  $\tilde{\Sigma}_{k,l} = \tilde{\Sigma}_{k,l,m}$ 
29
30    if  $r_{\phi,2}/r_{\phi,2}^{prev} > \theta$  or  $r_{T,2}/r_{T,2}^{prev} > \theta$  then
31      | Break to MGHOT
32
33    end
34     $l = 0$ 
35    Update MGT iterates:
36     $\phi_k = \phi_{k,l,m}$ ,  $C_k^d = C_{k,l,m}^d$ ,  $T_k = T_{k,l,m}$ ,  $k_{eff}^k = k_{eff}^{k,l,m}$ ,  $\tilde{\Sigma}_k = \tilde{\Sigma}_{k,l,m}$ 
37  end
38   $k = 0$ 
39 end

```

4 Results and Discussion

Results are presented in four sections. In Section 4.1, a verification using the method of manufactured solutions is presented. In Section 4.2, a study of the balance parameters used in the multilevel algorithms is shown. A transient calculation is demonstrated in Section 4.3, as well as a verification of the steady-state eigenvalue calculation. Steady-state calculations for an RZ model of the MSRE, with comparisons to reference values, are presented in Section 4.4, and are followed by calculations to examine the impact of capturing transport effects on the modeled problem.

The convergence criteria in these results, where applicable and unless otherwise stated, are detailed in Table 4.1.

Table 4.1: Convergence critieria.

$\epsilon_{\phi}^{\text{abs}}$	ϵ_T^{abs}	$\epsilon_{k_{\text{eff}}}^{\text{abs}}$
10^{-8}	10^{-8}	10^{-8}

4.1 Method of manufactured solutions verification

The implementations of the solvers described in Sections 3.1, 3.2, and 3.3 for the MGHOT, MGLOQD, and ELOT levels were each verified with the method of manufactured solutions (MMS) [63]. In MMS, an analytic solution is prescribed

for the dependent variable(s) of an equation and a source term is appended such that the prescribed solution satisfies the equation.

For example, consider the equation below, whose solution needs to be verified.

$$f(g(r, z, t)) = 0 \quad (4.1)$$

A solution is prescribed for $g(r, z, t) = g_{\text{MMS}}(r, z, t)$

$$f(g_{\text{MMS}}(r, z, t)) = Q_{\text{MMS}}(r, z, t), \quad (4.2)$$

and $Q_{\text{MMS}}(r, z, t)$ is determined by evaluating $f(g_{\text{MMS}}(r, z, t))$. The MMS source term $Q_{\text{MMS}}(r, z, t)$ is then discretized like any other and the solver should return a grid function approximating $g_{\text{MMS}}(r, z, t)$. The error in this approximation will be a function of the spatial mesh, time step, and the order of accuracy of the underlying discretizations. If the error decreases at the expected rate as the mesh is refined, it indicates that (1) the discretizations are valid to approximate the system in question and (2) the implementation of the discretizations is correct.

The error in the approximate solution is calculated by

$$\text{error}(t_n) = \vec{G}_n - \vec{g}_n, \quad (4.3)$$

where the vector \vec{G}_n contains the exact volume-averaged $g_{\text{MMS}}(r, z, t_n)$ in each cell and \vec{g}_n contains approximations for the volume-averaged $g_{\text{MMS}}(r, z, t_n)$ in each cell.

$$\vec{G}_n = \begin{bmatrix} G_{11}^n \\ \vdots \\ G_{NM}^n \end{bmatrix}, \quad (4.4a)$$

$$\vec{g}_n = \begin{bmatrix} g_{11}^n \\ \vdots \\ g_{NM}^n \end{bmatrix}, \quad (4.4b)$$

where

$$G_{ij}^n = \frac{2\pi}{V_{ij}} \int_i r \int_j g_{\text{MMS}}(r, z, t_n) dz dr. \quad (4.5)$$

4.1.1 Neutron transport

Isotropic The MGHOT solver is verified on a slightly modified, one-group formulation of Eq. (3.10).

$$\frac{1}{v} \frac{\partial}{\partial t} \psi + \frac{\mu}{r} \frac{\partial}{\partial r} (r \psi) + \xi \frac{\partial}{\partial z} \psi - \frac{1}{r} \frac{\partial}{\partial \omega} (\eta \psi) + \Sigma_t \psi = \frac{1}{4} \left(\Sigma_s + \nu \Sigma_f \right) \phi, \quad (4.6)$$

where

$$\phi = \int_{\Omega} \psi d\Omega. \quad (4.7)$$

Eq. (4.6) has no coupling to the DNP balance equations and, further, the nuclear data is assumed to be constant with respect to temperature. The ELOT level no longer provides ϕ and, instead, source iterations are used to determine the scattering and fission sources.

The prescribed solution is

$$\psi_{\text{MMS}} = \sin\left(\frac{\pi z}{Z}\right) (R^2 - r^2) e^{ct}, \quad (4.8a)$$

$$\phi_{\text{MMS}} = \int_{\hat{\Omega}} \psi_{\text{MMS}} d\hat{\Omega} = 4 \sin\left(\frac{\pi z}{Z}\right) (R^2 - r^2) e^{ct}. \quad (4.8b)$$

After evaluating Eq. (4.6) for $\psi = \psi_{\text{MMS}}$ and solving for Q_{MMS} , the verification equation can be formulated.

$$\begin{aligned} \frac{1}{v} \frac{\partial}{\partial t} \psi_{\text{MMS}} + \frac{\mu}{r} \frac{\partial}{\partial r} (r \psi_{\text{MMS}}) + \xi \frac{\partial}{\partial z} \psi_{\text{MMS}} - \frac{1}{r} \frac{\partial}{\partial \omega} (\eta \psi_{\text{MMS}}) \\ + \Sigma_t \psi_{\text{MMS}} = \left(\Sigma_s + \nu \Sigma_f \right) \psi_{\text{MMS}} + Q_{\text{MMS}}, \end{aligned} \quad (4.9)$$

where

$$Q_{\text{MMS}} = A \sin\left(\frac{\pi z}{Z}\right) (R^2 - r^2) - 2B \sin\left(\frac{\pi z}{Z}\right) r + D \cos\left(\frac{\pi z}{Z}\right) (R^2 - r^2), \quad (4.10)$$

and

$$A = e^{ct} \left[\frac{c}{v} + \Sigma_t - (\Sigma_s + \nu \Sigma_f) \right], \quad (4.11a)$$

$$B = e^{ct} \mu, \quad (4.11b)$$

$$D = e^{ct} \frac{\pi \xi}{Z}. \quad (4.11c)$$

Note that Eq. (4.8a) satisfies Eq. (3.7a), which describes the reflecting boundary condition at $r = 0$. For Eq. (3.7d), an incident angular flux of zero is assumed.

Solutions are computed on the uniform meshes described in Table 4.2 with the uniform nuclear data described in Table 4.3. Figures 4.1 and 4.2 show the results

Table 4.2: Meshes for isotropic MMS mesh refinement study, where $h_s = 0.1$ cm, and $h_t = 1E-4$ s. All simulations use $Z = 1.0$ cm, $R = 1.0$ cm, and $T = 1E-4$ s.

Δz	Δr	Δt
h_s	h_s	h_t
$h_s/2$	$h_s/2$	h_t
$h_s/4$	$h_s/4$	h_t
$h_s/8$	$h_s/8$	h_t
$h_s/16$	$h_s/16$	h_t
$h_s/32$	$h_s/32$	h_t

Table 4.3: Nuclear data used on the meshes in Table 4.2. c is the parameter that appears in Eq. (4.8a).

Σ_t	Σ_s	Σ_f	ν	v	c
1.0	0.5	0.5	2.0	1.0	1.0

of the isotropic convergence study for the scalar and angular fluxes.

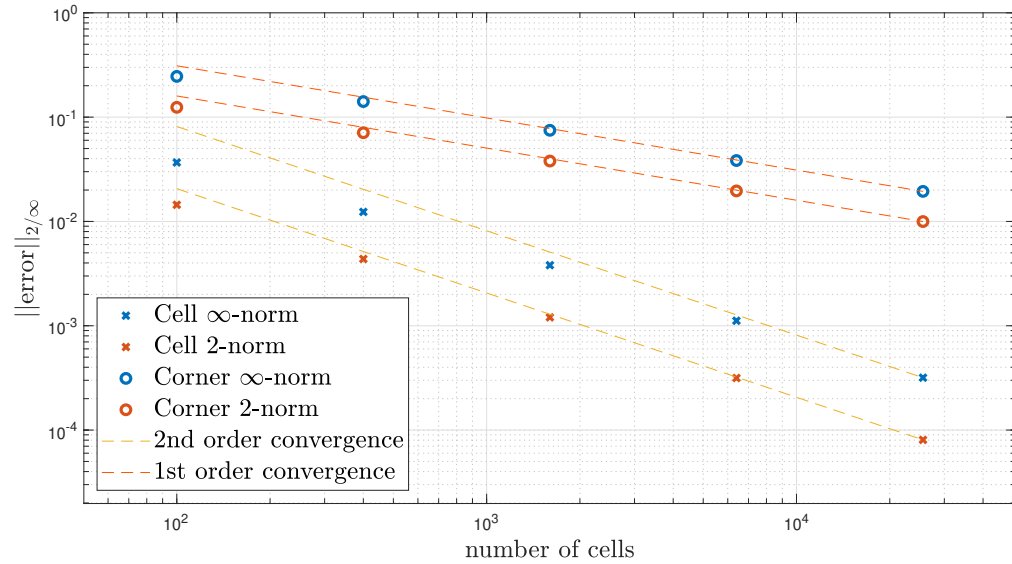


Figure 4.1: Simple corner balance convergence study for isotropic MMS problem.

Errors are measured from the scalar fluxes.

The cell scalar fluxes exhibit second-order convergence and the corner scalar fluxes exhibit first-order convergence, aligning with expectation. The cell fluxes are calculated with a simple arithmetic average of the corner values.

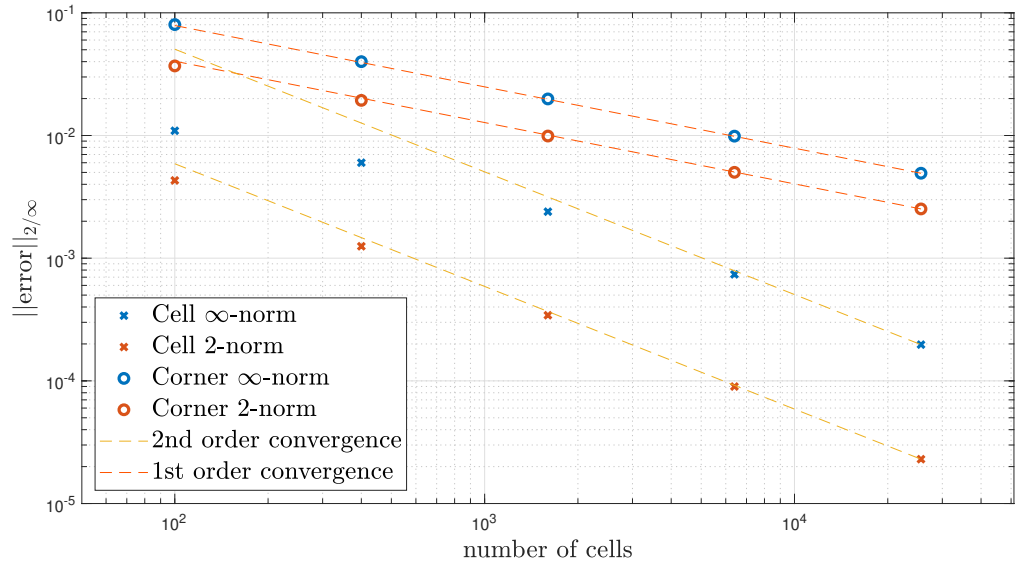


Figure 4.2: Simple corner balance convergence study for isotropic MMS problem.

Errors are measured from the angular fluxes with direction cosines $(\xi_p, \mu_{pq}) = (-0.971638, -0.167213)$.

The angular fluxes at a single angle are examined, and much of the same is observed; second- and first-order convergence for the cell and corner quantities, respectively.

Note the use of a constant time step in Table 4.2, and recall the manufactured solution has an exponential time dependence. As the α -approximation described in Eq. (3.14) assumes the angular flux to have an exponential time dependence, the error contributed from the approximation to the time derivative is zero, and the anticipated convergence can be observed without refinement of the time step. This is an advantageous approach because the solutions on finer meshes are already computationally expensive for a single time step, and refined time steps would

require multiple solves.

Figure 4.1 and 4.2 indicate that the MGHOT discretizations are valid and implemented correctly.

Anisotropic An anisotropic manufactured solution was also considered. Here, the convergence rate is expected to decrease as the spatial mesh is refined. This should occur because the angular mesh is not refined in step with the spatial mesh; all solutions are computed using the S₁₂ quadrature set described in Section 3.1.2.

As the spatial mesh is refined, the associated errors should decrease as they did for the isotropic problem, but now the error contributed from the discretization of the angular derivative must be considered. This error will remain static as the spatial mesh is refined. Eventually, the angular error will dominate and the convergence rate should decrease, eventually to zero, as the magnitude of the angular discretization error will be far greater than any reduction in error from spatial refinement.

The anisotropic manufactured solution is

$$\psi_{MMS} = \sin\left(\frac{\pi z}{Z}\right) \left(1 - \cos\left(\frac{2\pi r}{R}\right)\right) e^{ct} \mu^2, \quad (4.12a)$$

$$\phi_{MMS} = \int_{\hat{\Omega}} \psi_{MMS} d\hat{\Omega} = \frac{4}{3} \sin\left(\frac{\pi z}{Z}\right) \left(1 - \cos\left(\frac{2\pi r}{R}\right)\right) e^{ct}, \quad (4.12b)$$

and analytic source term Q_{MMS} is

$$\begin{aligned} Q_{\text{MMS}} = & \sin\left(\frac{\pi z}{Z}\right) \left(1 - \cos\left(\frac{2\pi r}{R}\right) + \frac{2\pi r}{R} \sin\left(\frac{2\pi r}{R}\right)\right) \frac{A}{r} \\ & + \cos\left(\frac{\pi z}{Z}\right) \left(1 - \cos\left(\frac{2\pi r}{R}\right)\right) B \\ & + \sin\left(\frac{\pi z}{Z}\right) \left(1 - \cos\left(\frac{2\pi r}{R}\right)\right) \left(\frac{D}{r} + F\right), \end{aligned} \quad (4.13)$$

where

$$A = e^{ct} \mu^3, \quad (4.14a)$$

$$B = e^{ct} \frac{\pi \xi \mu^2}{Z}, \quad (4.14b)$$

$$D = -e^{ct} \mu (\sin(\gamma)^2 - 3\eta^2), \quad (4.14c)$$

$$F = e^{ct} \left[\mu^2 \left(\Sigma_t + \frac{c}{v} \right) - \frac{1}{3} (\Sigma_s + \nu \Sigma_f) \right]. \quad (4.14d)$$

Solutions were computed on the uniform meshes in Table 4.4 with the nuclear data in Table 4.4. Figure 4.3 shows results of the anisotropic convergence study

Table 4.4: Meshes for anisotropic MMS convergence study, where $h_s = 10$ cm, and $h_t = 1\text{E}-4$ s. All meshes use $Z = 100$ cm, $R = 100$ cm, and $T = 1\text{E}-4$ s.

Δz	Δr	Δt
h_s	h_s	h_t
$h_s/2$	$h_s/2$	h_t
$h_s/4$	$h_s/4$	h_t
$h_s/8$	$h_s/8$	h_t
$h_s/16$	$h_s/16$	h_t

for the cell scalar fluxes.

Table 4.5: Nuclear data used on the meshes in Table 4.4.

Σ_t	Σ_s	Σ_f	ν	v	c
1.0	0.01	0.01	2.0	1.0	1.0

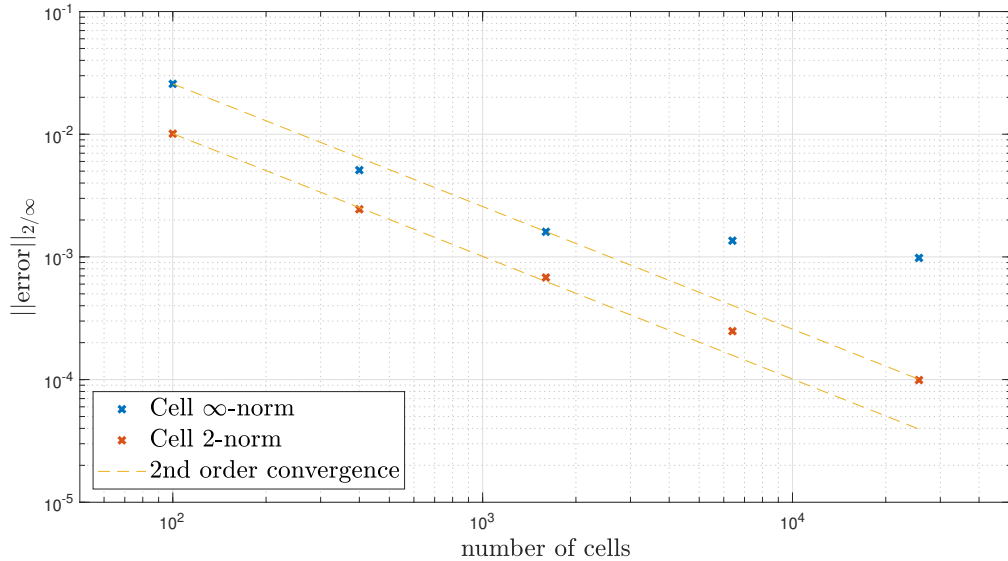


Figure 4.3: Simple corner balance convergence study for anisotropic MMS problem.
Errors are measured from the scalar fluxes.

As anticipated, the first few refinements show second-order convergence; these refinements fall into a regime where the spatial discretization error dominates. With further refinements, the convergence rates decrease, most notably in the ∞ -norm, as a regime is entered where the angular discretization error begins to dominate.

4.1.2 Quasi-diffusion

Similar to the previous section, the QD solver used in the MGLOQD and ELOT levels was verified on an independent, one-group formulation of Eq. (3.54).

$$\frac{1}{v} \frac{\partial}{\partial t} \phi + \frac{1}{r} \frac{\partial}{\partial r} (r J_r) + \frac{\partial}{\partial z} J_z + \Sigma_t \phi = \Sigma_s \phi + \nu \Sigma_f \phi, \quad (4.15a)$$

$$\frac{1}{v} \frac{\partial}{\partial t} J_r + \frac{1}{r^G} \frac{\partial}{\partial r} (r^G E_{rr} \phi) + \frac{\partial}{\partial z} (E_{rz} \phi) + \Sigma_t J_r = 0, \quad (4.15b)$$

$$\frac{1}{v} \frac{\partial}{\partial t} J_z + \frac{1}{r} \frac{\partial}{\partial r} (r E_{rz} \phi) + \frac{\partial}{\partial z} (E_{zz} \phi) + \Sigma_t J_z = 0, \quad (4.15c)$$

The prescribed solution for the angular flux was

$$\psi_{\text{MMS}} = (A\mu + B\xi + D)^2 \sin\left(\frac{\pi z}{Z}\right) \left(1 - \cos\left(\frac{2\pi r}{R}\right)\right) e^{Ct}. \quad (4.16)$$

From Eq. (4.16) the scalar flux, currents, and Eddington factors were determined.

$$\phi_{\text{MMS}} = \frac{4(A^2 + B^2 + 3D^2)}{3} \sin\left(\frac{\pi z}{Z}\right) \left(1 - \cos\left(\frac{2\pi r}{R}\right)\right) e^{Ct}, \quad (4.17a)$$

$$J_{z,\text{MMS}} = \frac{8BD}{3} \sin\left(\frac{\pi z}{Z}\right) \left(1 - \cos\left(\frac{2\pi r}{R}\right)\right) e^{Ct}, \quad (4.17b)$$

$$J_{r,\text{MMS}} = \frac{8AD}{3} \sin\left(\frac{\pi z}{Z}\right) \left(1 - \cos\left(\frac{2\pi r}{R}\right)\right) e^{Ct}. \quad (4.17c)$$

$$E_{zz,\text{MMS}} = \frac{A^2 + 3B^2 + 5D^2}{5(A^2 + B^2 + 3D^2)}, \quad (4.17d)$$

$$E_{rr,\text{MMS}} = \frac{3A^2 + B^2 + 5D^2}{5(A^2 + B^2 + 3D^2)}, \quad (4.17e)$$

$$E_{rz,\text{MMS}} = \frac{2AB}{5(A^2 + B^2 + 3D^2)}, \quad (4.17\text{f})$$

The coefficients A , B , C , and D are selected to analyze a number of different problem types, as detailed in Table 4.6.

Table 4.6: QD MMS coefficients.

Problem Type	A	B	C	D	$E_{rr,\text{MMS}}$	$E_{zz,\text{MMS}}$	$E_{rz,\text{MMS}}$
Diffusion physics	0	0	0	1	1/3	1/3	0
Transport physics	0	1	0	1	0.40	0.30	0
	1	0	0	1	0.30	0.40	0
	1	1	0	1	0.36	0.36	0.08
Time dependent	1	1	1	1	0.36	0.36	0.08

Substitution of the prescribed solution into Eq. (4.15) produces

$$\begin{aligned} \frac{1}{v} \frac{\partial}{\partial t} \phi_{\text{MMS}} + \frac{1}{r} \frac{\partial}{\partial r} (r J_{r,\text{MMS}}) + \frac{\partial}{\partial z} J_{z,\text{MMS}} + \Sigma_t \phi_{\text{MMS}} \\ = \Sigma_s \phi_{\text{MMS}} + \nu \Sigma_f \phi_{\text{MMS}} + Q_{\text{MMS},0}, \quad (4.18\text{a}) \end{aligned}$$

$$\begin{aligned} \frac{1}{v} \frac{\partial}{\partial t} J_{r,\text{MMS}} + \frac{1}{r^G} \frac{\partial}{\partial r} (r^G E_{rr,\text{MMS}} \phi_{\text{MMS}}) + \frac{\partial}{\partial z} (E_{rz,\text{MMS}} \phi_{\text{MMS}}) \\ + \Sigma_t J_{r,\text{MMS}} = Q_{\text{MMS},1\text{R}}, \quad (4.18\text{b}) \end{aligned}$$

$$\begin{aligned} \frac{1}{v} \frac{\partial}{\partial t} J_{z,\text{MMS}} + \frac{1}{r} \frac{\partial}{\partial r} (r E_{rz,\text{MMS}} \phi_{\text{MMS}}) + \frac{\partial}{\partial z} (E_{zz,\text{MMS}} \phi_{\text{MMS}}) \\ + \Sigma_t J_{z,\text{MMS}} = Q_{\text{MMS},1Z}, \quad (4.18c) \end{aligned}$$

where

$$\begin{aligned} Q_{\text{MMS},0} = e^{Ct} & \left[\frac{4(A^2 + B^2 + 3D^2)}{3} \left(\frac{C}{v} + \Sigma_a \right) \sin \left(\frac{\pi z}{Z} \right) \left(1 - \cos \left(\frac{2\pi r}{R} \right) \right) \right. \\ & + \frac{8AD}{3r} \sin \left(\frac{\pi z}{Z} \right) \left(1 - \cos \left(\frac{2\pi r}{R} \right) + \frac{2\pi r}{R} \sin \left(\frac{2\pi r}{R} \right) \right) \\ & \left. + \frac{8BD\pi}{3Z} \cos \left(\frac{\pi z}{Z} \right) \left(1 - \cos \left(\frac{2\pi r}{R} \right) \right) \right], \quad (4.19a) \end{aligned}$$

$$\begin{aligned} Q_{\text{MMS},1R} = e^{Ct} & \left[\frac{8AD}{3} \left(\frac{C}{v} + \Sigma_t \right) \sin \left(\frac{\pi z}{Z} \right) \left(1 - \cos \left(\frac{2\pi r}{R} \right) \right) \right. \\ & + \frac{4(A^2 + B^2 + 3D^2)}{3} \left(\frac{E_{rz}\pi}{Z} \cos \left(\frac{\pi z}{Z} \right) \left(1 - \cos \left(\frac{2\pi r}{R} \right) \right) \right. \\ & \left. \left. + E_{rr} \sin \left(\frac{\pi z}{Z} \right) \left(\frac{G}{r} \left(1 - \cos \left(\frac{2\pi r}{R} \right) \right) + \frac{2\pi}{R} \sin \left(\frac{2\pi r}{R} \right) \right) \right) \right], \quad (4.19b) \end{aligned}$$

$$\begin{aligned} Q_{\text{MMS},1Z} = e^{Ct} & \left[\frac{8BD}{3} \left(\frac{C}{v} + \Sigma_t \right) \sin \left(\frac{\pi z}{Z} \right) \left(1 - \cos \left(\frac{2\pi r}{R} \right) \right) \right. \\ & + \frac{4(A^2 + B^2 + 3D^2)}{3} \left(\frac{E_{zz}\pi}{Z} \cos \left(\frac{\pi z}{Z} \right) \left(1 - \cos \left(\frac{2\pi r}{R} \right) \right) \right. \\ & \left. \left. + \frac{E_{rz}}{r} \sin \left(\frac{\pi z}{Z} \right) \left(1 - \cos \left(\frac{2\pi r}{R} \right) + \frac{2\pi r}{R} \sin \left(\frac{2\pi r}{R} \right) \right) \right) \right]. \quad (4.19c) \end{aligned}$$

Solutions were computed on the meshes in Tables 4.7 and 4.8, with the nuclear data in Table 4.9. Table 4.8, which describes the mesh parameters for time-dependent

problems, shows a squared refinement in Δt for each linear refinement in space, as the approximations to the time and space derivatives are first- and second-order accurate, respectively. Refinements must be made in proportion to the differing orders of accuracy, otherwise the convergence rate will be obscured.

Table 4.7: Meshes used in QD MMS convergence study for $C = 0$, where $h_s = 10$ cm and $h_t = 1$ s. All simulations use $Z = 100.0$ cm, $R = 100.0$ cm, and $T = 1.0$ s.

Δz	Δr	Δt
h_s	h_s	h_t
$h_s/2$	$h_s/2$	h_t
$h_s/4$	$h_s/4$	h_t
$h_s/8$	$h_s/8$	h_t
$h_s/10$	$h_s/10$	h_t

Table 4.8: Meshes used in QD MMS convergence study for $C = 1$, where $h_s = 10$ cm and $h_t = 1$ s. All simulations use $Z = 100.0$ cm, $R = 100.0$ cm, and $T = 1.0$ s.

Δz	Δr	Δt
h_s	h_s	h_t
$h_s/2$	$h_s/2$	$h_t/4$
$h_s/4$	$h_s/4$	$h_t/16$
$h_s/8$	$h_s/8$	$h_t/64$
$h_s/10$	$h_s/10$	$h_t/100$

Figures 4.4 and 4.5 show the results, measured in the 2- and ∞ -norm, of the

Table 4.9: Nuclear data used on the meshes in Tables 4.7 and 4.8.

Σ_t	Σ_s	Σ_f	ν	v
1.0	0.5	0.25	2.0	100

convergence study for the problems described in Table 4.6 .

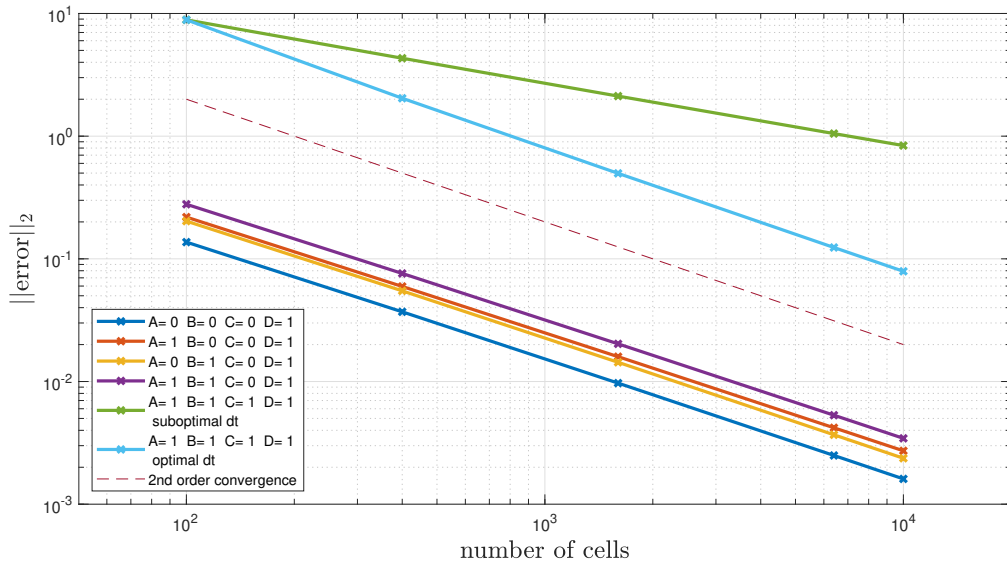


Figure 4.4: QD convergence study for MMS problems. Errors are measured with the 2-norm from the scalar fluxes and currents.

Nearly all problem variations in Figure 4.4 exhibited the expected second-order convergence. One variation was simulated with suboptimal selections for Δt to demonstrate the necessity of refining the time mesh in correct proportion to refinements in the spatial mesh. This suboptimal variation utilized a linear refinement of Δt instead of the correct squared refinement and, as a result, exhibited first-order convergence.

Figure 4.5 shows the time-dependent problem exhibiting second-order conver-

gence. The other problem variations, except for suboptimal Δt , began to approach second-order convergence, after an initial decrease, as the mesh was refined. This behaviour is most easily observed in Table 4.10.

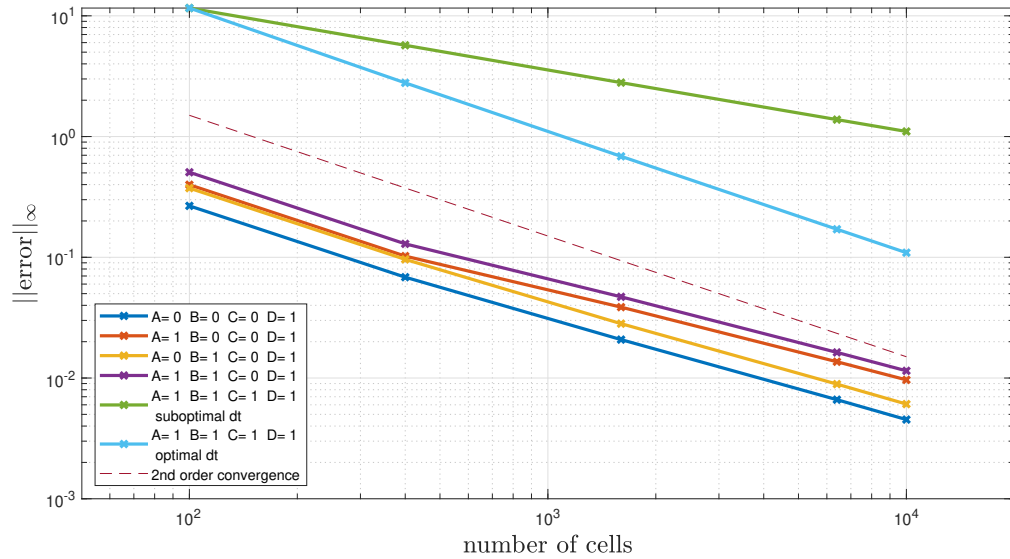


Figure 4.5: QD convergence study for MMS problems. Errors are measured with the ∞ -norm from the scalar fluxes and currents.

Table 4.10: Convergence rates in the ∞ -norm.

Problem Type	A	B	C	D	α_1	α_2	α_3	α_4
Diffusion physics	0	0	0	1	1.962	1.717	1.653	1.700
Transport physics	0	1	0	1	1.963	1.404	1.502	1.550
	1	0	0	1	1.960	1.768	1.663	1.707
	1	1	0	1	1.970	1.458	1.530	1.572
Time dependent	1	1	1	1	-	-	-	-
suboptimal Δt	-	-	-	-	1.024	1.027	1.018	1.012
optimal Δt	-	-	-	-	2.059	2.021	2.007	2.003

The α values in Table 4.10 measure the convergence rate between refinement levels. For example,

$$\alpha_1(A, B, C, D) = \frac{\log(\text{error}(A, B, C, D, h_s)) - \log(\text{error}(A, B, C, D, h_s/2))}{\log(h_s) - \log(h_s/2)}. \quad (4.20)$$

The values for α_1 demonstrate approximate second-order convergence, but the second refinement showed a drop in the convergence rate (reflected in the α_2 values) for all but the time-dependent problems. This drop is not unusual; the ∞ -norm returns the largest error on the mesh and, between refinement levels, the cell that contains this error may change. On the first refinement step, the largest error appears to have been in a cell in the convergent regime, while in subsequent steps the largest errors were in cells approaching the convergent regime.

Figure 4.4 and 4.5 indicate the QD discretizations are valid and implemented

correctly.

4.1.3 Heat transfer

The heat transfer solver was verified on an independent formulation of (3.71e).

$$\frac{\partial(\rho c_p T)}{\partial t} - \frac{\kappa}{r} \frac{\partial}{\partial r} \left(r \frac{\partial}{\partial r} T \right) - \kappa \frac{\partial^2}{\partial z^2} T + \frac{\partial(\vec{u} \rho c_p T)}{\partial z} = \omega_f \Sigma_f \Phi, \quad (4.21)$$

where Φ was some constant, not ϕ as solved by the ELOT system. The flow velocity \vec{u} was also assumed to be constant.

The following solution was prescribed for the temperature

$$T_{MMS} = \Pi \cos \left(\frac{\pi r}{2R} \right) \left(1 - \cos \left(\frac{2\pi z}{Z} \right) \right) e^{ct}. \quad (4.22)$$

Substituting the solution into Eq. (4.21) yields

$$\begin{aligned} \frac{\partial(\rho c_p T_{MMS})}{\partial t} - \frac{\kappa}{r} \frac{\partial}{\partial r} \left(r \frac{\partial}{\partial r} T_{MMS} \right) - \kappa \frac{\partial^2}{\partial z^2} T_{MMS} + \frac{\partial(\vec{u} \rho c_p T_{MMS})}{\partial z} \\ = \omega_f \Sigma_f \Phi + Q_{MMS}, \end{aligned} \quad (4.23)$$

where

$$\begin{aligned} Q_{MMS} = e^{ct} \left(1 - \cos \left(\frac{2\pi z}{Z} \right) \right) \left[A \cos \left(\frac{\pi r}{2R} \right) + \frac{B \left(\sin \left(\frac{\pi r}{2R} \right) + \frac{\pi r}{2R} \cos \left(\frac{\pi r}{2R} \right) \right)}{r} \right] \\ + e^{ct} \cos \left(\frac{\pi r}{2R} \right) \left[D \cos \left(\frac{2\pi z}{Z} \right) + F \sin \left(\frac{2\pi z}{Z} \right) \right] - \omega_f \Sigma_f \Phi, \end{aligned} \quad (4.24)$$

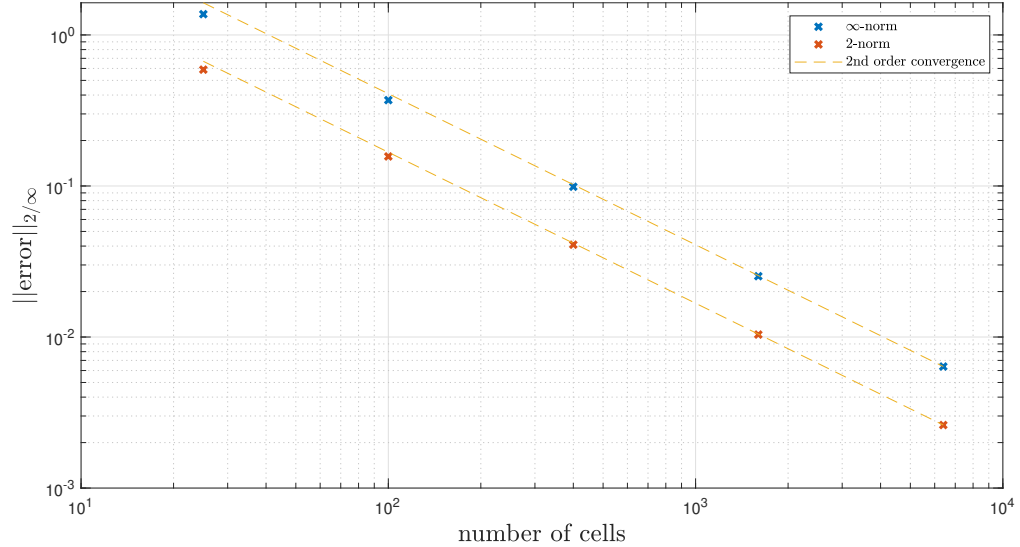


Figure 4.6: Heat transfer convergence study for MMS problem.

The expected second-order convergence was observed, indicating the discretizations for the heat transfer equation are valid and implemented correctly.

4.1.4 DNP balance

The DNP balance solver was verified on a single-group, independent formulation of Eq. (2.1b).

$$\frac{\partial}{\partial t}C + \frac{\partial}{\partial z}(\vec{u}C) = \beta\nu\Sigma_f\Phi - \lambda C \quad (4.26)$$

As in the previous section, Φ is a constant.

The following solution was prescribed for C

$$C_{\text{MMS}} = \Pi \cos\left(\frac{\pi r}{2R}\right) \left(1 - \cos\left(\frac{2\pi z}{Z}\right)\right) e^{Ct}. \quad (4.27)$$

Substitution of this solution produces

$$\frac{\partial}{\partial t} C_{\text{MMS}} + \frac{\partial}{\partial z} (\vec{u} C_{\text{MMS}}) = \beta \nu \Sigma_f \Phi - \lambda C_{\text{MMS}} + Q_{\text{MMS}}, \quad (4.28)$$

where

$$\begin{aligned} Q_{\text{MMS}} &= (A + D) \cos\left(\frac{\pi r}{2R}\right) \left(1 - \cos\left(\frac{2\pi z}{Z}\right)\right) e^{Ct} \\ &\quad + B \cos\left(\frac{\pi r}{2R}\right) \sin\left(\frac{2\pi z}{Z}\right) e^{ct} - \beta \nu \Sigma_f \Phi, \end{aligned} \quad (4.29)$$

and

$$A = \Pi c, \quad (4.30\text{a})$$

$$B = \frac{2\Pi\pi\vec{u}}{Z}, \quad (4.30\text{b})$$

$$D = \Pi\lambda. \quad (4.30\text{c})$$

Solutions were computed on the meshes in Table 4.13 with the data in Table 4.14.

Table 4.13: Meshes used in DNP balance MMS convergence study where $h_s = 0.1$ cm and $h_t = 0.2$ s. All simulations use $Z = 1.0$ cm, $R = 1.0$ cm, and $T = 0.2$ s.

Δz	Δr	Δt
h_s	h_s	h_t
$h_s/2$	$h_s/2$	$h_t/4$
$h_s/4$	$h_s/4$	$h_t/16$
$h_s/8$	$h_s/8$	$h_t/64$
$h_s/16$	$h_s/16$	$h_t/256$

Table 4.14: Data used on the meshes in Table 4.13.

\vec{u}	Φ	Π	c	β	ν	Σ_f	λ
0.4	1.0	10.0	0.1	0.007	2.0	10.0	0.1

Figure 4.7 shows the results of the MMS convergence study.

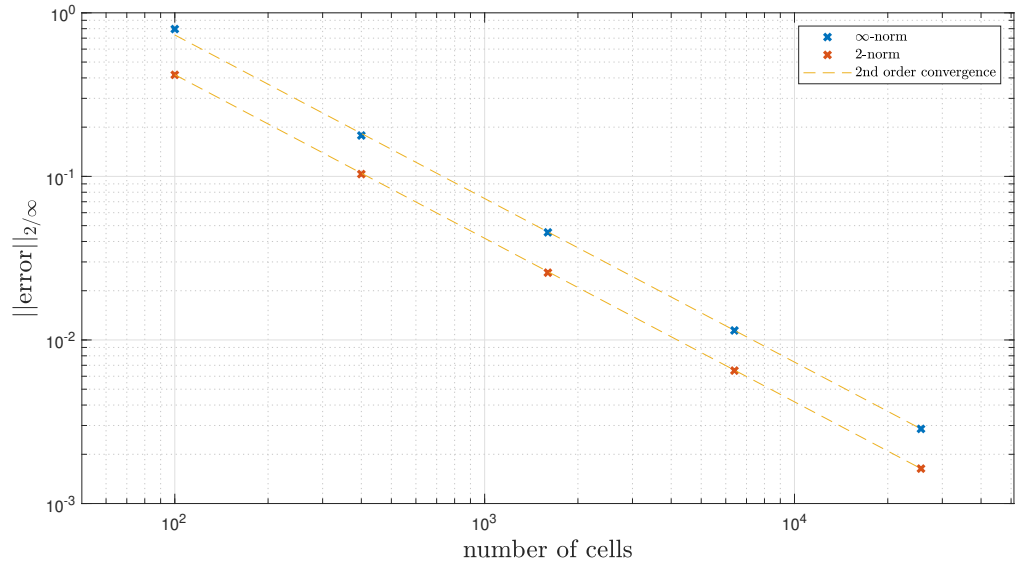


Figure 4.7: DNP balance convergence study for MMS problem.

The error decreased with the expected second-order convergence. This indicates the discretizations for the DNP balance equations are valid and implemented correctly.

4.2 Residual balance parameter study

A study of the influence of the balance factors on solution time was conducted to inform selections for τ . The balance factors on each level of Algorithms 3 and 4 were assumed equal, i.e. $\tau_{\text{MGLOQD}} = \tau_{\phi,2} = \tau_{T,2}$ and $\tau_{\text{ELOT}} = \tau_{\phi,3} = \tau_{T,3} = \tau_{k_{\text{eff}}}$. The values of in Table 4.15 were considered for each of the balance factors τ_{ELOT} and τ_{MGLOQD} , resulting in 16 total cases.

With a balance factor of one, a reduction in the residual at an inner level beyond

that of the nearest outer level will force the algorithm to move to the nearest outer level. A balance factor of zero requires the residual at an inner level to satisfy the absolute convergence criteria before moving to an outer level. The intermediate values allow for a reduced convergence criteria to be met.

The extremes are represented by ($\tau_{\text{ELOT}} = 1, \tau_{\text{MGLOQD}} = 1$) and ($\tau_{\text{ELOT}} = 0, \tau_{\text{MGLOQD}} = 0$). The former is referred to as the sequential algorithm as, generally, only one solve is performed at each level before alternating to the next. The sequential algorithm features the most frequent communication between the levels. The latter closely resembles fixed-point iteration, the exceptional detail being the interrupt action, and features the least frequent communication between the levels.

Except where noted, the interrupt action was parametrized by $\theta = 1$, meaning any increase in the residual at an inner level forces the algorithm to the nearest outer level.

The problems were run on the MSRE problem described extensively in Section 4.4.1, used nuclear data generated with SCALE, and modeled two neutron energy groups and six DNP groups. The mesh parameters in Table 4.16 were used.

Table 4.15: Balance factors used in parameter study.

τ
1 1E-2 1E-4 0

Table 4.16: Mesh parameters for residual balance parameter study.

Δz [cm]	Δr [cm]	Δt [s]
5	0.3125	0.0005

The reported solution times are for a single run of each case on the Rogue com-

puting server at Oregon State University and should not be mistaken for statistical averages calculated from multiple runs. These run times are reported to provide a coarse metric for evaluating the performance of the various iterative approaches. A study to identify the optimal selections for the balance parameters would benefit from a statistical approach under controlled computing conditions. Here, the intent is to identify general trends.

In addition to the solve times for each case, the numbers of MGHOT, MGLOQD, and ELOT iterations are detailed. A transient and steady-state solve are considered.

4.2.1 Transient

Figure 4.8 shows the solve times for the transient cases. The sequential algorithm

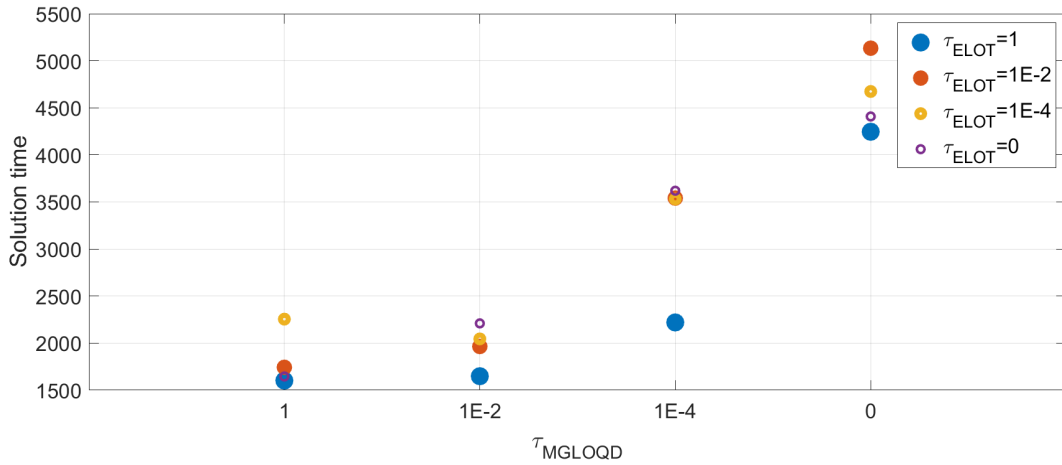


Figure 4.8: Transient solve times [s] for a variety of balance factors τ .

defined by ($\tau_{\text{ELOT}}=1$, $\tau_{\text{MGLOQD}}=1$) resulted in the shortest solve time, although

those at ($\tau_{\text{ELOT}} = 1$, $\tau_{\text{MGLOQD}} = 1\text{E-}2$) and ($\tau_{\text{ELOT}} = 0$, $\tau_{\text{MGLOQD}} = 1$) were only slightly longer. The choice of τ_{MGLOQD} had a significant impact on the solve time, with larger values generally leading to greater efficiency. This indicates that frequent exchanges of data between the MGHOT and MGLOQD levels encourages more rapid convergence for the problem considered.

The MGHOT, MGLOQD, and ELOT iterations required in each case are shown in Figures 4.9, 4.10, and 4.11.

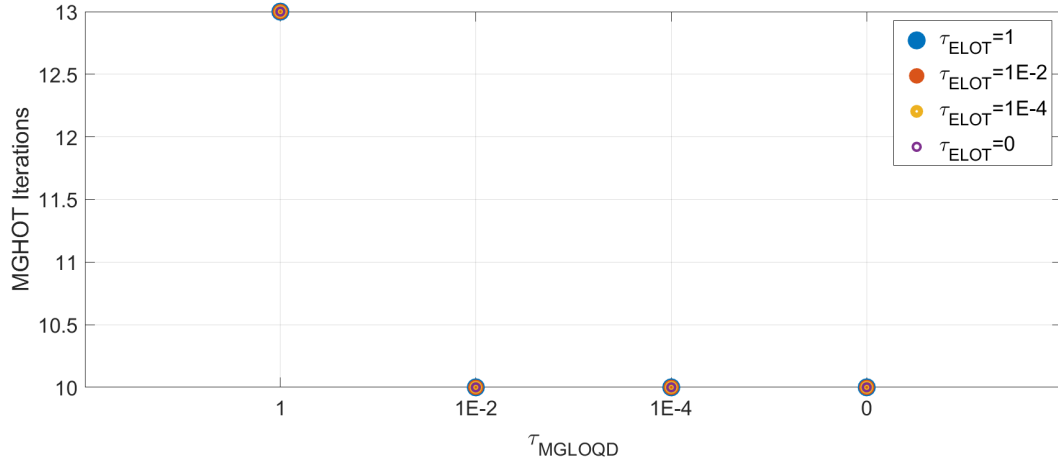


Figure 4.9: MGHOT iterations in a transient solve for a variety of balance factors τ .

The number of MGHOT iterations is independent of the selection of τ_{ELOT} and is flat for $\tau_{\text{MGLOQD}} < 1$. As expected, the MGHOT iterations peak at $\tau_{\text{MGLOQD}} = 1$, where iterating between the MGHOT and MGLOQD levels is most highly encouraged. Overall, differing values of the balance parameters produce little variation in the number of MGHOT iterations.

Figure 4.10 shows the number of MGLOQD iterations to be independent of

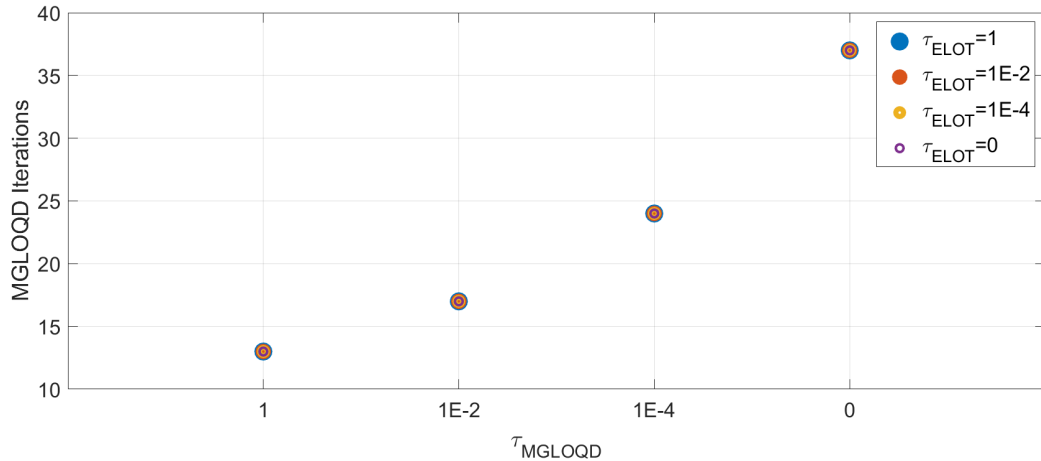


Figure 4.10: MGLOQD iterations in a transient solve for a variety of balance factors τ .

τ_{ELOT} while again demonstrating the efficiency gains of tight coupling between the MGLOQD and MGHOT levels. Figure 4.11 shows much of the same for the ELOT iterations, except cases with $\tau_{\text{ELOT}} = 1$ require markedly fewer iterations. This indicates that frequent exchange of information between the MGLOQD and ELOT levels also encourages more rapid convergence.

Note that the fastest solve using ($\tau_{\text{ELOT}}=1$, $\tau_{\text{MGLOQD}}=1$) minimized the number of MGLOQD and ELOT iterations, but not the number of MGHOT iterations. It was expected that the MGHOT solution would be the most computationally expensive to compute, but as illustrated in Table 4.17, this was not the case on the mesh considered.

The ELOT solves were most expensive due to the size of the linear system at that level, which was larger than that of the MGLOQD system because six DNP groups were modeled. This explains the much shorter MGLOQD average

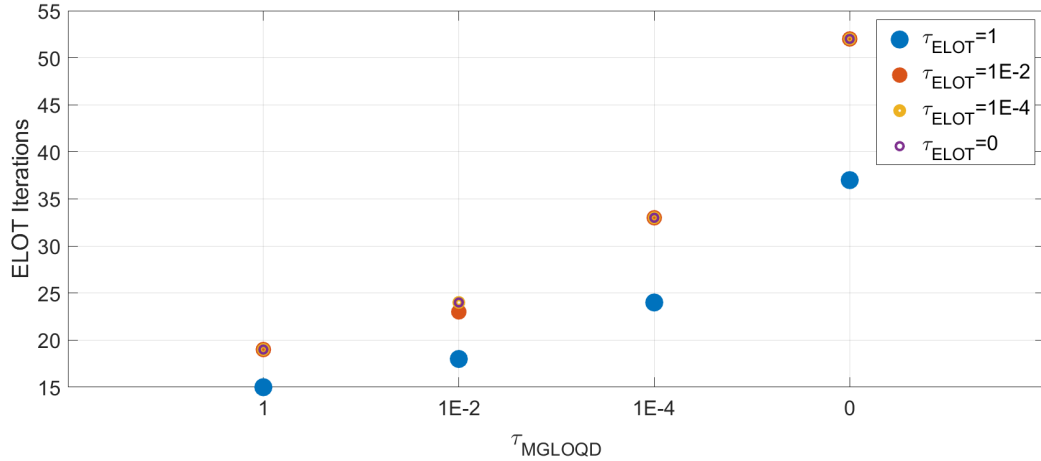


Figure 4.11: ELOT iterations in a transient solve for a variety of balance factors τ .

Level	Average solve time [s]
MGHOT	1.56
MGLOQD	19.21
ELOT	87.23

Table 4.17: Average solve times for transient case with ($\tau_{\text{ELOT}}=1$, $\tau_{\text{MGLOQD}}=1$).

solve time. Despite needing to loop over the angular and spatial meshes, the MGHOT average solve time was less than 2 seconds. This unexpected expedience is most likely due to algorithmic differences in the solution approaches between the transport and QD levels. The transport approach marches across the mesh solving small systems of a fixed size (4x4) while the QD approach forms a single linear system across the whole mesh.

It should be noted that for greater numbers of energy groups and finer angular meshes, these dynamics could change considerably. For example, modeling a single additional neutron energy group would make the MGLOQD linear system larger,

and generally more expensive to solve, than the ELOT system.

To investigate the impact of the interrupt events of Algorithm 3, these cases were repeated while disabling the feature. The solution times are shown in Figure 4.12.

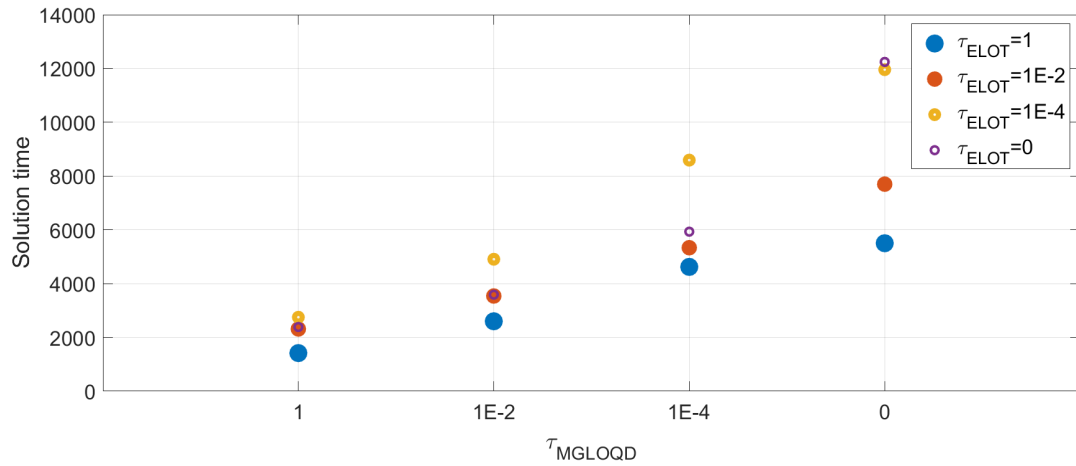


Figure 4.12: Transient solve times [s] for a variety of balance factors τ without the interrupt event.

The fastest solve is similar to that featuring the interrupt event and is also characterized by ($\tau_{\text{ELOT}}=1$, $\tau_{\text{MGLOQD}}=1$). This agreement is expected, as when ($\tau_{\text{ELOT}}=1$, $\tau_{\text{MGLOQD}}=1$) an increase in residual that may trigger the interrupt is irrelevant; these definitions will cause the algorithm to move to a solve at an outer loop regardless.

For all the other cases, however, larger solution times are observed relative to those in Figure 4.8, indicating that this check, which is simple to implement, can accelerate convergence. In the case of strict fixed-point iteration ($\tau_{\text{ELOT}}=0$, $\tau_{\text{MGLOQD}}=0$), for example, the interrupt event reduces solve time by almost a factor

of three.

4.2.2 Steady state

The steady state solution times are shown in Figure 4.13. Large values for τ_{ELOT} , which define a tighter coupling between the MGLOQD and ELOT levels, were found to result in shorter solve times, particularly when $\tau_{\text{MGLOQD}} \neq 0$. The fixed-point iteration algorithm ($\tau_{\text{ELOT}} = 0, \tau_{\text{MGLOQD}} = 0$) was found to have the longest solve time.

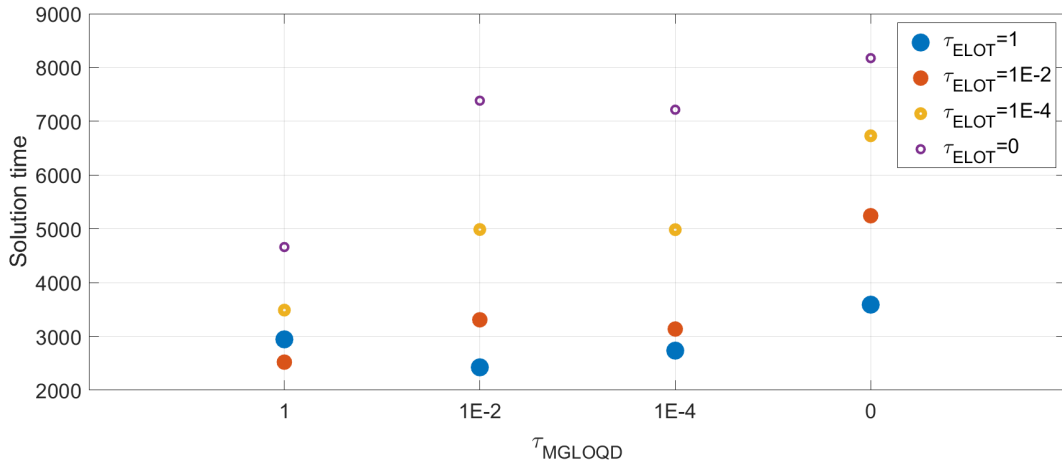


Figure 4.13: Steady state solve times for a variety of balance factors τ .

Details on the number of MGHOT, MGLOQD, and ELOT iterations required in the steady-state solve are shown in Figures 4.14, 4.15, and 4.16. Similar to the transient case, the number of MGHOT iterations varied mildly, except for the closely coupled sequential algorithm ($\tau_{\text{ELOT}}=1, \tau_{\text{MGLOQD}}=1$). Cases with close coupling of the MGLOQD and ELOT levels required a greater number of MGLOQD

iterations, as seen in Figure 4.15.

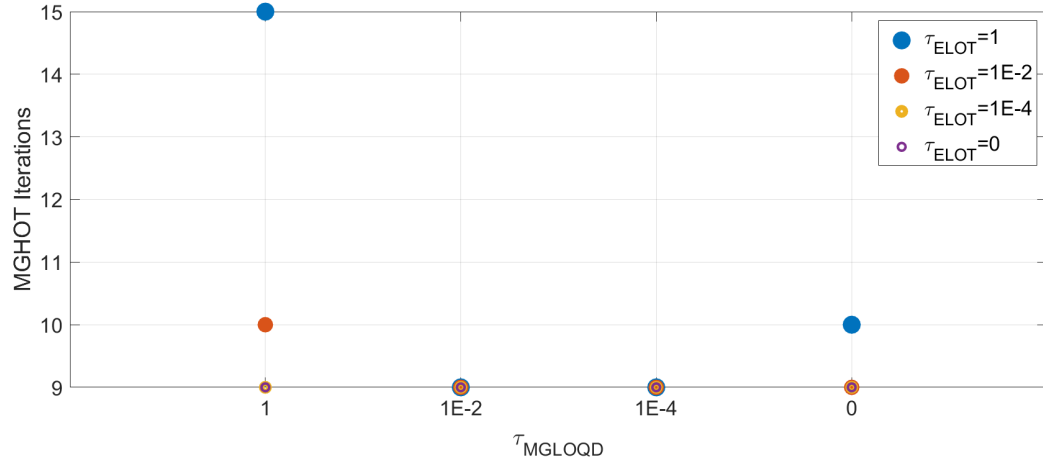


Figure 4.14: MGHOT iterations in a transient solve for a variety of balance factors τ .

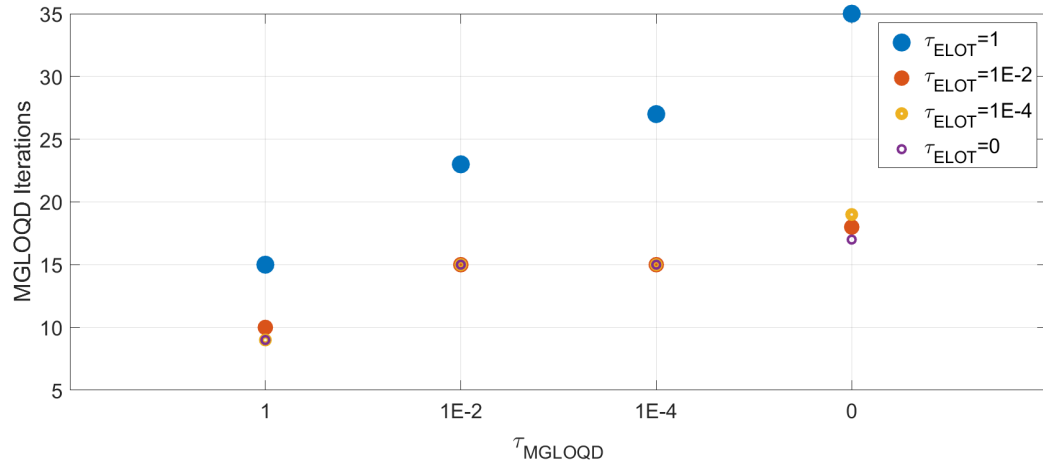


Figure 4.15: MGLOQD iterations in a transient solve for a variety of balance factors τ .

The distribution of ELOT iterations in Figure 4.16 closely resembles the overall solution times in Figure 4.13. As the ELOT solution requires the most time, this

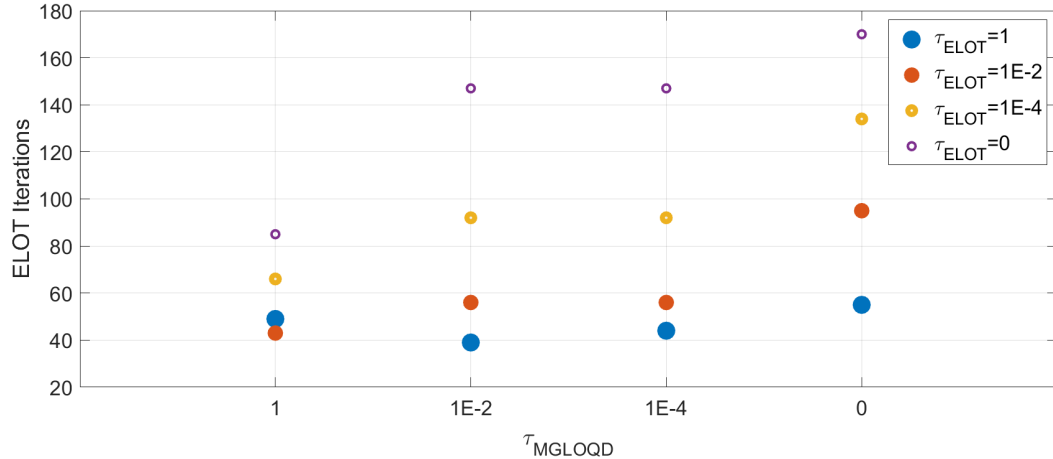


Figure 4.16: ELOT iterations in a transient solve for a variety of balance factors τ .

is expected.

As before, tight coupling between the levels was found to accelerate convergence. To illustrate the effect the balance factors have on convergence behaviour, residuals for a poorly optimized case and a better optimized case are presented. A sawtooth pattern indicative of oversolving can be clearly observed in the residual plot of the poorly optimized case ($\tau_{\text{ELOT}} = 0, \tau_{\text{MGLOQD}} = 0$) shown in Figure 4.17. Large jumps in the residuals suggest the solutions at inner levels were converged to a degree exceeding the resolution of features in the outer levels. This type of behaviour is expected for $(\tau_{\text{ELOT}} = 0, \tau_{\text{MGLOQD}} = 0)$, as this is the case with the most infrequent exchange of information between the three levels.

For the better optimized case ($\tau_{\text{ELOT}} = 1, \tau_{\text{MGLOQD}} = 1\text{E}-2$), the residuals in Figure 4.18 can be seen to decrease in a nearly monotonic fashion in contrast to Figure 4.17. Additionally, the solution requires far fewer iterations to reach

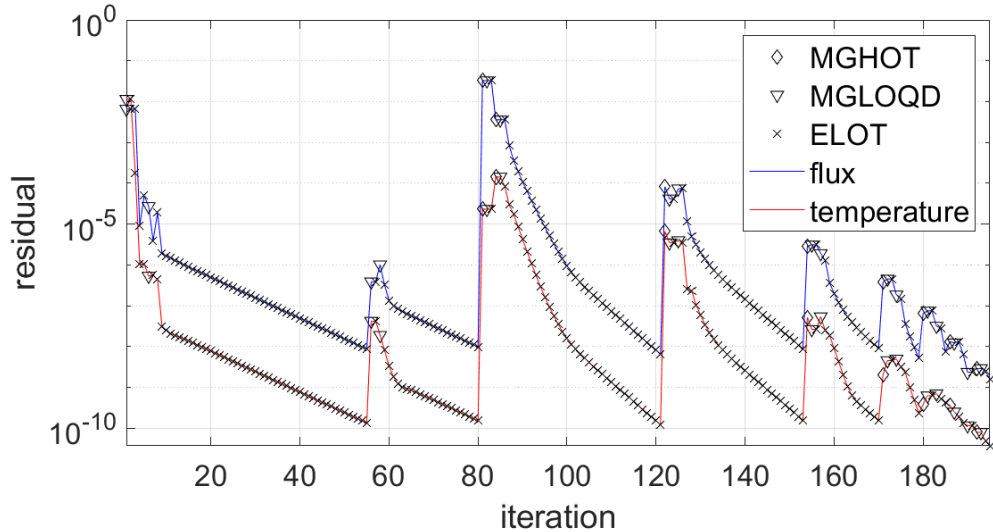


Figure 4.17: Residuals for case with $(\tau_{ELOT} = 0, \tau_{MGLOQD} = 0)$.

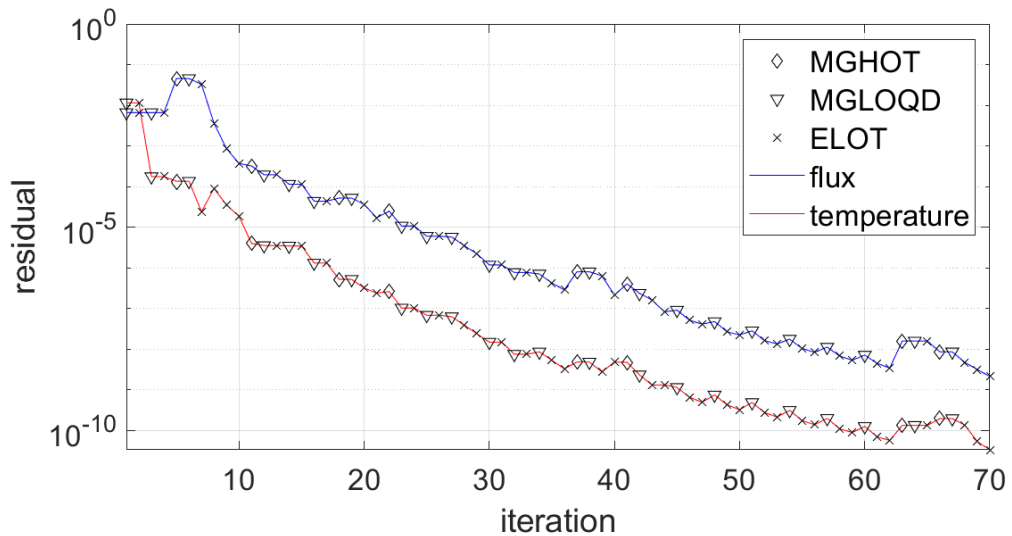


Figure 4.18: Residual behavior for case with $(\tau_{ELOT} = 1, \tau_{MGLOQD} = 1E-2)$.

convergence.

4.2.3 Remarks

In general, tighter couplings characterized by balance factors close to one were found to be favorable for simulations of the MSRE. The sequential algorithm outperformed the fixed-point iteration algorithm by a factor of approximately three in both the transient and steady-state cases. For a transient solve, it should be noted that pertinent selections for the balance factors may change as the problem develops. The findings here are based on a transient consisting of a single time step.

4.3 Transient simulation

A two-group transient was simulated to demonstrate the influence of DNP drift on reactor dynamics and verify the eigenvalue calculation in the steady state solver. The problem consists of a single material with the properties in Tables 4.18, 4.19, and 4.20. The core size and heat transfer properties are similar to those used in the MSRE, which is described in detail in Section 4.4. The solutions were computed on the mesh in Table 4.21.

Table 4.18: Scattering cross sections for homogeneous problem.

$\Sigma_{s,11}$	$\Sigma_{s,12}$	$\Sigma_{s,21}$	$\Sigma_{s,22}$
9.99	0.01	0.0	5.0

Table 4.19: Group constants for homogeneous problem.

Energy Group	Σ_t	Σ_f	χ^p	χ^d	ν
1	10.0	0.0	1.0	1.0	0
2	10.0	5.0	0.0	0.0	Figure 4.19

Table 4.20: Geometry and heat transfer parameters for homogeneous problem.

Parameter	Value	Units
Inlet temperature	920	K
Wall temperature	920	K
Core height	170	cm
Core radius	70	cm
Recirculation length	350	cm
Fuel velocity	21.45	cm s^{-1}
κ	0.0553	$\text{W cm}^{-1} \text{K}^{-1}$
c_p	1967.0	$\text{J K}^{-1} \text{kg}^{-1}$
ρ	2.146E-3	kg cm^{-3}

Table 4.21: Mesh parameters for homogeneous transient.

Δz [cm]	Δr [cm]	Δt [s]
5	5	0.015

The number of neutrons produced in a thermal fission event, shown in Figure 4.19, has been defined to introduce negative temperature feedback. With this feedback, a steady state can be reached by letting the transient simulation run for an extended period. Knowing the approximate steady-state power, a steady-state simulation can be performed to verify an approximately critical eigenvalue is calculated.

Vacuum boundary conditions were enforced on the outside boundaries. The group fluxes and DNP concentrations were initialized to $1 \text{ cm}^{-2} \text{ s}^{-1}$ and 0 cm^{-3} ,

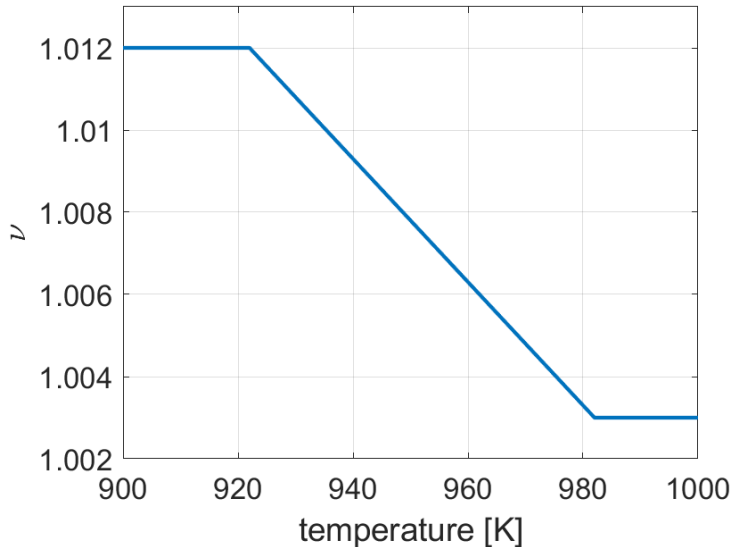


Figure 4.19: Thermal group ν .

respectively. The reactor startup phase is detailed in Section 4.3.1 and the steady-state eigenvalue calculation is detailed in Section 4.3.2.

4.3.1 Startup

The core power from 0 to 60 seconds is shown in Figure 4.20. Initially, the core is supercritical owing to low initial temperatures. The neutron population grows until roughly 8 seconds, at which point the multigroup fluxes reach a magnitude where the core temperature begins to increase as shown in Figure 4.21. At these temperatures, the multigroup fluxes, shown in Figure 4.22, are still centered on the midplane of the reactor. The DNP concentrations are similarly centered on the midplane.

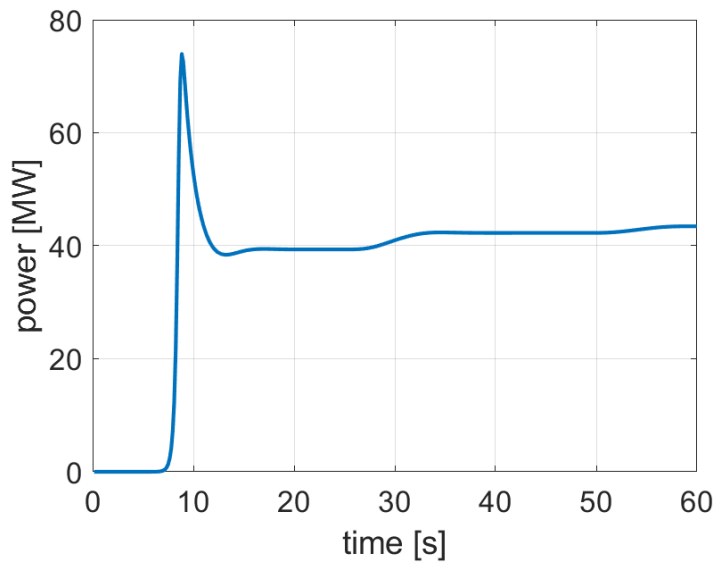


Figure 4.20: Core power during startup phase.

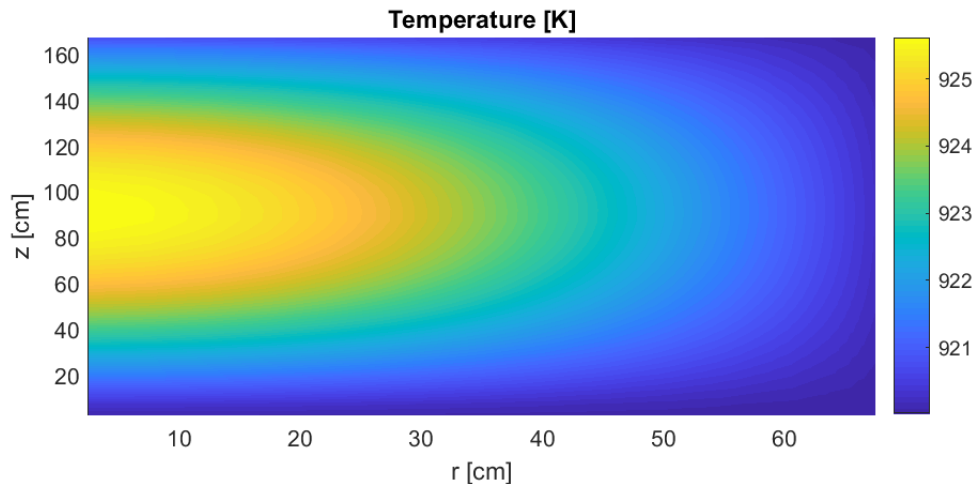


Figure 4.21: Core temperatures at 8.55 s.

Just before 10 seconds, the negative temperature feedback becomes appreciable and the power begins to decrease sharply. Shortly after, due to the movement of

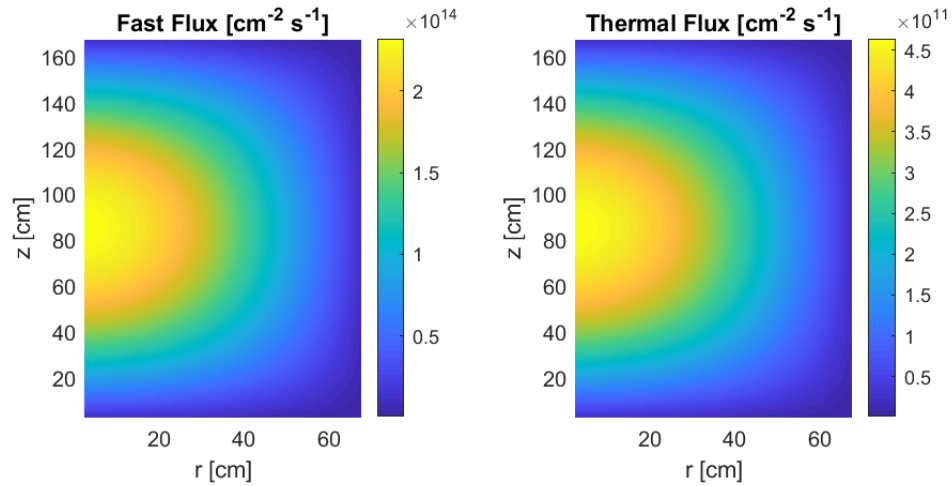


Figure 4.22: Multigroup fluxes at 8.55 s.

the fuel, the peaks of the temperature and longer-lived DNP distributions begin to shift towards the outlet as shown in Figures 4.23 and 4.24. The first of the long-lived DNPs exiting the core into the recirculation loop can also be seen in Figure 4.24.

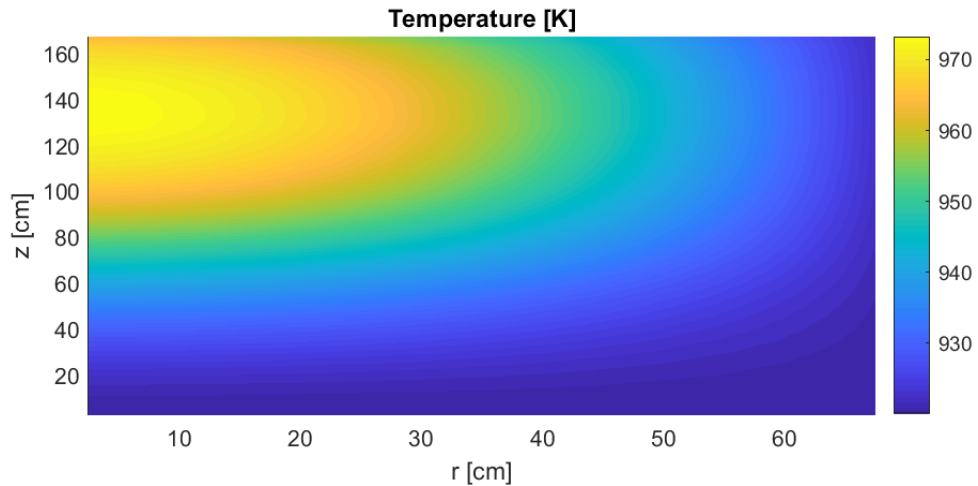


Figure 4.23: Core temperatures at 12.15 s

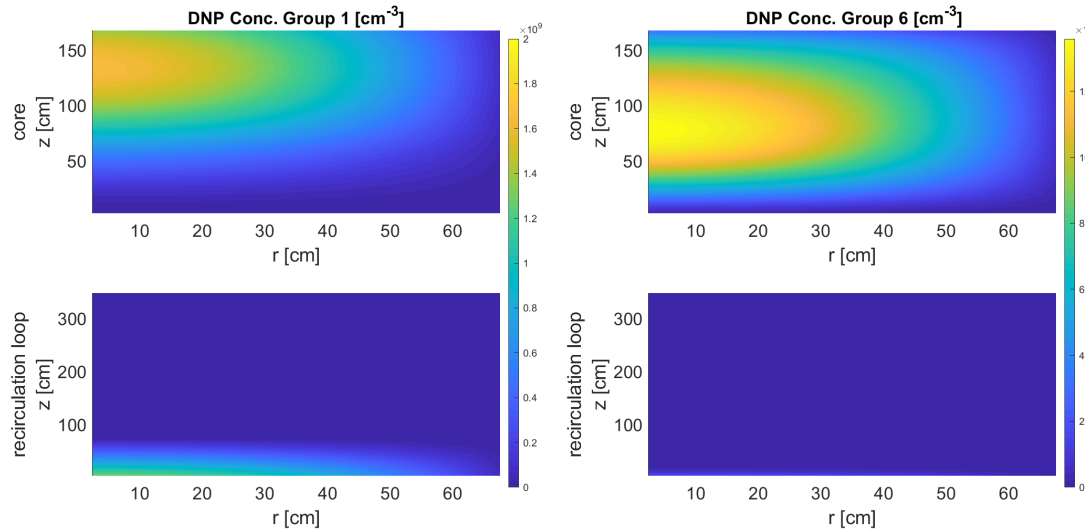


Figure 4.24: DNP concentration at 12.15 s for longest-lived (left) and shortest-lived (right) groups.

By about 20 seconds, the power has briefly plateaued after the temperature distribution has shifted squarely to the bottom of the core. Due to the negative temperature feedback, this drives the multigroup fluxes, shown in Figure 4.25, away from the midplane to center around $z = 70$ cm. At this point, the initial slug of longer-lived DNPs, shown in Figure 4.26, is roughly midway through the recirculation loop. The shortest-lived precursor group shows virtually no recirculation or shift from the midplane owing to its high decay constant.

The long-lived DNPs in the recirculation loop eventually reenter the core just before 30 seconds, causing the slight rise in power seen in Figure 4.20. Another slug, more dispersed as seen in Figure 4.27, reenters the core at around 53 seconds, causing another smaller power increase. This behaviour continues, with each wave of recirculated DNPs becoming increasingly dispersed and producing progressively

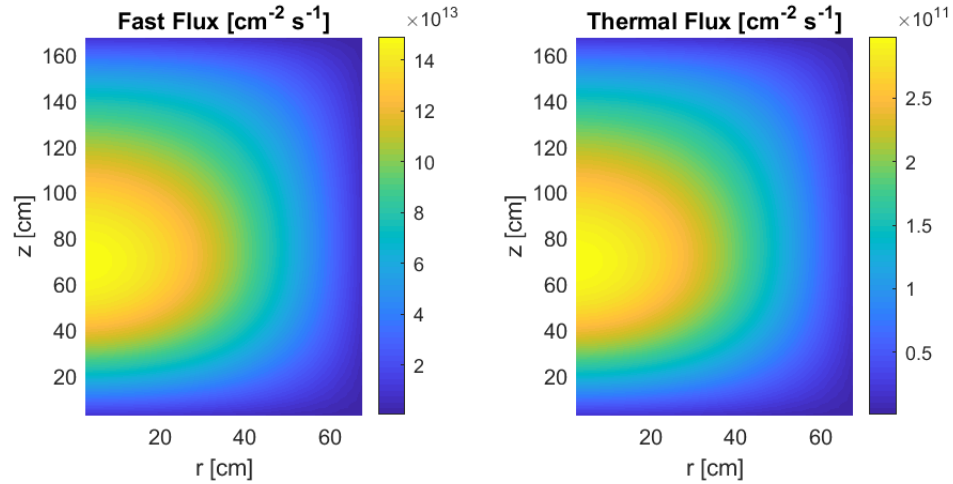


Figure 4.25: Multigroup fluxes at 21.75 s

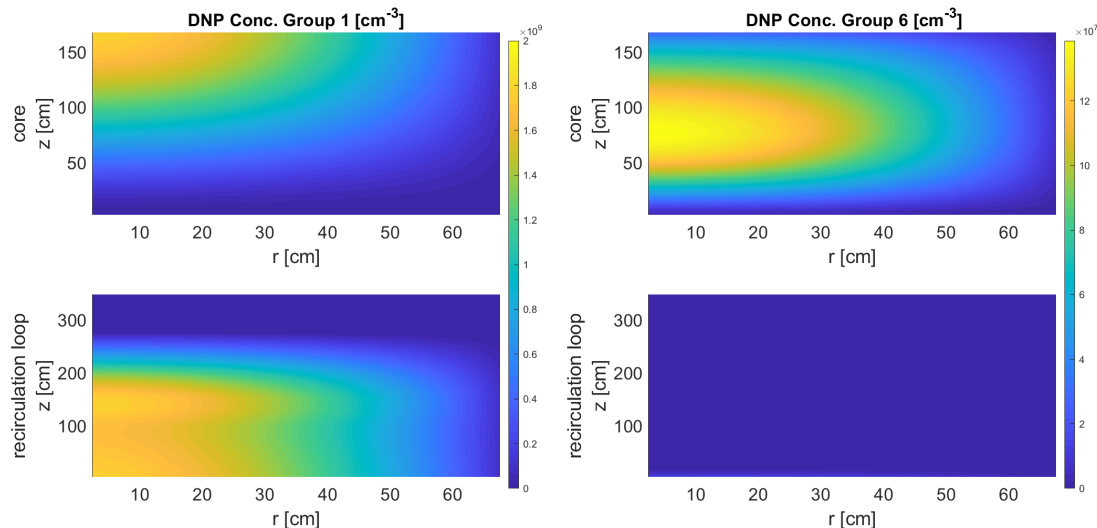


Figure 4.26: DNP concentration at 21.75 s for longest-lived (left) and shortest-lived (right) groups.

smaller changes in power while asymptotically approaching a steady state.

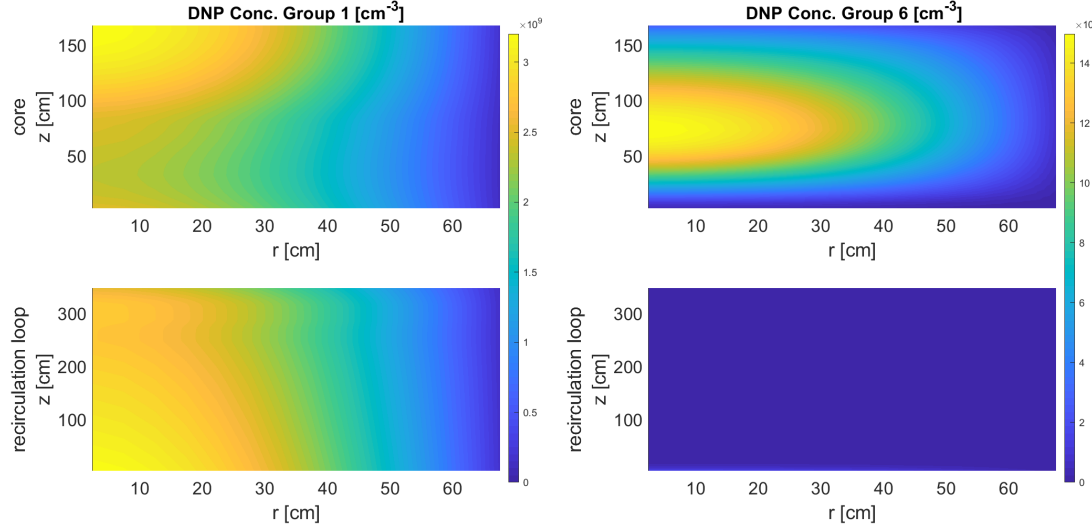


Figure 4.27: DNP concentration at 53.55 s for longest-lived (left) and shortest-lived (right) groups.

4.3.2 Steady-state eigenvalue

The core power, as shown in Figure 4.28, flattens out considerably by 200 seconds. At 600 seconds, the power is approximately 44.83 MW. Calculating a steady-state solution with the same parameters of the transient and scaling the flux to this power yields the eigenvalue in Table 4.22.

Table 4.22: k_{eff} at steady-state power of 44.83 MW.

k_{eff}	$ 1 - k_{\text{eff}} $	Approximate $\frac{dP}{dt}(600 \text{ s}) [\text{MW/s}^2]$
0.99991537113	8.46288700000E-05	2.88373135977E-05

This eigenvalue is not identically one, as would be the case for a critical reactor, however, the deviation from criticality is of the same magnitude as the approximate rate of change still occurring in the power at 600 s. Additionally, considering that

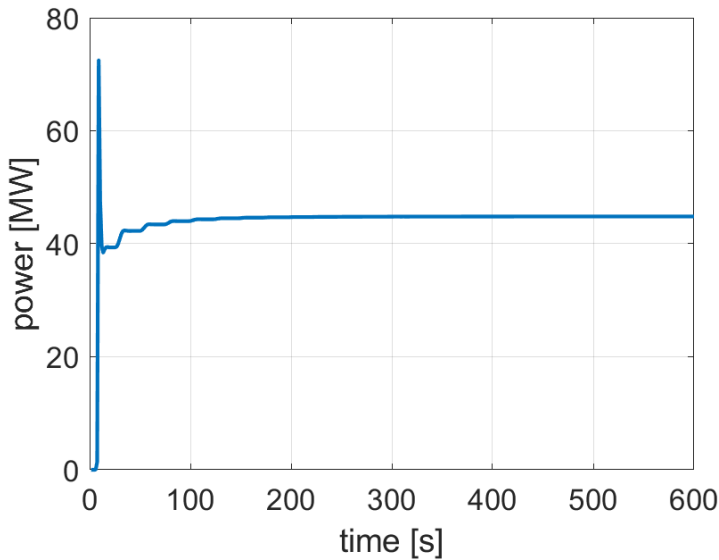


Figure 4.28: Core power out to 10 minutes.

the transient and steady-state calculations have different discretization errors and are subject to convergence criteria, this degree of agreement is reasonable.

4.4 Steady state simulation of the Molten Salt Reactor Experiment

A model of the MSRE was simulated to evaluate the performance of Quasimolto based on the ability to calculate the following quantities:

- Loss of reactivity from DNP flow
- Isothermal eigenvalue
- Fluxes and temperatures in a critical configuration

Reference values are sourced from the MOST benchmark [17] and Lindsay et

al. [34]. In the MOST benchmark, participants simulated the MSRE and reported results for a number steady-state and transient quantities. These included the reactivity loss from DNP flow, coefficient of reactivity for the modeled materials, and behaviour during pump start-up, pump coast-down, and natural circulation events. Lindsay et al. compared results from their code, Moltres, to design calculations for the MSRE [64, 24].

4.4.1 Modeling parameters

The MSRE was modeled with the parameters in Table 4.23.

Table 4.23: As-modeled MSRE parameters.

Parameter	Value	Units	Source
Inlet temperature	922	K	[65]
Wall temperature	922	K	[65]
Core height	170	cm	≈ 170.18 cm [65]
Core radius	70	cm	≈ 69.85 cm [65]
Recirculation length	350	cm	Derived [64]
Fuel velocity	21.45	cm s^{-1}	Derived [65]
k_{fuel}	0.0553	$\text{W cm}^{-1} \text{K}^{-1}$	[65]
$c_{\text{p,fuel}}$	1967.0	$\text{J K}^{-1} \text{kg}^{-1}$	[65]
ρ_{fuel}	2.146E-3	kg cm^{-3}	[65]
k_{mod}	0.3120	$\text{W cm}^{-1} \text{K}^{-1}$	[46]
$c_{\text{p,mod}}$	1760.0	$\text{J K}^{-1} \text{kg}^{-1}$	[46]
ρ_{mod}	1.860E-3	kg cm^{-3}	[65]

The fuel velocity was derived from the fuel channel geometry (1.2 in x 0.4 in), the total number of fuel channels (1140), and the nominal fuel pump flow rate

(1200 gal/min) given for the MSRE.

$$\frac{1200 \text{ gal/min}}{1140 * 1.2 \text{ in} * 0.4 \text{ in}} * \frac{1 \text{ min}}{60 \text{ sec}} * \frac{3875.41 \text{ cm}^3}{1 \text{ gal}} * \left(\frac{1 \text{ in}}{2.54 \text{ cm}} \right)^2 \approx 21.45 \text{ cm/s.} \quad (4.31)$$

This velocity is similar to that used by Haubenreich et al. [64] (21.34 cm/s) in the initial neutronic calculations for the MSRE.

The recirculation length was derived from the recirculation time of 16.45 s used by Haubenreich et al. and assuming the flow rate in the recirculation loop matches that of the core.

$$21.45 \text{ cm/s} * 16.45 \text{ s} = 352.9 \text{ cm} \quad (4.32)$$

The length of 350 cm was chosen to accommodate uniform mesh parameters.

Geometry The as-modeled MSRE geometry was similar to that modeled by Lindsay et al. - 14 vertical fuel channels measuring 1.25 cm wide were placed 5 cm apart within a graphite matrix, as depicted in Figure 4.29. This configuration yields a fuel fraction of 0.236. The MSRE design specification for the fuel fraction was 0.225 [65].

Some simulations include control material. The as-modeled control rod geometry, detailed in Table 4.24, was chosen to replicate the volume of control material in the MSRE with rods fully inserted, which was calculated from details provided by Tolson and Taboada [66]. The control rod is hollow, as were those in the MSRE. The parameters in Table 4.24 yield a control material volume within approximately 1% of that present in the MSRE.

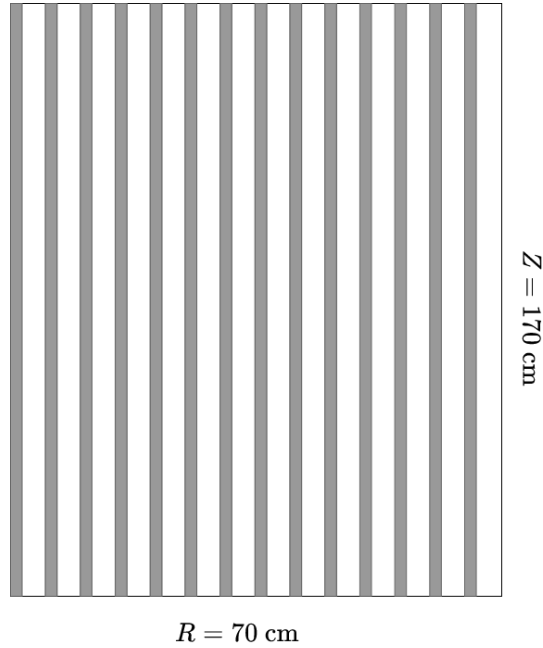


Figure 4.29: As-modeled MSRE axis-symmetric geometry. The dark and light regions denote fuel and graphite, respectively. The leftmost channel, which falls on the axis of symmetry, is half width. The control rod, not pictured, would be between the first and second (from the left) fuel channels.

Table 4.24: As-modeled control rod geometry.

Inner diameter	Outer diameter	Length
1.25 cm	2.5 cm	142.2 cm

Nuclear data Two-group nuclear data was generated with SCALE for the materials detailed in Table 4.25 using the 238-group ENDF/B-VII library [67]. 238-group fluxes were calculated by the NEWT transport module within SCALE, and then utilized in a flux-weighted group collapse. Further details on the generation of the 2-group constants, in addition to SCALE input files, can be found in Appendix D. Group constants were evaluated from 922 K to 1072 K at 50 K intervals. Linear

4.4.2 Loss of reactivity from DNP flow

This section evaluates one metric involved in the MOST benchmark: loss of reactivity due to the flow of DNPs. For consistency with the simulations under comparison, the control rod was fully withdrawn. The fluxes in these simulations were scaled to produce a power of 8 MWth. The following figures show results calculated with ENDF DNP decay data.

Figure 4.30 show the fast and thermal fluxes. A striated nature is noticeable in each; for the fast flux, higher values are observed in the fuel regions, and for the thermal flux, higher values are observed in the graphite moderator. Both fluxes peak near the midplane.

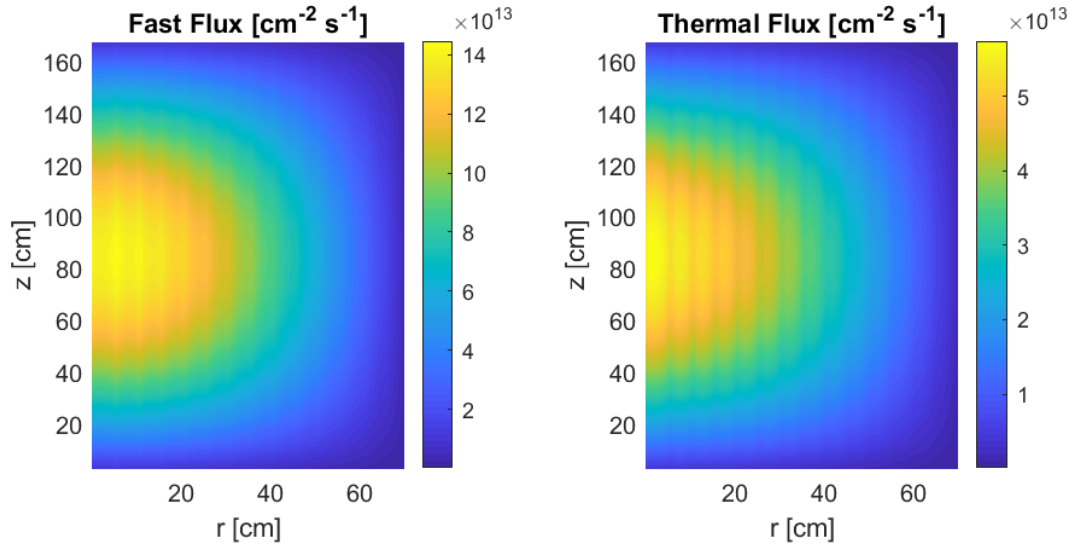


Figure 4.30: Fast (left) and thermal (right) fluxes with control rod fully withdrawn.

Figure 4.31 shows the temperature distribution. Expectedly, the temperature peaks at the outlet. Temperatures are higher in the graphite moderator, a phe-

nomena consistent with previous modeling attempts and experimental observation of the MSRE.

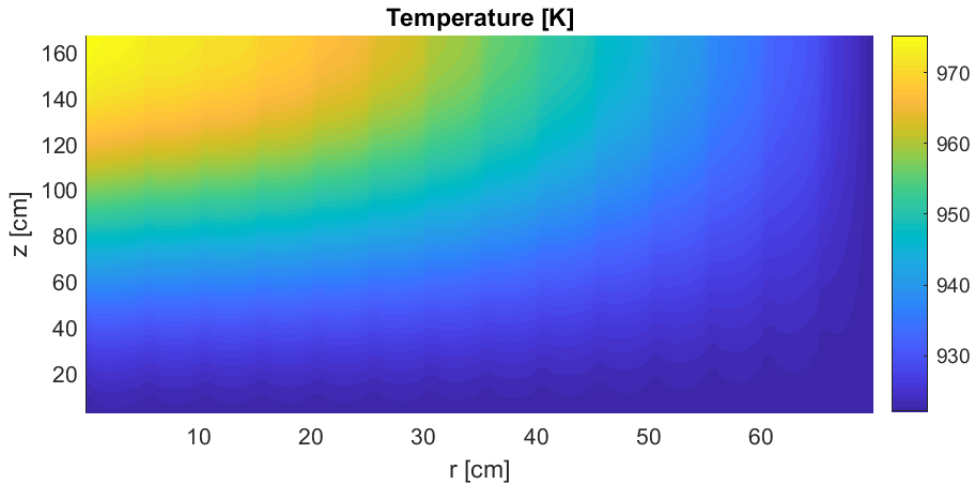


Figure 4.31: Temperature distribution with control rod fully withdrawn.

Figure 4.32, 4.33, and 4.34 show the DNP concentrations in each precursor group for the core (top) and recirculation loop (bottom) regions. As DNPs are produced through fission events and purely axial flow is assumed, the DNPs are limited to the fuel channels. For all precursor groups, the fuel channels with the highest concentrations are along the central axis, where the flux is largest. The longest-lived precursor groups, in Figure 4.32, experience significant recirculation and the concentrations peak at the core outlet.

In shorter-lived precursor groups, the recirculated concentrations decrease and the peaks of the core concentrations shift towards the midplane. This is observable in precursor group 4 of Figure 4.33, where DNPs entering the recirculation loop decay significantly before reentering the core and the peak of the core concentration

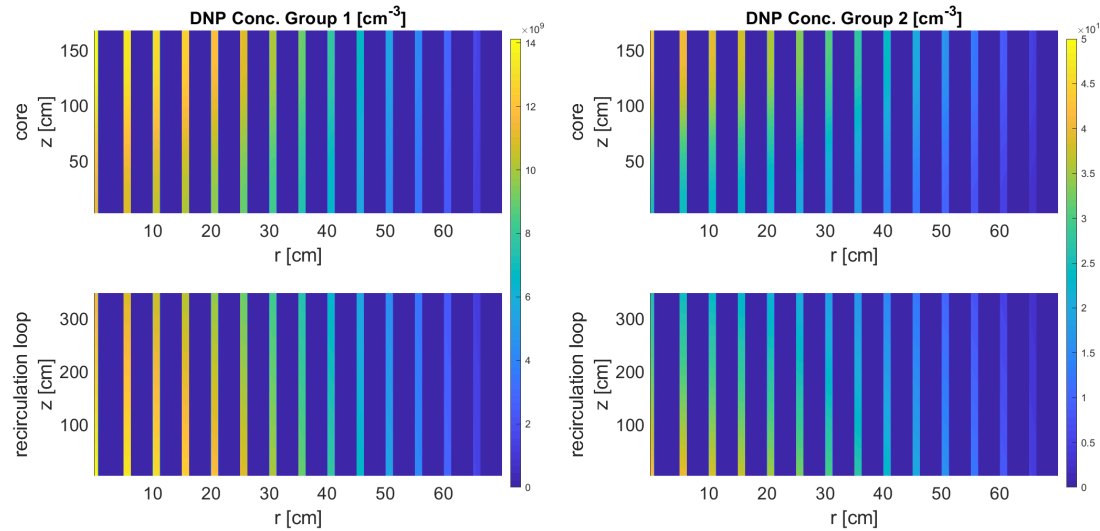


Figure 4.32: DNP concentrations for groups 1 and 2 with control rod fully withdrawn.

has shifted away from the outlet to approximately 130 cm.

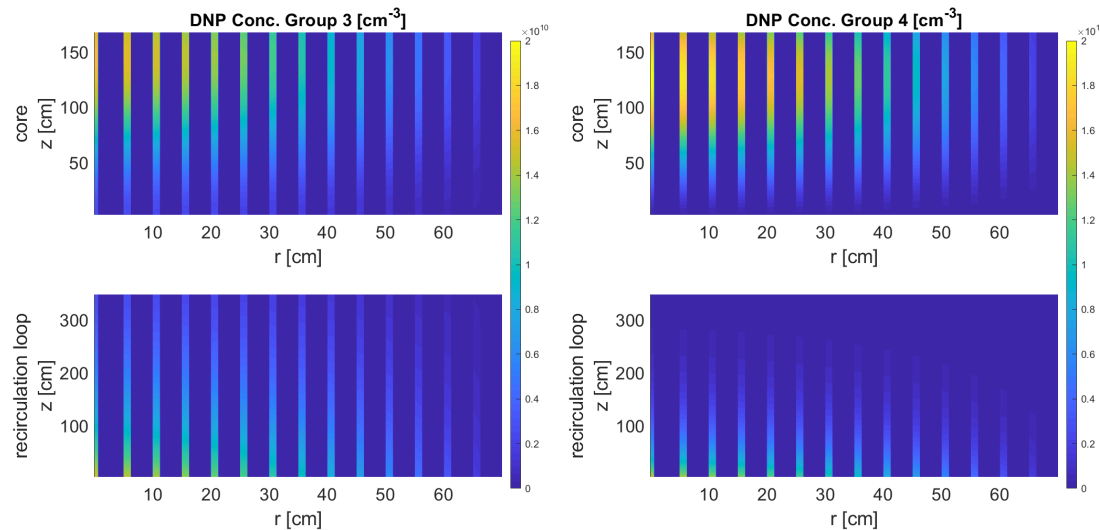


Figure 4.33: DNP concentrations for groups 3 and 4 with control rod fully withdrawn.

This behaviour grows more pronounced in the shortest-lived precursors, shown in Figure 4.34, where the magnitudes of the recirculating concentrations immediately drop off, and the core concentration for precursor group 6 peaks closest to the miplane at $z=92.5$ cm.

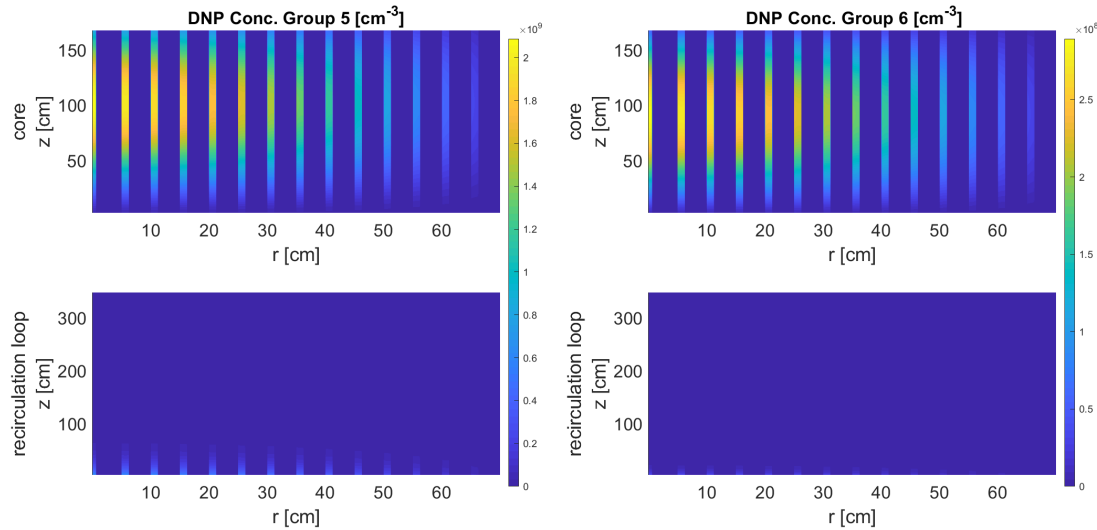


Figure 4.34: DNP concentrations for groups 5 and 6 with control rod fully withdrawn.

The DNPs that decay in the recirculation loop are a source of reactivity loss, as their delayed neutrons are emitted outside the active core region. The reactivity loss can be quantified by comparing to the eigenvalue of a system with $\beta = 0$, i.e. a system where all neutrons are produced in the active core region. Table 4.28 details the reactivity loss associated with each set of decay data.

For both the ENDF and ORNL decay data, a significant fraction of the reactivity contributed by the DNPs is lost. These losses are of similar magnitude to those calculated by MOST participants using the ORNL decay data, as well as

Table 4.28: Reactivity loss from DNP drift. The change in reactivity $\Delta\rho$ is measured relative to the system with $\beta = 0$.

Decay data	k_{eff}	ρ [pcm]	$\Delta\rho$ [pcm]
$\beta = 0$	1.059211	5590.1	—
ENDF	1.055615	5268.5	-321.6
ORNL	1.055966	5299.1	-291.0

that reported experimentally for the MSRE, as can be seen in Table 4.29.

Table 4.29: Reactivity loss from DNP drift in the MSRE at steady state as calculated by MOST participants and reported experimentally. Adapted from Table 1 in Delpech et al. [17].

Source	Type	Reactivity loss [pcm]
Prince et al. [24]	Measured	212 ± 4
Prince et al. [24]	Computed	222
Kophazi et al. [68]	Computed	244
Lecarpentier and Carpentier [19]	Computed	229
Lapenta, Mattioda, and Ravetto [69, 70]	Computed	245
Kondo et al. [71]	Computed	262
Krepel et al. [21]	Computed	253
Dulla, Rostagno, and Ravetto [72]	Computed	261
QuasiMolto (this work)	Computed	291

The loss calculated in this work is the highest among the computed values shown in Table 4.29. It is important to note that MOST participants modeled the upper and lower plenum regions of the MSRE, in contrast to the geometry used in this work. Delpech et al. [17] state “[the] effect on reactivity of the fuel motion is strongly dependent on the geometry of the upper and lower plena considered.” Prince et al. [24] also remark on the importance of plena modeling, attributing longer fuel residence times and changes in the DNP equilibrium concentrations to greater retention of DNPs in the active core region, as evidenced in Table 4.30.

Plena modeling	Reactivity loss [pcm]
No	300
Yes	222

Table 4.30: Reactivity loss from DNP drift with and without plena modeling as reported by Prince et al. [24].

Note the value calculated by Prince et al. without plena modeling compares closely to that calculated in this work. In addition to the referenced statements, this suggests plena modeling may result in a reactivity loss more closely aligned with the others in Table 4.29.

Attempts to model the plena, which feature lower fuel velocities, produced non-physical results (large temperature drops) at the fuel channel and plena boundaries. Further development in this area is left to future work, where a refinement of the energy balance discretization or, better yet, coupling to equations governing fluid flow may offer a solution.

4.4.3 Isothermal eigenvalue

The eigenvalue for an isothermal core (923.15 K) was also calculated and compared to those reported for the MOST benchmark. The comparison is presented in Table 4.31.

The eigenvalue calculated in this work is the lowest of those presented by ~ 130 pcm. Modeling the plena would most likely bring the QuasiMolto eigenvalue into closer agreement. The plena are composed entirely of fuel salt material, which would promote multiplication in the core. Furthermore, as noted in the previous

Table 4.31: Isothermal eigenvalues as calculated in this work and by some MOST participants. Adapted from Table 6 in Delpech et al. [17]. Delpech et al. do not identify which decay data was used for these calculations. ENDF decay data was used in QuasiMolto.

Source	k_{eff}
Kophazi et al. [68]	$1.0598 \pm 13 \text{ pcm}$
Lapenta, Mattioda, and Ravetto [69, 70]	1.07513
Lecarpentier and Carpentier [19]	1.06752
Krepel et al. [21]	1.06966
Dulla, Rostagno, and Ravetto [72]	1.07060
QuasiMolto (this work)	1.05852

section, the loss of reactivity due to DNP flow would decrease, further increasing the eigenvalue.

4.4.4 Critical system

An approximately critical system at 10MW was also modeled. Criticality was achieved by inserting the control rod to 60 cm from the bottom of the core.

The fast and thermal fluxes are shown in Figure 4.35. The effect of the control rod is readily apparent. Where in Figure 4.30 the flux was quite nearly centered on the central axis, here the flux has been pushed outward. The thermal flux experiences a dramatic decrease in magnitude around the control rod, as the control material is strongly absorptive to thermal neutrons. The fast flux experiences a similar effect, but to a lesser extent owing to increased transparency in the control material at higher energies. Beyond the tip of the control rod, the magnitudes of the fast and thermal fluxes increase rapidly. Farther from the central axis,

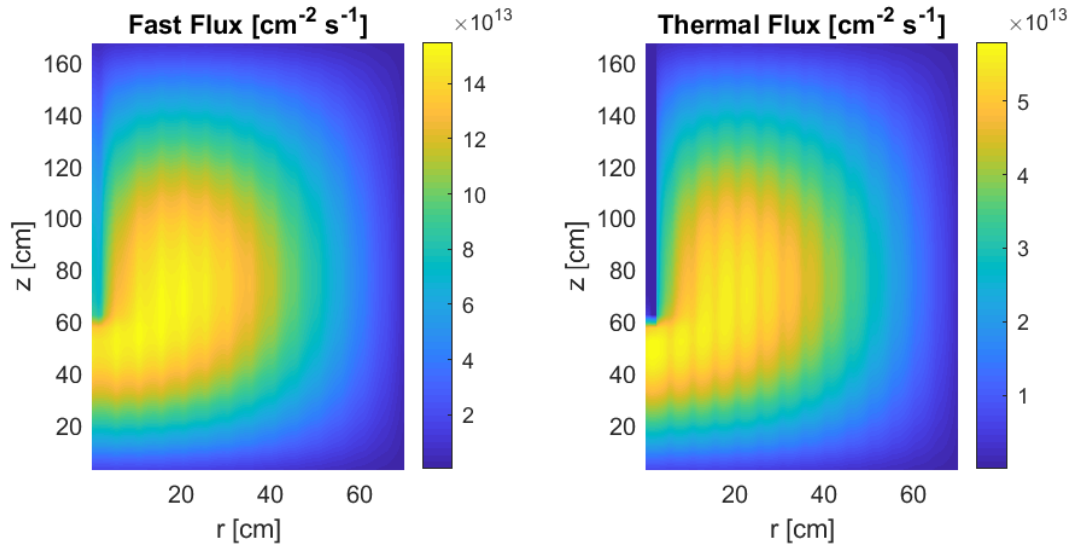


Figure 4.35: Fast and thermal fluxes with control rod inserted to 60 cm.

the fluxes look quite similar to those of the previous section - characterized by striations corresponding to material variation.

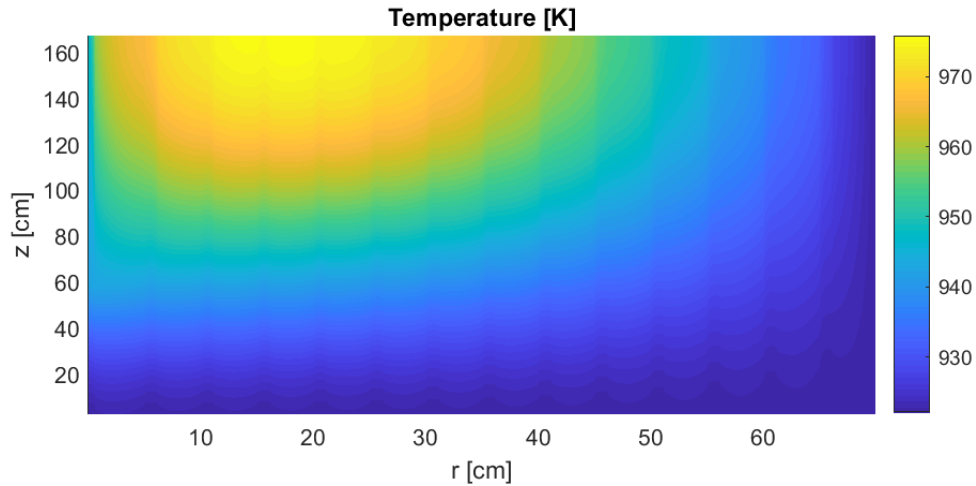


Figure 4.36: Temperature distribution with control rod inserted to 60 cm.

The temperature distribution, in Figure 4.36, reflects the flux shifting away

from the central axis. The peak outlet temperature occurs at approximately 18 cm, and the temperatures along the central axis are much lower than in the uncontrolled case (Figure 4.31) due to lower fluxes in that region. Here, again, graphite temperatures are slightly higher than the fuel temperatures.

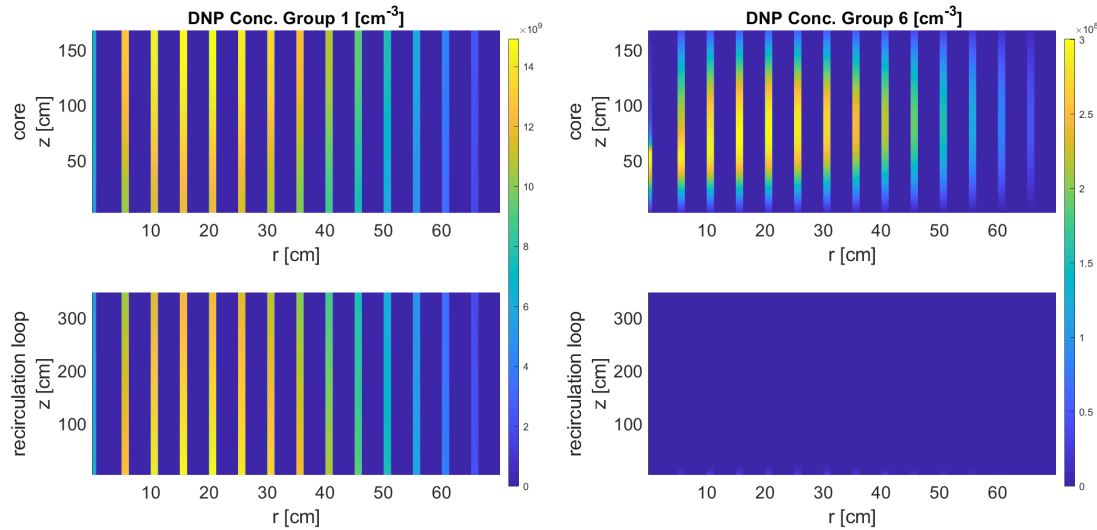


Figure 4.37: DNP concentrations for groups 1 and 6 with control rod inserted to 60 cm.

The DNP concentrations for the longest- and shortest-lived groups are shown in Figure 4.37. The highest concentrations are observed in the fuel channel 20 cm from the central axis. For precursor group 1, the fuel channel closest to the control rod has a relatively low concentration due to the depressed flux in the region. For precursor group 6, the same region sees an appreciable concentration develop immediately beyond the control rod and quickly dissipate at approximately 60 cm from the bottom of the core as the flux drops. Recirculation behaviour similar to that noted earlier is present.

4.4.4.1 Intercode comparison

To gauge the fidelity of QuasiMolto, the data in Figures 4.35 and 4.36 were compared to simulations by Lindsay et al. and Briggs. In particular, the midplane and centerline fluxes were compared, in addition to the temperatures in and around the hottest region.

The simulations to be compared have a number of variations in their as-modeled MSRE parameters, some of which are presented in Table 4.32.

Table 4.32: Variations in as-modeled MSRE parameters. All models feature 6 DNP groups and 2 neutron energy groups.

Source	Radius [cm]	Height [cm]	Plena	Control rod
Lindsay et al. [34]	72.5	150	No	No
Briggs [73]	75.08	213.51	Yes	Yes*
QuasiMolto (this work)	70	170	No	Yes

As mentioned prior, the Moltres simulation uses a similar geometry to that in Figure 4.29, but lacks any control material. According to Lindsay et al., the height of 150 cm was chosen to yield an approximately critical geometry. The as-modeled power is not stated.

The geometry of the simulation by Briggs is described thoroughly by Haubenreich et al. [64] and features explicit modeling of the plena, which contributes to the larger height of 213.41 cm. A number of structural regions are also modeled, such as the core vessel and downcomer. The control material in the simulation is assumed to be black to thermal neutrons and transparent to fast neutrons, and has additional fuel material in the surrounding area. The core is composed of a homogeneous mix of graphite and fuel material, as opposed to the channels modeled in

QuasiMolto and Moltres. The as-modeled power is 10MW.

The results from the comparison codes have been extracted from plots in “Introduction to Moltres: An application for simulation of Molten Salt Reactors” by Lindsay et al. using the WebPlotDigitizer tool [74].

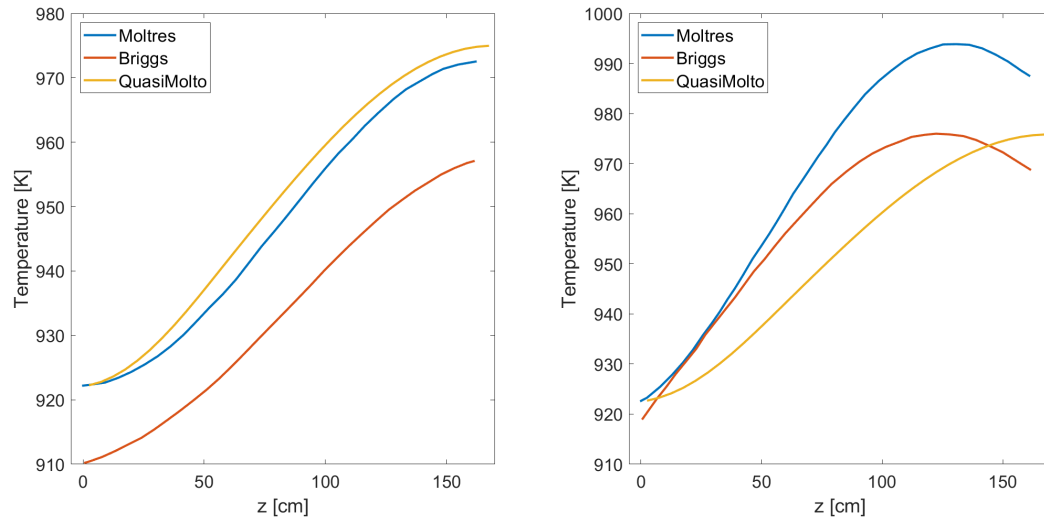


Figure 4.38: Comparison of temperatures in hottest graphite region (right) and closest fuel channel (left).

Hot channel Figure 4.38 shows the temperatures in the hottest graphite channel as calculated by the three different codes. Also plotted is the temperature in the closest fuel channel.

The shape of the temperature distribution in the fuel is similar in each code. All show a ΔT of approximately 55 K across the core. The Moltres and QuasiMolto fuel temperatures compare favorably in magnitude, as well, owing to their similar inlet conditions taken from Robertson [65]. The fuel temperature distribution

calculated by Briggs closely resembles those calculated by Moltres and QuasiMolto, but is offset by approximately 10 K. This appears to be due to a lower inlet temperature.

The moderator temperatures vary significantly. QuasiMolto calculates graphite temperatures nearly identical to the nearby fuel channel, but slightly larger due to gamma and neutron irradiation. Moltres and Briggs both feature prominent peaks in the graphite temperature at approximately 130 cm. This feature is absent in the QuasiMolto result and may be a consequence of the uniform velocity profiles assumed in the nearby fuel channels. Similarly, the lower graphite temperatures calculated by QuasiMolto may be influenced by this assumption. The use of well-developed velocity profiles may result in the peaking behaviour seen in the comparison works. The use of temperature-independent values for the specific heat, density, and thermal conductivity may also contribute to these differences.

It is unclear where the graphite temperatures are taken in the data provided by Briggs; the model described by Haubenreich et al. does not feature distinct graphite regions. The graphite temperatures may have been calculated for a different geometry after calculating the neutron fluxes.

	QuasiMolto	Moltres	Briggs
Peak $\phi_{\text{fast}}/\phi_{\text{thermal}}$	2.754	2.556	3.527

Table 4.33: Midplane peak fast to thermal flux ratios.

Midplane flux Figure 4.39 shows the midplane fluxes calculated by QuasiMolto, Moltres, and Briggs.

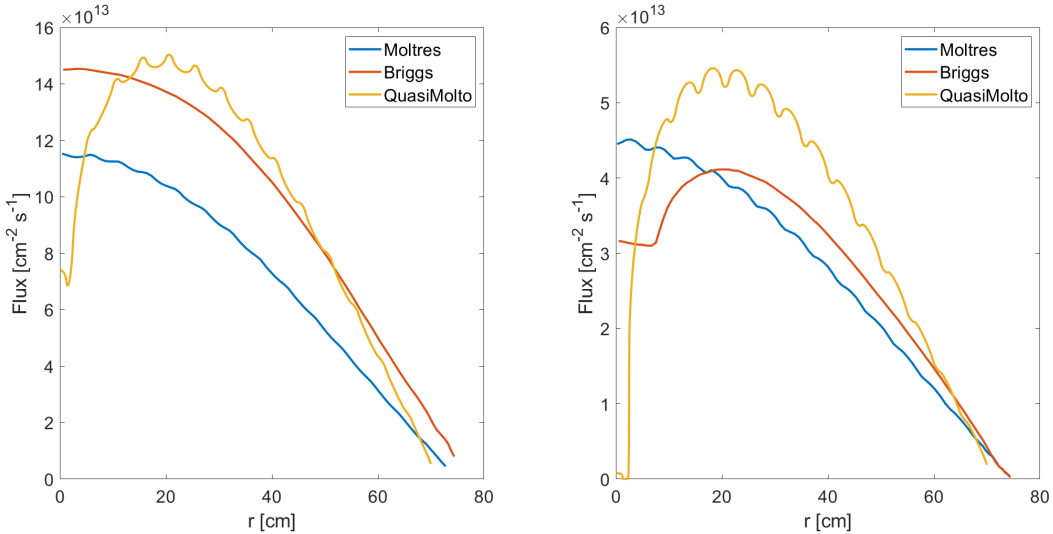


Figure 4.39: Comparison of fast (left) and thermal (right) midplane fluxes

The fast flux as calculated by QuasiMolto has a similar magnitude to that calculated by Briggs and features oscillations reflecting material variation similar to those seen in the Moltres results. These oscillations are absent from Briggs's results as the core is modeled as a homogeneous mixture of fuel and graphite.

QuasiMolto's fast flux drops by a factor of approximately one half in the control rod region around 0 cm. The absence of a depression in Briggs's fast flux may be attributable to the assumed transparency of the control material to fast neutrons, as well as the additional fuel featured around the control rod region. As the Moltres simulation features no control rod, neither the fast nor thermal flux experience a depression near the central axis.

Much of the same observations apply to the thermal flux; magnitudes compare favorably among the three codes, but the control rod has greater effect in

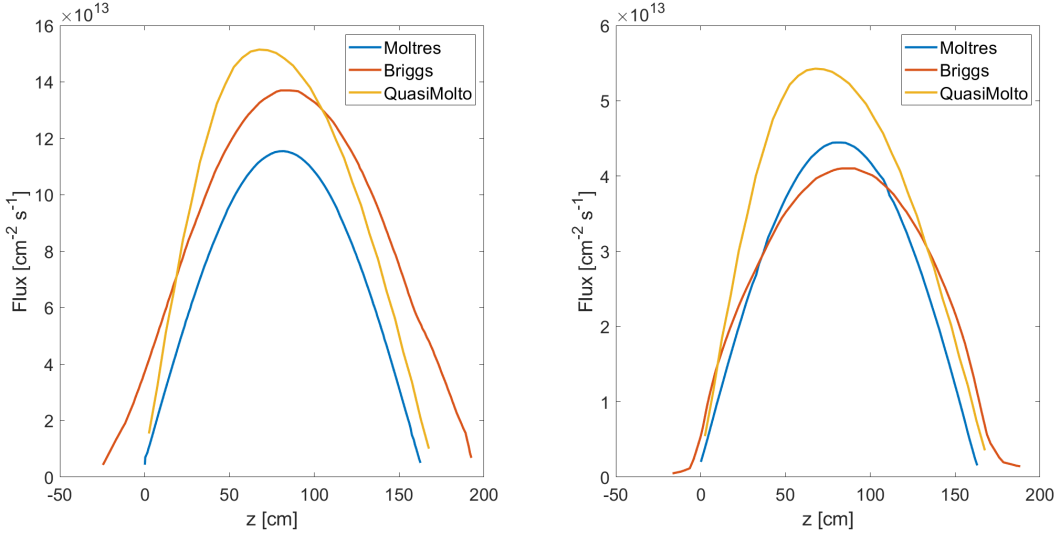


Figure 4.40: Comparison of fast (left) and thermal (right) centerline fluxes.

QuasiMolto. Again, the caveat of additional fuel in the calculations from Briggs is noted, which may contribute to the plateau in the thermal flux observed between 0 cm and 10 cm.

The stronger influence of the control rod in QuasiMolto will drive the group fluxes to increase in order to achieve a power of 10MW. This contributes to the elevated amplitudes of the fluxes calculated by QuasiMolto. Similarly, the larger geometry modeled by Briggs will result in lesser group flux magnitudes.

The peak fast to thermal flux ratios for QuasiMolto and Moltres differ by less than 10%, as detailed in Table 4.33. Note that both of these efforts used the ENDF/B-VII library. Briggs used the nuclear library described by Joanou et al. [75], and the ratio is 30% larger.

	QuasiMolto	Moltres	Briggs
Peak $\phi_{\text{fast}}/\phi_{\text{thermal}}$	2.791	2.598	3.341

Table 4.34: Centerline peak fast to thermal flux ratios.

Centerline flux The centerline fluxes are shown in Figure 4.40. The results from Briggs are taken 21.36 cm from the central axis, presumably to examine a region outside the immediate influence of the control material. For consistency, the results from QuasiMolto are shown at the same location. The results from Moltres, whose model does not feature control material, are taken at 0 cm. Generally, the three sets of results share similar shapes and magnitudes for the fast and thermal fluxes. As Briggs modeled the plena, the associated fluxes span a noticeably greater range.

The fluxes calculated by QuasiMolto are moderately larger than those calculated by Moltres and Briggs. Again, this is likely due to the heightened effects of the control rod in QuasiMolto, which will produce greater group fluxes in order to achieve the rated power.

The centerline peak fast to thermal flux ratios in Table 4.34 demonstrate the same trends noted for the midplane flux ratios in Table 4.33. The QuasiMolto and Moltres values differing by approximately 7%.

Additionally, the QuasiMolto fluxes are noticeably biased towards the bottom of the reactor. This is evidence of negative temperature feedback in the system and consistent with the fuel temperature distributions in Figure 4.38. The control material may also be contributing to the asymmetry. This bias is not obviously present in the comparison works. If the calculations by Briggs, however, did utilize indirect thermal-hydraulic coupling, one may not expect to observe evidence of

temperature feedback in the fluxes. The use of differing nuclear data amongst the three works may also contribute to this variation.

4.4.5 Transport effects

A number of the calculations in the previous sections were repeated while enforcing Eddington factors and boundary conditions consistent with the P1 (or diffusion) approximation. By examining the differences between the original transport-coupled solutions and these diffusion solutions, the importance of capturing transport effects in the modeled problems was assessed.

$$\text{Diffusion Eddington factors: } (E_{zz}, E_{rr}, E_{rz}) = \left(\frac{1}{3}, \frac{1}{3}, 0 \right). \quad (4.33)$$

The P1 boundary conditions are described in Appendix E. In the sections that follow, a parameter calculated using MGHOT-derived Eddington factors is labeled ‘transport’, and a parameter calculated with the Eddington factors in Eq. (4.33) is labeled ‘diffusion’.

4.4.5.1 Isothermal eigenvalue

The isothermal eigenvalue calculation was repeated assuming the diffusion approximation. The absolute difference of the Eddington factors calculated with the MGHOT solution and their diffusion equivalents are presented in Figures 4.41, 4.42, and 4.43.

Areas where the deviations are non-zero indicate the presence and magnitude of transport effects. Figures 4.41 and 4.42 show higher deviations in E_{zz} and E_{rr} in the fuel channels and near boundaries, where transport effects are expected. Note that the peak deviations in Figures 4.41 and 4.42 occur at the outside boundaries. E_{zz} and E_{rr} also exhibit oscillatory behaviours close to the axial boundaries. Figure 4.43 shows higher deviations in E_{rz} at the interfaces between materials, deviations which grow more pronounced towards the outside boundary, particularly at the outside corners.

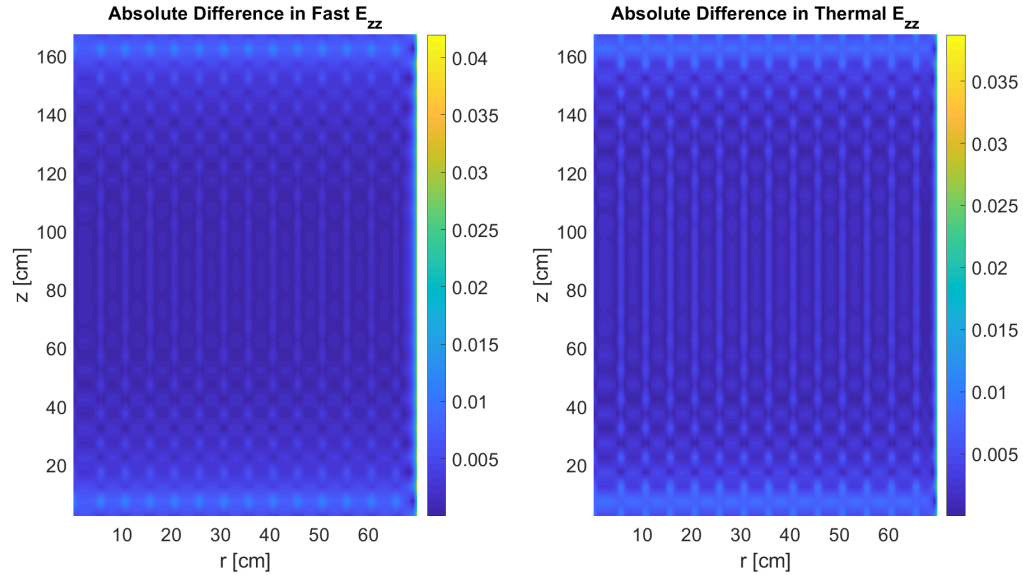


Figure 4.41: Absolute difference in fast and thermal E_{zz} for isothermal calculation.

The percent difference between the transport and diffusion fluxes is shown in Figure 4.44. The flux variations largely follow the patterns present in the figures of the Eddington factors. In fuel regions, the diffusion approximation generally underestimates the fast flux and overestimates the thermal flux. The converse is

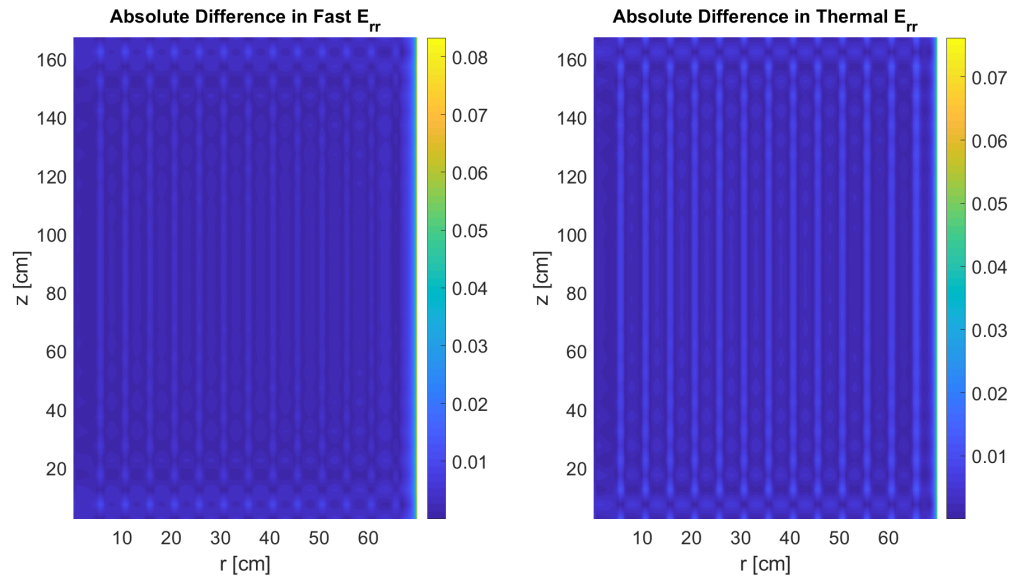


Figure 4.42: Absolute difference in fast and thermal E_{rr} for isothermal calculation.

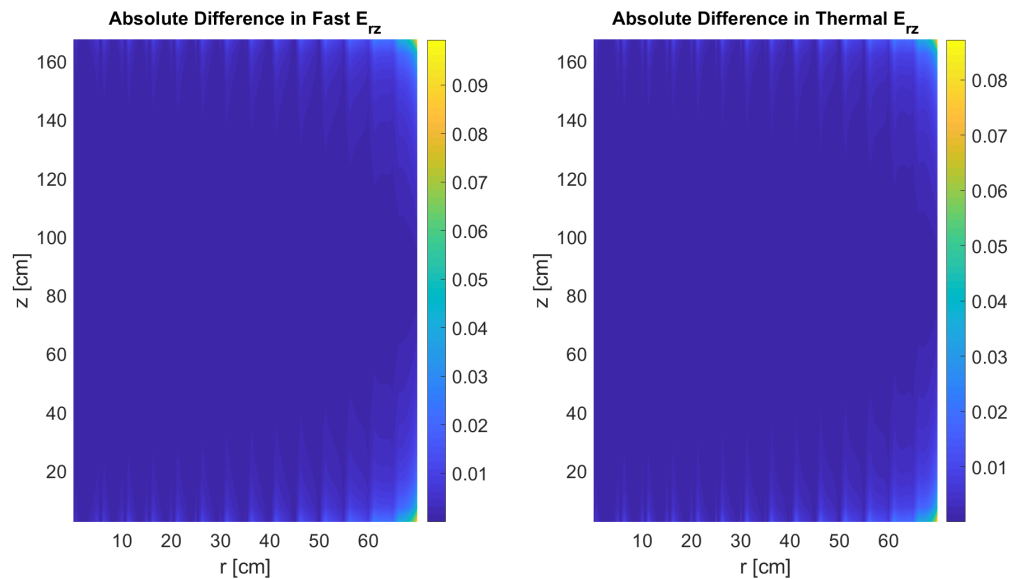


Figure 4.43: Absolute difference in fast and thermal E_{rz} for isothermal calculation.

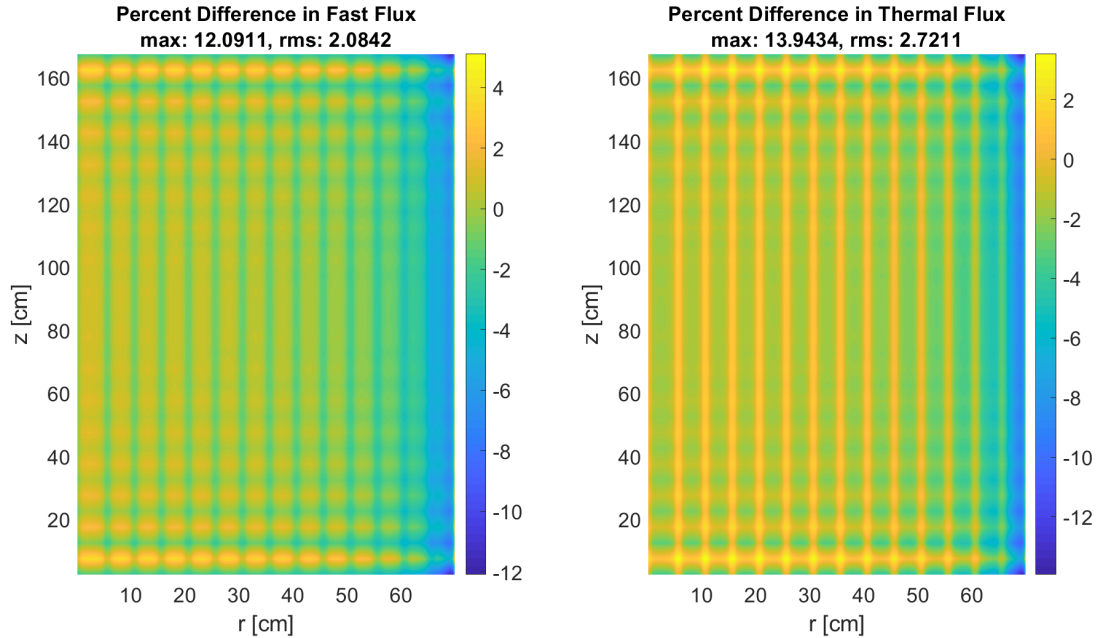


Figure 4.44: Percent difference in isothermal fast and thermal fluxes relative to case with transport coupling.

true in graphite regions. Artifacts of the oscillations noted in the Eddington factors appear in the form of the checkering at the axial boundaries.

The largest differences in the fast and thermal fluxes occur at the outside boundary, where the diffusion approximation underestimates the fluxes by as much as 14%. On average, the differences are around 2% and 3% for the fast and thermal fluxes, respectively.

The difference between the transport and diffusion eigenvalue, detailed in Table 4.35, was approximately 0.1%.

Table 4.35: Isothermal eigenvalues calculated for transport and diffusion simulations.

	Transport	Diffusion	Difference*10⁵
k_{eff}	1.05852	1.05747	105

4.4.5.2 Loss of reactivity from DNP flow

The effects of the diffusion approximation on the temperature distribution, DNP concentrations, and reactivity loss from DNP flow were examined by repeating the calculations in Section 4.4.2. The transport-derived Eddington factors for the original calculations were nearly identical to those detailed in the previous section. Similarly, the variations in the transport and diffusion fluxes were nearly identical to those presented in Figure 4.44.

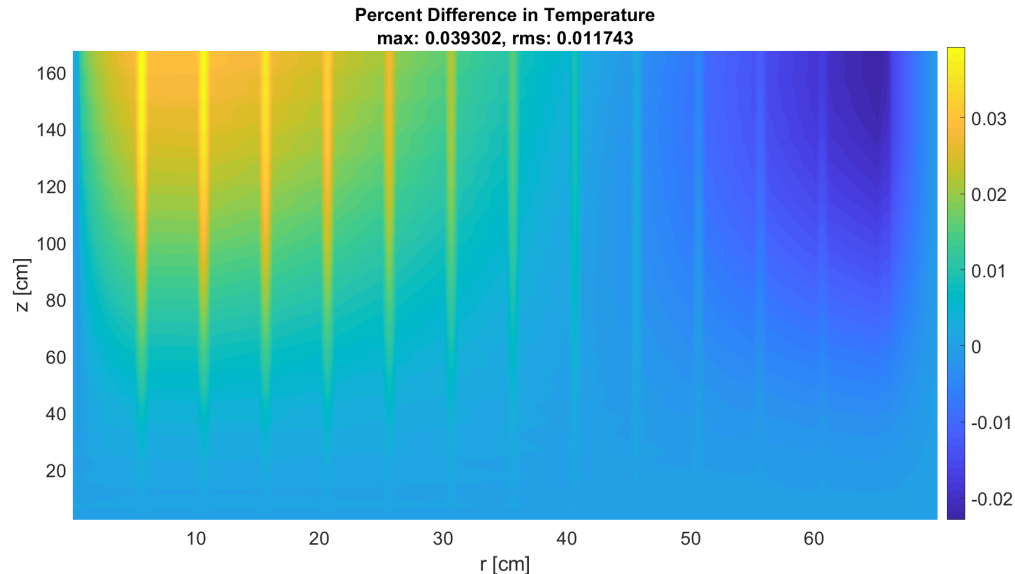


Figure 4.45: Percent difference in temperature distribution relative to case with transport coupling.

The change in the temperature distribution brought on by the use of diffusion Eddington factors was minimal, as shown in Figure 4.45. The temperature distribution is driven by fission events, which are driven predominantly by the thermal flux. As such, the variations in the thermal flux in the fuel channels of Figure 4.44 are reflected in Figure 4.45; the temperatures are higher towards the center of the core and lower towards the outside. At the inlet of the core, where the boundary temperature is fixed, the variation is close to zero. At the outlet, the maximum temperature variation of approximately 0.04% is seen in the fuel channel at 5 cm.

On average, the DNP concentrations varied by just over half a percent, as shown in Figure 4.46, 4.47, and 4.48. Data in these figures were calculated with ENDF decay data. Similar to the temperature distribution, higher thermal fluxes in the inside fuel channels produced higher DNP concentrations, while lower thermal fluxes produced lower DNP concentrations in outside fuel channels. Maximum variations around 5% were observed for all precursor groups, however, variations of this magnitude were limited to fuel channels in areas of lower importance near the outside boundary.

The reactivity losses from DNP drift for the diffusion case, detailed in Table 4.36, are nearly identical to those for the transport case detailed in Table 4.28.

Table 4.36: Reactivity loss from DNP drift using the P1 approximation. The change in reactivity $\Delta\rho$ is measured relative to the system with $\beta = 0$.

Decay data	k_{eff}	ρ [pcm]	$\Delta\rho$ [pcm]
$\beta = 0$	1.058114	5492.22	—
ENDF	1.054522	5170.3	-321.92
ORNL	1.054863	5200.96	-291.26

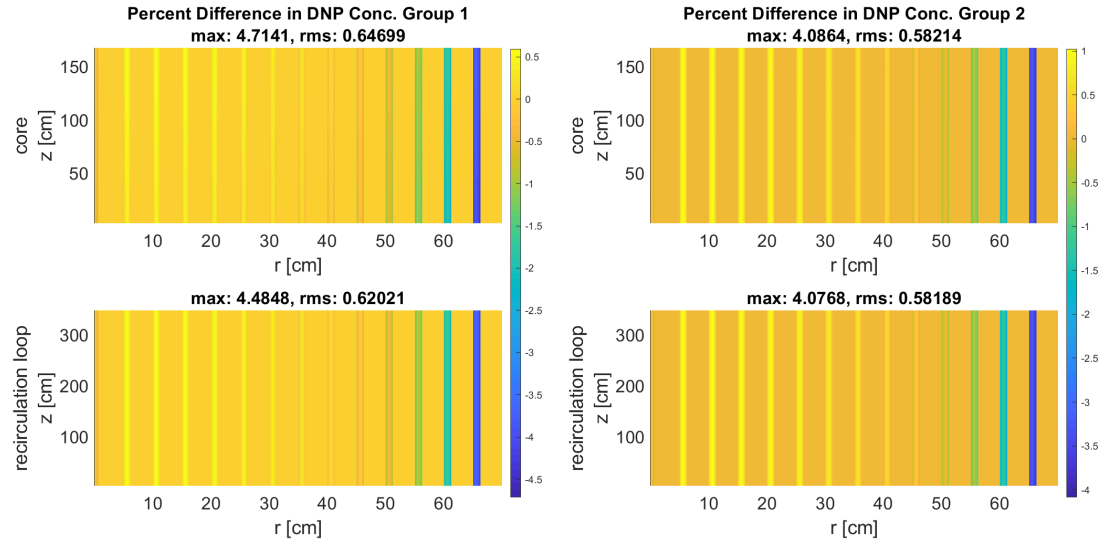


Figure 4.46: Percent difference in DNP concentrations for groups 1 and 2 relative to case with transport coupling.

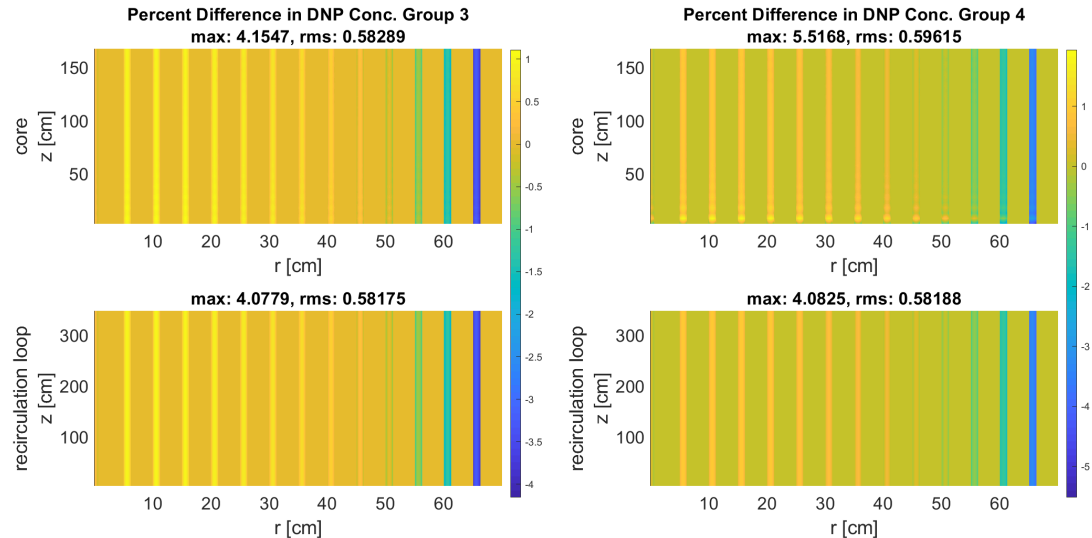


Figure 4.47: Percent difference in DNP concentrations for groups 3 and 4 relative to case with transport coupling.

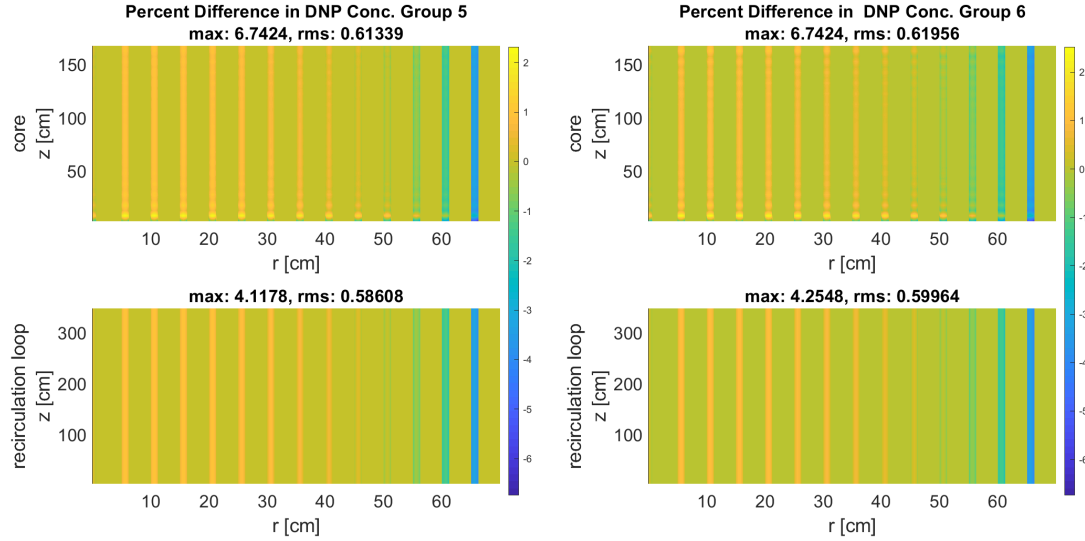


Figure 4.48: Percent difference in DNP concentrations for groups 5 and 6 relative to case with transport coupling.

4.4.5.3 Critical system

The approximately critical reactor configuration was also simulated with the diffusion approximation. The absolute difference of the Eddington factors calculated with the MGHOT solution and their diffusion equivalents are presented in Figures 4.49, 4.50, and 4.51.

For the bulk of the core, the Eddington factors for the critical configuration look similar to those reported for the isothermal case in Figures 4.41, 4.42, and 4.43. Higher deviations from the diffusion values occur within the fuel channels, near boundaries, and at material interfaces. The presence of the partially inserted control rod at approximately 2.5 cm from the central axis, however, sets these results apart. In this region, the deviations increase significantly, particularly in

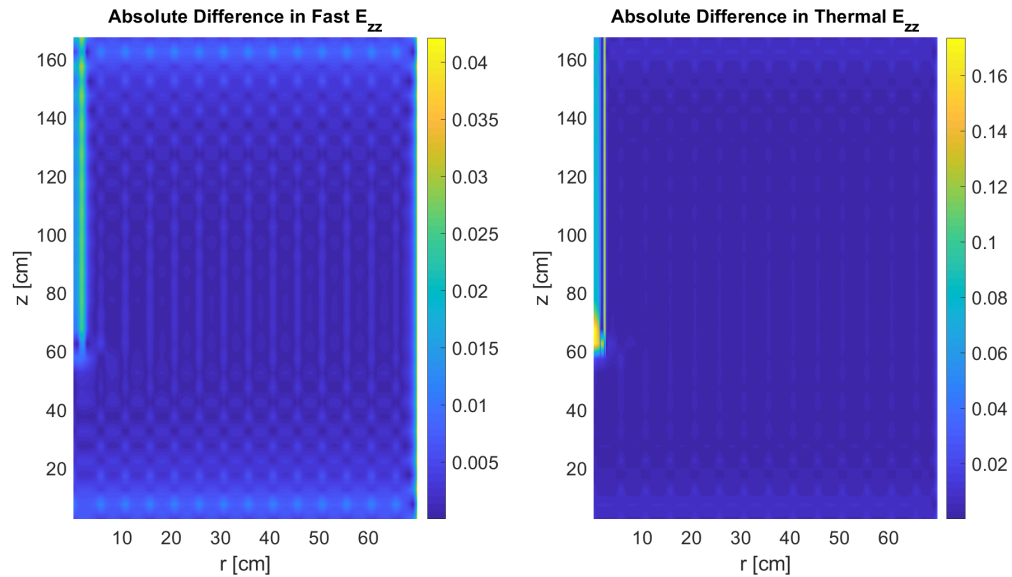


Figure 4.49: Absolute difference in fast and thermal E_{zz} for critical configuration.

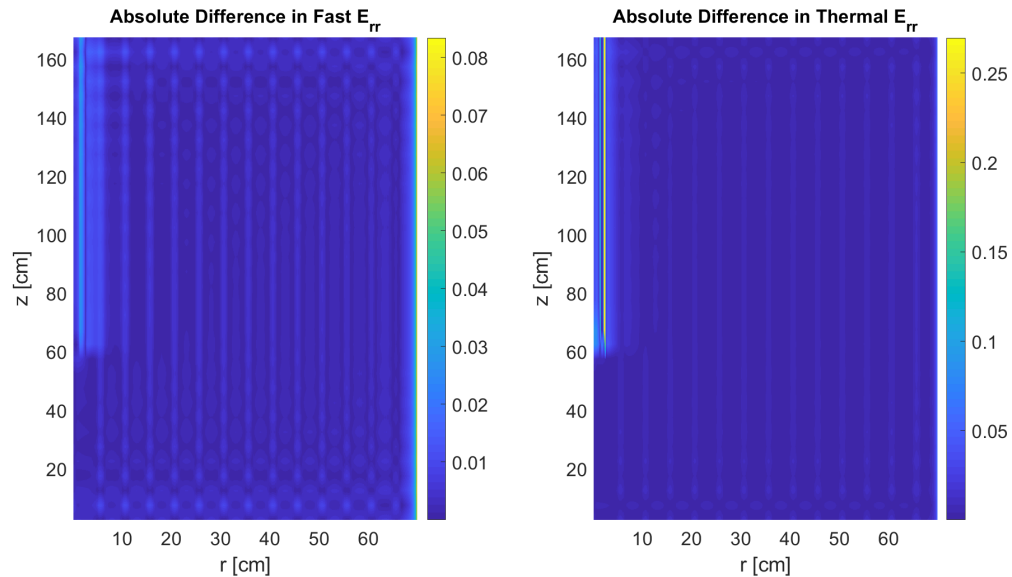


Figure 4.50: Absolute difference in fast and thermal E_{rr} for critical configuration.

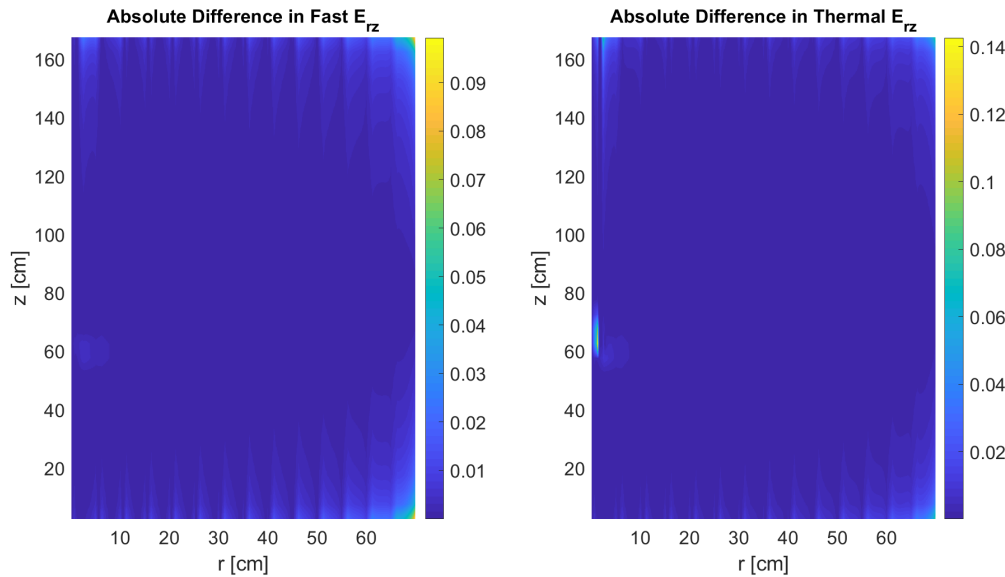


Figure 4.51: Absolute difference in fast and thermal E_{rz} for critical configuration.

the thermal energy group where the control material is particularly absorptive. As expected, the fluxes calculated with diffusion approximation differ significantly from the transport solution in and around the control rod region, as shown in Figure 4.52.

The diffusion approximation calculates a higher fast flux in the control rod, and a lower fast flux in neighboring regions. The thermal fluxes in the control rod shows more nuanced variations that are shown in the left plot of Figure 4.53. On the outside edge, the flux is overestimated by roughly 20%. In the region just inside this edge, the flux is underestimated by over 30% before rebounding to an overestimation of roughly 10%. This general behaviour is mirrored on the inside edge, but with lesser magnitudes. The right plot of Figure 4.53 shows that the depression in the transport thermal flux around the control material is

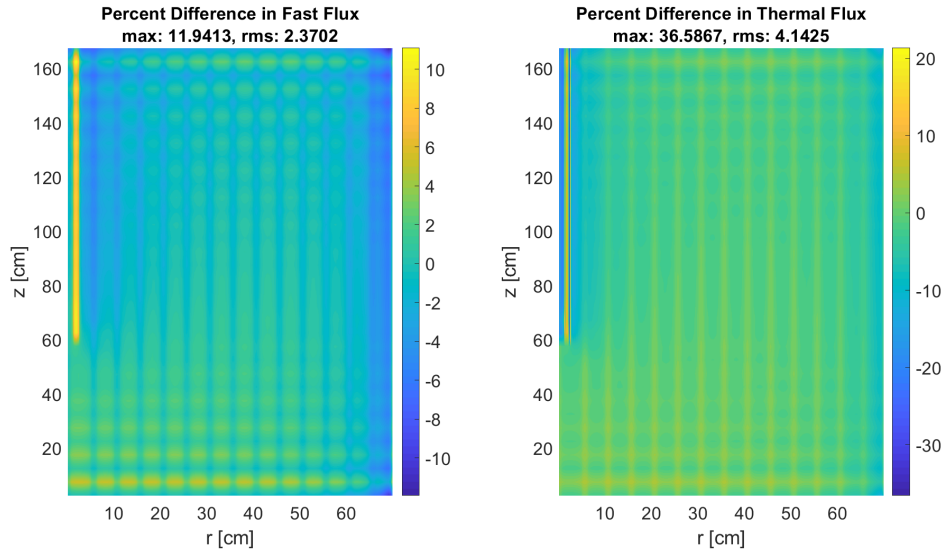


Figure 4.52: Percent difference in fast and thermal fluxes relative to case with transport coupling for critical configuration.

slightly broader and deeper than in the diffusion case, giving rise to the differences observed.

Outside the control rod region, as before, lesser fast fluxes and greater thermal fluxes are observed in the fuel channels while the converse is true in the graphite regions. The RMS average variation for the fast and thermal fluxes were modestly larger than those reported for the isothermal case at approximately 2.5% and 4.7%, respectively.

A comparison of the midplane and centerline fluxes is shown in Figure 4.54. The centerline fast and thermal fluxes are in close agreement for both cases. The midplane fast and thermal fluxes have the same rough shape, but the transport fluxes exhibit, generally, greater fluxes in the fuel channels and lesser fluxes in the graphite moderator. Overall, Figure 4.54 shows that the diffusion approxima-

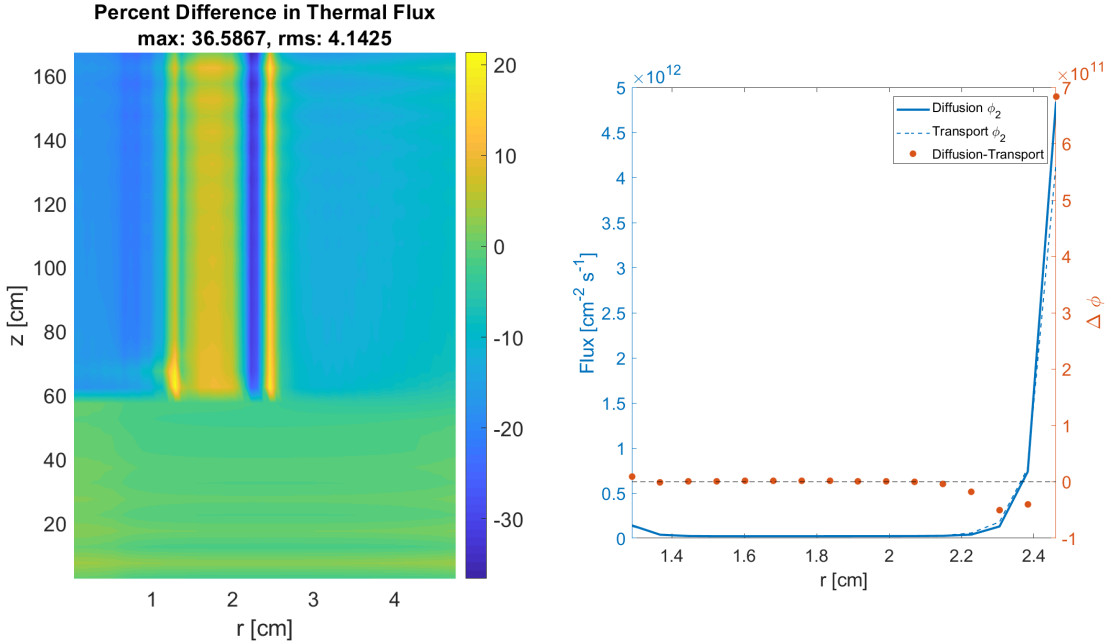


Figure 4.53: Left: percent difference in thermal flux around control rod for critical configuration. Right: thermal fluxes around control rod at core midplane.

tion replicates the general features of the transport solution, but finer details are smoothed out.

Table 4.37: Eigenvalues of transport and diffusion simulations for approximately critical case.

	Transport	Diffusion	Difference* 10^5
k_{eff}	0.99471	0.98824	647

The difference in eigenvalue, detailed in Table 4.37, is greater than for the isothermal case at roughly 0.6%. As the critical configuration introduces control material and accompanying transport effects, which the diffusion approximation cannot capture, this heightened difference is expected. The depressed fluxes in areas neighboring the control rod are most likely responsible for the lesser eigenvalue

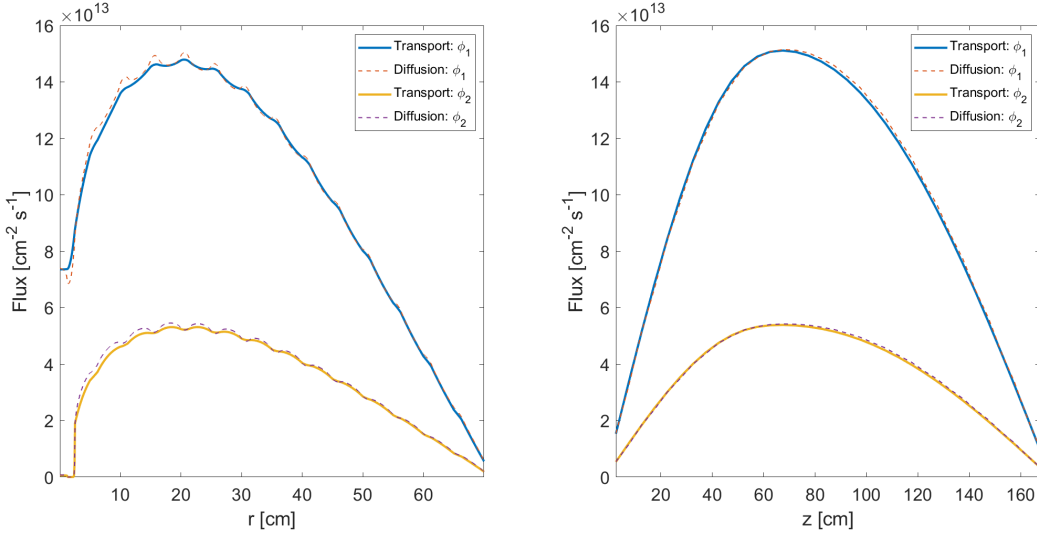


Figure 4.54: Midplane (left) and centerline (right) fluxes as calculated with diffusion and transport-derived Eddington factors and boundary conditions.

found in the diffusion case.

4.4.6 Remarks

Considering modeling differences, the isothermal eigenvalue calculation and intercode comparison of the centerline and midplane fluxes reflected QuasiMolto's ability to accurately capture the neutronic aspects of MSRE. This ability would be further enhanced by better representation of the multiphysics phenomena.

QuasiMolto was found to overestimate the loss of reactivity from DNP flow. Additionally, QuasiMolto was unable to reproduce the shape and magnitude of the graphite temperature distribution calculated by other codes, although the fuel temperature distribution was comparable. The use of temperature-dependent thermal

physical properties may partially address these irregularities. Coupling to additional multiphysics phenomena, such as equations describing fluid flow, also offers promise. Here, one merit of the multilevel approach can be highlighted: additional coupling need only be considered at the ELOT level, and not in any multigroup context.

Under normal operating conditions, transport effects were found to be responsible for an average variation of 2-3% in the group fluxes, which may be significant for depletion calculations. Insertion of strong absorbing material was found to produce larger average variations of 2-5%. Impacts to the temperature distribution and DNP concentrations were minor.

Generally, the diffusion approximation was found to adequately calculate the neutronic characteristics of the MSRE. Note, however, that the modeling of transport phenomena did not unduly increase solution time. As noted in Section 4.2, the MGHOT solution is computationally inexpensive relative to the cost of solutions at the MGLOQD and ELOT levels.

5 Conclusion

The objectives of this research are restated below:

1. Model and simulate time- and space-dependent CFR physics using neutron transport theory
 - (a) Implement in RZ cylindrical geometry
 - (b) Implement for an arbitrary number of neutron energy and precursor groups
2. Implement multiphysics coupling using a quasi-diffusion based, multilevel method
3. Validate results against available experimental data from the MSRE

Objective 1(a) was met by use of the multilevel method developed in this work. From the solution of the multigroup neutron transport equation, high-order transport effects in each energy group are projected into a multigroup low-order quasi-diffusion system through the use of fractional functionals, such as the Eddington factors. The solution to the multigroup low-order system is used in group collapse calculations to further project transport effects into the formulation of a compact single-group low-order quasi-diffusion system whose solution preserves multigroup reaction rates.

The low-order system also includes the multiphysics phenomena, satisfying Objective 2. The delayed neutron precursor balance equations feature an advection term to account for the drift phenomenon which characterizes circulating fuel reactor physics. Coupling to the heat transfer equation allows for temperature dependence of the group constants. Enforcing multiphysics coupling to the single-group quasi-diffusion system offers computational savings relative to a multigroup alternative, while also simplifying future coupling to additional multiphysics phenomena. Explicit methods, which introduce stability conditions, were used to approximate the advection terms and purely axial velocities were assumed.

The novel method was implemented in the computational tool QuasiMolto for an arbitrary number of neutron energy groups and precursor groups, in satisfaction of Objective 1(b). The implemented solvers were verified with the method of manufactured solutions, and the low-order solvers were found to exhibit second- and first-order convergence with respect to space and time for smooth solutions.

A multilevel residual balance algorithm intended to reduce oversolving was presented and, when characterized by balance factors allowing for tight coupling between the levels, was found to reduce the computational cost of a solve by a factor of approximately three when compared to fixed point iteration.

Transient and steady-state calculations demonstrated the influence of the delayed neutron precursor drift phenomenon, and simulations of the MSRE, the subject of Objective 3, were found to reproduce much of the neutronic behaviour found with other computational tools. Enhanced multiphysics coupling would facilitate modeling improvements, which in turn would allow QuasiMolto to better

reproduce key experimental characteristics such as the loss of reactivity due to delayed neutron precursor drift and the graphite temperature distribution.

Leveraging the flexibility of the multilevel framework, the influence of transport effects on channel-type reactors was examined by enforcing Eddington factors and boundary conditions consistent with the P_1 approximation. The resulting calculations were compared to those incorporating transport effects, and average variations of 2-3% were found in the two-group fluxes under normal-operating conditions. Overall, the P_1 approximation reproduced the general features of the transport solution on the problems considered.

5.1 Future work

As mentioned, coupling to additional multiphysics phenomena would improve QuasiMolto's agreement to experimental and computed quantities. In particular, results suggest direct or indirect coupling to equations governing fluid flow hold the most promise, and would also enable the simulation of transients characterized by natural circulation or channel blockage. Transient simulations would also benefit from the scalability offered by the use of an advanced, high-performance computational library such as PETSc [61] or hypre [62]. Additionally, the use of implicit discretizations for the advection terms present in the multiphysics equations would eliminate the stability conditions noted earlier, allowing for refinements in the spatial mesh of transient simulations without requiring a proportional refinement to the temporal mesh.

Near the conclusion of this work, it was noted that definitions offering greater consistency with the neutron transport solution are applicable to the Eddington factors at cell interfaces. These alternate definitions would incorporate the upwinding convention used in the simple corner balance approach, rather than utilizing the volume-averaged angular fluxes. The volume-averaged definitions may introduce diffusive effects that the upwind definitions avoid.

Finally, two recently published benchmarks, one on the MSRE by Fratoni et al. [76] and another on molten salt fast reactors by Tiberga et al. [77], offer further opportunities to assess the capabilities implemented in QuasiMolto.

Bibliography

- [1] J. Serp et al. “The molten salt reactor (MSR) in generation IV: Overview and perspectives”. In: *Progress in Nuclear Energy* 77 (2014), pp. 308–319.
- [2] W. K. Ergen et al. “The Aircraft Reactor Experiment-Physics”. In: *Nuclear Science and Engineering* 2 (1957), pp. 826–840.
- [3] A. Weinberg. “The First Nuclear Era: The Life and Times of a Technological Fixer”. In: AIP Press, 1994. Chap. Aircraft Nuclear Propulsion.
- [4] E. S. Bettis et al. “The Aircraft Reactor Experiment-Design and Construction”. In: *Nuclear Science and Engineering* 2 (1957), pp. 804–825.
- [5] E. S. Bettis et al. “The Aircraft Reactor Experiment-Operation”. In: *Nuclear Science and Engineering* 2 (1957), pp. 841–853.
- [6] H. G. MacPherson. “The Molten Salt Reactor Adventure”. In: *Nuclear Science and Engineering* 90:4 (1985), pp. 374–380.
- [7] N. Haubenreich P and J. R. Engel. “Experience with the Molten-Salt Reactor Experiment”. In: *Nuclear Applications and Technology* 8 (1970), pp. 118–136.
- [8] J. R. Engel et al. *Conceptual Design Characteristics of a Denatured Molten-Salt Reactor with Once-Through Fueling*. Tech. rep. ORNL/TM-7207. Oak Ridge National Laboratory, July 1980.

- [9] R. C. Robertson. *Conceptual Design Study of a Single-Fluid Molten-Salt Breeder Reactor*. Tech. rep. ORNL-4541. Oak Ridge National Laboratory, June 1971.
- [10] J. E. Kelly. “Generation IV International Forum: A decade of progress through international cooperation”. In: *Progress in Nuclear Energy* 77 (2014), pp. 240–246.
- [11] H. Freed et al. *Advanced Nuclear 101*. Ed. by thirdway.org. [Online; posted 01-December-2015]. Dec. 2015. URL: <https://www.thirdway.org/report/advanced-nuclear-101>.
- [12] T. Abram and S. Ion. “Generation-IV nuclear power: A review of the state of the science”. In: *Energy Policy* 36 (2008), pp. 4323–4330.
- [13] D. F. Williams and P. F. Britt. *Technology and Applied R&D Needs for Molten Salt Chemistry: Innovative Approaches to Accelerate Molten Salt Reactor Development and Deployment*. Tech. rep. U.S. Department of Energy, Apr. 2017.
- [14] D. Wooten and J. J. Powers. “A Review of Molten Salt Reactor Kinetics Methods”. In: *Nuclear Science and Engineering* 191 (2018), pp. 203–230.
- [15] J. J. Duderstadt and L. J. Hamilton. *Nuclear Reactor Analysis*. Wiley, 1976.
- [16] R. J. Kedl. *Fluid Dynamic Studies of the Molten Salt Reactor Experiment Core*. Tech. rep. ORNL/TM-3229. Oak Ridge National Laboratory, Nov. 1970.

- [17] M. Delpech et al. “Benchmark of dynamic simulation tools for molten salt reactors”. In: *Global 2003: Atoms for Prosperity: Updating Eisenhowers Global Vision for Nuclear Energy* (Nov. 2003).
- [18] Apil Tamang and Dmitriy Y. Anistratov. “A Multilevel Projective Method for Solving the Space-Time Multigroup Neutron Kinetics Equations Coupled with the Heat Transfer Equation”. In: *Nuclear Science and Engineering* 177 (2014), pp. 34–89.
- [19] D. Lecarpentier and V. Carpentier. “A Neutronic Program for Critical and Nonequilibrium Study of Mobile Fuel Reactors: The Cinsf1D Code”. In: *Nuclear Science and Engineering* 143 (2003), pp. 33–46.
- [20] T. Yamamoto et al. “Transient Characteristics of Small Molten Salt Reactor During Blockage Accident”. In: *Heat Transfer - Asian Research* 143 (2006), 35 (6).
- [21] J. Krepel et al. “DYN1D-MSR dynamics code for molten salt reactors”. In: *Annals of Nuclear Energy* 32 (2005), pp. 1799–1824.
- [22] J. Krepel et al. “DYN3D-MSR spatial dynamics code for molten salt reactors”. In: *Annals of Nuclear Energy* 34 (2007), pp. 449–462.
- [23] U. Rohde et al. “The reactor dynamics code DYN3D – models, validation and applications”. In: *Progress of Nuclear Energy* 89 (2016), pp. 170–190.
- [24] B. E. Prince et al. *Zero-power physical experiments on molten-salt reactor experiment*. Tech. rep. ORNL-4233. Oak Ridge National Laboratory, 1968.

- [25] C. Nicolino et al. “Coupled dynamics in the physics of molten salt reactors”. In: *Annals of Nuclear Energy* 35 (2008), pp. 314–322.
- [26] D. L. Zhang et al. “Development of a steady state analysis code for a molten salt reactor”. In: *Annals of Nuclear Energy* 36 (2009), pp. 590–603.
- [27] J. Kópházi, D. Lathouwers, and J. L. Kloosterman. “Development of a Three-Dimensional Time-Dependent Calculation Scheme for Molten Salt Reactors and Validation of the Measurement Data of the Molten Salt Reactor Experiment”. In: *Nuclear Science and Energy* 163 (2009), pp. 118–131.
- [28] B. Boer et al. “Coupled Neutronics/Thermal-Hydraulics Calculations for High Temperature Reactors with the DALTON-THERMIX Code System”. In: *Proceedings of the International Conference on Physics of Reactors (PHYSOR ‘08)*. Interlaken, Switzerland, 2008.
- [29] M. Aufiero et al. “Development of an OpenFOAM model for the Molten Salt Fast Reactor transient analysis”. In: *Chemical Engineering Science* 111 (2014), pp. 390–401.
- [30] H. Jasak, A. Jemcov, and Z. Tukovic. “OpenFOAM: a C++ library for Complex Physics Simulations”. In: *International Workshop ON Coupled Methods in Numerical Dynamics*. 2007.
- [31] C. Fiorina et al. “Modelling and analysis of the MSFR transient behaviour”. In: *Annals of Nuclear Energy* 64 (2014), pp. 485–498.
- [32] COMSOL Multiphysics. *AC/DC Module User’s Guide*. 5.4. Stockholm, Sweden: COMSOL AB ®, 2018, pp. 75–84.

- [33] K. Zhuang et al. “Studies on the molten salt reactor: code development and neutronic analysis of MSRE-type design”. In: *Journal of Nuclear Science and Technology* 52 (2015), pp. 251–263.
- [34] A. Lindsay et al. “Introduction to Moltres: An application for simulation of Molten Salt Reactors”. In: *Annals of Nuclear Energy* 114 (2018), pp. 530–540.
- [35] D. Gaston et al. “MOOSE: A parallel computational framework for coupled systems of nonlinear equations”. In: *Nuclear Engineering and Design* 239 (May 2009), pp. 1768–1778.
- [36] V. Ya. Gol'din. “A Quasi-Diffusion Method of Solving the Kinetic Equation”. In: *USSR Computational Mathematics and Mathematical Physics* 4 (1964), pp. 136–149.
- [37] V. Ya. Gol'Din. “On Mathematical Modeling of Problems of Non-Equilibrium Transfer in Physical Systems”. In: *Modern Problems of Mathematical Physics and Computational Mathematics*. Nauka, Moscow, 1982, pp. 113–127.
- [38] V. Ya. Gol'Din. “Solution of the Multigroup Transport Equation by the Quasi-Diffusion Method”. In: *Preprint of the Keldysh Institute for Applied Mathematics* 128, USSR Academy of Sciences (1986).
- [39] D. Y. Anistratov and V. Ya. Gol'Din. “Numerical Solution of the Time-Dependent Transport Equation Coupled with the Burnup and Reactor Kinetics Equations”. In: *Proceedings of the International Symposium for Numerical Transport Theory*. Moscow, Russia, 1992, p. 33.

- [40] V. Ya. Gol'Din and D. Y. Anistratov. "Fast Neutron Reactor in a Self-Adjusting Neutron-Nuclide Regime". In: *Mathematical Modeling* 7.10 (1995), pp. 12–32.
- [41] V. Ya. Gol'Din and B. N. Chetverushkin. "Methods for Solving One-Dimensional Problems of Radiation Gas Dynamics". In: *USSR Computational Mathematics and Mathematical Physics* 12 (1972), pp. 177–189.
- [42] V. Ya. Gol'Din, D. A. Gol'Dina, et al. "Mathematical Modeling of High Temperature Gas Dynamics Processes". In: *Problems of Atomic Science and Engineering: Methods and Codes for Numerical Solution of Mathematical Physics Problems* 2 (1986).
- [43] D. Y. Anistratov, E.N Aristova, and V. Ya. Gol'Din. "A Nonlinear Method for Solving Problems of Radiation Transfer in Medium". In: *Mathematical Modeling* 7.10 (1996), p. 3.
- [44] E. N. Aristova, V. Ya. Gol'Din, and A. V. Kolpakov. "Multidimensional Calculations of Radiation Transport by Nonlinear Quasi-Diffusion Method". In: *Proceedings of the International Conference on Mathematics and Computations, Reactor Physics and Environmental Analysis in Nuclear Applications*. Madrid, Spain, 1986, p. 667.
- [45] E. N. Aristova. "Simulation of Radiation Transport in a Channel Based on the Quasi-Diffusion Method". In: *Transport Theory and Statistical Physics* 37 (2008), pp. 483–503.

- [46] A. Cammi et al. "A multi-physics modelling approach to the dynamics of Molten Salt Reactors". In: *Annals of Nuclear Energy* 38 (2011), pp. 1356–1372.
- [47] E. E. Lewis and Jr. W. F. Miller. *Computational Methods of Neutron Transport*. American Nuclear Society, 1993.
- [48] G. I. Bell and S. Glasstone. "Nuclear Reactor Theory". In: (Oct. 1970).
- [49] J. E. Morel and G.R. Montry. "Analysis and elimination of the discrete-ordinates flux dip". In: *Transport Theory and Statistical Physics* 13.5 (1984), pp. 615–633.
- [50] M. L. Adams. "Subcell balance methods for radiative transfer on arbitrary grids". In: *Transport Theory and Statistical Physics* 26.2-5 (1997), pp. 385–431.
- [51] T. S. Palmer and M. L. Adams. "Curvilinear Geometry Transport Discretizations in the "Thick" Diffusion Limit". In: *Proceedings of International Topical Meeting on Mathematical Methods and Supercomputing in Nuclear Applications*. Karlsruhe, Germany, 1993.
- [52] Marvin L. Adams and Edward W. Larsen. "Fast Iterative Methods for Discrete-Ordinates Particle Transport Calculations". In: *Progress in Nuclear Energy* 40 (2002), pp. 3–159.
- [53] J.P. Jones, D.Y. Anistratov, and J. E. Morel. "Discretization of Low-Order Quasidiffusion Equations on Arbitrary Quadrilaterals in 2D r-z Geometry". In: *Proceedings of M&C 2017*. Jeju, Korea, 2017.

- [54] J. E. Morel. *A 3-D cell-centered diffusion discretization for arbitrary polynomial meshes*. Tech. rep. LANL Research Note, CCS-4:02-40(U). Los Alamos National Laboratory, 2002.
- [55] J.P. Jones. “The Quasidiffusion Method For Solving Radiation Transport Problems On Arbitrary Quadrilateral Meshes in 2D $r - z$ Geometry”. PhD thesis. North Carolina State University, 2019.
- [56] Randall J. Leveque. “Finite Volume Methods for Hyperbolic Problems”. In: Cambridge UK: Cambridge University Press, 2004. Chap. 4, pp. 72–76.
- [57] J. E. Morel, R. M. Roberts, and M. J. Shashkov. “A Local Support-Operators Diffusion Discretization Scheme for Quadrilateral $r - z$ Meshes”. In: *Journal of Computational Physics* 144 (1997), pp. 17–51.
- [58] Randall J. Leveque. “Finite Difference Methods for Ordinary and Partial Differential Equations”. In: Philadelphia, PA: Society for Industrial and Applied Mathematics, 2007. Chap. 3, pp. 66–68.
- [59] J. P. Senecal and W. Ji. “Approaches for mitigating over-solving in multi-physics simulations”. In: *Annals of Nuclear Energy* 112 (2017), pp. 503–528.
- [60] Gaël Guennebaud, Benoît Jacob, et al. *Eigen v3*. <http://eigen.tuxfamily.org>. 2010.
- [61] Satish Balay et al. *PETSc Web page*. <https://www.mcs.anl.gov/petsc>. 2019. URL: <https://www.mcs.anl.gov/petsc>.

- [62] Robert D. Falgout and Ulrike Meier Yang. “hypre: A Library of High Performance Preconditioners”. In: *Computational Science — ICCS 2002*. Ed. by Peter M. A. Sloot et al. Berlin, Heidelberg: Springer Berlin Heidelberg, 2002, pp. 632–641. ISBN: 978-3-540-47789-1.
- [63] Kambiz Salari and Patrick Knupp. “Code Verification by the Method of Manufactured Solutions”. In: Sandia National Laboratories, June 2000. Chap. 3, pp. 21–27.
- [64] P. N. Haubenreich et al. *MSRE Design and Operations Report. Part III. Nuclear Analysis*. Tech. rep. ORNL-TM-730. Oak Ridge National Laboratory, 1964.
- [65] R. C. Robertson. *MSRE Design and Operations Report. Part I. Description of Reactor Design Technical Report*. Tech. rep. ORNL-TM-728. Oak Ridge National Laboratory, 1965.
- [66] G. M. Tolson and A. Taboada. *MSRE CONTROL ELEMENTS: Manufacture, Inspections, Drawings, and Specifications*. Tech. rep. ORNL-4123. Oak Ridge National Laboratory, 1967.
- [67] “ENDF/B-VII.1 Nuclear Data for Science and Technology: Cross Sections, Covariances, Fission Product Yields and Decay Data”. In: *Nuclear Data Sheets* 112.12 (2011). Special Issue on ENDF/B-VII.1 Library, pp. 2887–2996. ISSN: 0090-3752. DOI: <https://doi.org/10.1016/j.nds.2011.11.002>. URL: <http://www.sciencedirect.com/science/article/pii/S009037521100113X>.

- [68] J. Kophazi et al. “MCNP Based Calculation of Reactivity Loss in Circulating Fuel Reactors”. In: *Proceedings of the International Conference on Nuclear Mathematical and Computational Sciences: A Century in Review-A Century Anew*. Gatlinburg, USA, 2003.
- [69] G. Lapenta, F. Mattioda, and P. Ravetto. “Point Kinetic Model for Fluid Fuel Systems”. In: *Annals of Nuclear Energy* 28 (2001), pp. 1759–1772.
- [70] F. Mattioda, P. Ravetto, and G. Ritter. “Effective Delayed Neutron Fraction for Fluid-Fuel Systems”. In: *Annals of Nuclear Energy* 27 (2000), pp. 1523–1532.
- [71] S. Kondo et al. “SIMMER-III: an Advanced Computer Program for LMFBR Severe Accident Analysis”. In: *ANP*. Tokyo, Japan, 1992.
- [72] S. Dulla, M. M. Rostagno, and P. Ravetto. “Quasi-Static Method for the Time-Dependent Neutronics of Fluid-Fuel Systems”. In: *American Nuclear Society Winter Meeting*. New Orleans, USA, 2003.
- [73] R. B. Briggs. *Molten-Salt Reactor Program Semiannual Progress Report for Period Ending July 31, 1964*. Tech. rep. ORNL-3708. Oak Ridge National Laboratory, 1964.
- [74] Ankit Rohatgi. *Webplotdigitizer: Version 4.3*. 2020. URL: <https://automeris.io/WebPlotDigitizer>.
- [75] G. D. Joanou et al. “NUCLEAR DATA FOR GAM-1 DATA TAPE. VOL-UME I”. In: (Aug. 1961). doi: [10.2172/4810176](https://doi.org/10.2172/4810176).

- [76] Massimiliano Fratoni et al. *Molten Salt Reactor Experiment Benchmark Evaluation (Project 16-10240)*. Tech. rep. DOE-UCB-8542. University of California, Berkeley, 2020.
- [77] Marco Tiberga et al. “Results from a multi-physics numerical benchmark for codes dedicated to molten salt fast reactors”. In: *Annals of Nuclear Energy* 142 (2020).
- [78] B. T. Rearden and M.A. Jessee. *SCALE Code System*. Tech. rep. ORNL/TM-2005/39. Oak Ridge National Laboratory, 2018.

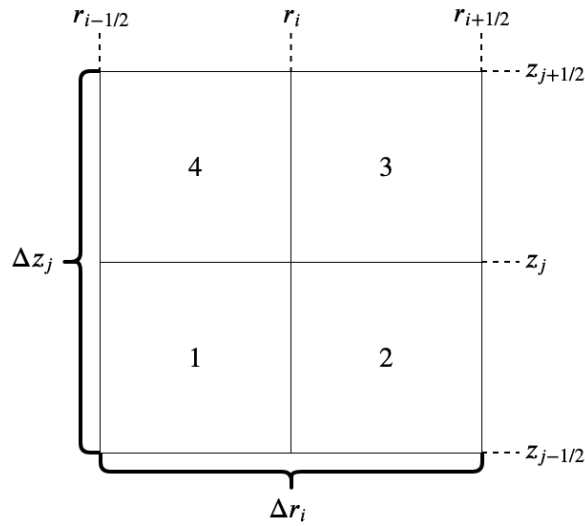
APPENDIX

A Quadrature Set

Table A.1: Level-symmetric S_{12} quadrature set in one octant.

ξ	μ	η	w
0.167213	0.167213	0.971638	0.0707626
0.167213	0.459548	0.872271	0.0558811
0.167213	0.628019	0.760021	0.0373377
0.167213	0.760021	0.628019	0.0373377
0.167213	0.872271	0.459548	0.0558811
0.167213	0.971638	0.167213	0.0707626
0.459548	0.167213	0.872271	0.0558811
0.459548	0.459548	0.760021	0.0502819
0.459548	0.628019	0.628019	0.0258513
0.459548	0.760021	0.459548	0.0502819
0.459548	0.872271	0.167213	0.0558811
0.628019	0.167213	0.760021	0.0373377
0.628019	0.459548	0.628019	0.0258513
0.628019	0.628019	0.459548	0.0258513
0.628019	0.760021	0.167213	0.0373377
0.760021	0.167213	0.628019	0.0373377
0.760021	0.459548	0.459548	0.0502819
0.760021	0.628019	0.167213	0.0373377
0.872271	0.167213	0.459548	0.0558811
0.872271	0.459548	0.167213	0.0558811
0.971638	0.167213	0.167213	0.0707626

B Simple Corner Balance



We start by integrating Eq. (3.18) over corner 1. We adopt the shorthand in Eq. (B.1).

$$\int_{r_{i-1/2}}^{r_i} dr \equiv \int_{i,1} dr, \quad \int_{z_{i-1/2}}^{z_i} dz \equiv \int_{j,1} dz \quad (\text{B.1})$$

Eq. (3.18) has been reproduced with each term colored to track where subsequent terms originate.

$$\begin{aligned} & \frac{\mu_{pq}}{r} \frac{\partial}{\partial r} (r \psi_{g,pq}) + \xi_p \frac{\partial \psi_{g,pq}}{\partial z} + \frac{\epsilon_{q+1/2}^p \psi_{g,p,q+1/2} - \epsilon_{q-1/2}^p \psi_{g,p,q-1/2}}{rw_{pq}} \\ & + \bar{\Sigma}_t \psi_{g,pq} = Q \end{aligned} \quad (\text{B.2})$$

Integrating over corner 1 we obtain

$$\begin{aligned}
& 2\pi \int_{i,1} r \int_{j,1} \frac{\mu_{pq}}{r} \frac{\partial}{\partial r} (r \psi_{g,pq}) \ dz \ dr + 2\pi \int_{i,1} r \int_{j,1} \xi_p \frac{\partial}{\partial z} \psi_{g,pq} \ dz \ dr \\
& + 2\pi \int_{i,1} r \int_{j,1} \frac{\epsilon_{q+1/2}^p \psi_{p,q+1/2} - \epsilon_{q-1/2}^p \psi_{p,q-1/2}}{rw_{pq}} \ dz \ dr \\
& + 2\pi \int_{i,1} r \int_{j,1} \bar{\Sigma}_t \psi_{p,q} \ dz \ dr = 2\pi \int_{i,1} r \int_{j,1} Q \ dz \ dr.
\end{aligned} \tag{B.3}$$

Evaluating select integrals we obtain

$$\begin{aligned}
& \mu_{pq} r_i \int_{j,1} \psi_{g,pq}(r_i, z) \ dz - \mu_{pq} r_{i-1/2} \int_{j,1} \psi_{g,pq}(r_{i-1/2}, z) \ dz \\
& + \xi_p \int_{i,1} r \psi_{g,pq}(r, z_j) \ dr - \xi_p \int_{i,1} r \psi_{g,pq}(r, z_{j-1/2}) \ dr \\
& + \int_{i,1} \int_{j,1} \frac{\epsilon_{q+1/2}^p \psi_{p,q+1/2} - \epsilon_{q-1/2}^p \psi_{p,q-1/2}}{w_{pq}} \ dz \ dr \\
& + \int_{i,1} \int_{j,1} r \bar{\Sigma}_t \psi_{p,q} \ dz \ dr = \int_{i,1} r \int_{j,1} Q \ dz \ dr.
\end{aligned} \tag{B.4}$$

We define the following surface- and volume-averaged quantities.

$$\begin{aligned}
\psi_{pqij,1W} &= \frac{\int_{j,1} \psi_{g,pq}(r_{i-1/2}, z) \ dz}{\int_{j,1} dz}, & \psi_{pqij,1E} &= \frac{\int_{j,1} \psi_{g,pq}(r_i, z) \ dz}{\int_{j,1} dz} \\
\psi_{pqij,1N} &= \frac{\int_{i,1} r \psi_{g,pq}(r, z_j) \ dr}{\int_{i,1} r \ dr}, & \psi_{pqij,1S} &= \frac{\int_{i,1} r \psi_{g,pq}(r, z_{j-1/2}) \ dr}{\int_{i,1} r \ dr} \\
\psi_{p,q+1/2,ij,1} &= \frac{\int_{i,1} \int_{j,1} \psi_{p,q+1/2} \ dz \ dr}{\int_{i,1} \int_{j,1} dz \ dr}, & \psi_{p,q-1/2,ij,1} &= \frac{\int_{i,1} \int_{j,1} \psi_{p,q-1/2} \ dz \ dr}{\int_{i,1} \int_{j,1} dz \ dr} \\
\psi_{pqij,1} &= \frac{\int_{i,1} \int_{j,1} r \psi_{pq} \ dz \ dr}{\int_{i,1} \int_{j,1} r \ dz \ dr}, & Q_{ij,1} &= \frac{\int_{i,1} r \int_{j,1} Q \ dz \ dr}{\int_{i,1} \int_{j,1} r \ dz \ dr}
\end{aligned} \tag{B.5}$$

$\psi_{pqij,1W}$, $\psi_{pqij,1E}$ and $\psi_{pqij,1N}$, $\psi_{pqij,1S}$ are the surface-averaged angular fluxes over the axial and radial faces, respectively. $\psi_{p,q+1/2,ij,1}$ and $\psi_{p,q-1/2,ij,1}$ are the volume-averaged half-angle angular fluxes. $\psi_{pqij,1}$ is the volume-averaged angular flux, and $Q_{ij,1}$ is the volume-averaged source. Note that in the above definitions we have left off the group index g in abuse of notation. Substituting these expressions we obtain Eq. (B.6).

Corner 1:

$$\begin{aligned} & \mu_{pq} r_i \frac{\Delta z_j}{2} \psi_{pqij,1E} - \mu_{pq} r_{i-1/2} \frac{\Delta z_j}{2} \psi_{pqij,1W} \\ & + \xi_p \frac{r_i^2 - r_{i-1/2}^2}{2} \psi_{pqij,1N} - \xi_p \frac{r_i^2 - r_{i-1/2}^2}{2} \psi_{pqij,1S} \\ & + \frac{\epsilon_{q+1/2}^p}{w_{pq}} \frac{\Delta z_j \Delta r_i}{4} \psi_{p,q+1/2,ij,1} - \frac{\epsilon_{q-1/2}^p}{w_{pq}} \frac{\Delta z_j \Delta r_i}{4} \psi_{p,q-1/2,ij,1} \\ & + \frac{\Delta z_j (r_i^2 - r_{i-1/2}^2)}{4} \bar{\Sigma}_{t,ij} \psi_{pqij,1} = \frac{\Delta z_j (r_i^2 - r_{i-1/2}^2)}{4} Q_{ij,1}, \end{aligned} \quad (\text{B.6})$$

where we have assumed $r_i = \frac{r_{i+1/2} + r_{i-1/2}}{2}$, $z_j = \frac{z_{j+1/2} + z_{j-1/2}}{2}$. Finally, we approximate internal surface-averaged angular fluxes, i.e. those between two corners in a cell, as the arithmetic mean of the corner fluxes on either side of the surface.

$$\begin{aligned} & \mu_{pq} r_i \frac{\Delta z_j}{2} \frac{\psi_{pqij,1} + \psi_{pqij,2}}{2} - \mu_{pq} r_{i-1/2} \frac{\Delta z_j}{2} \psi_{pqij,1W} \\ & + \xi_p \frac{r_i^2 - r_{i-1/2}^2}{2} \frac{\psi_{pqij,1} + \psi_{pqij,4}}{2} - \xi_p \frac{r_i^2 - r_{i-1/2}^2}{2} \psi_{pqij,1S} \\ & + \frac{\epsilon_{q+1/2}^p}{w_{pq}} \frac{\Delta z_j \Delta r_i}{4} \psi_{p,q+1/2,ij,1} - \frac{\epsilon_{q-1/2}^p}{w_{pq}} \frac{\Delta z_j \Delta r_i}{4} \psi_{p,q-1/2,ij,1} \\ & + \frac{\Delta z_j (r_i^2 - r_{i-1/2}^2)}{4} \bar{\Sigma}_{t,ij,1} \psi_{pqij,1} = \frac{\Delta z_j (r_i^2 - r_{i-1/2}^2)}{4} Q_{ij,1}, \end{aligned} \quad (\text{B.7})$$

Following an analogous procedure for corners 2, 3, and 4, we obtain the expressions in Eqs. (B.8), (B.9), and (B.10).

Corner 2:

$$\begin{aligned} & \mu_{pq} r_{i+1/2} \frac{\Delta z_j}{2} \psi_{pqij,2E} - \mu_{pq} r_i \frac{\Delta z_j}{2} \frac{\psi_{pqij,1} + \psi_{pqij,2}}{2} \\ & + \xi_p \frac{r_{i+1/2}^2 - r_i^2}{2} \frac{\psi_{pqij,2} + \psi_{pqij,3}}{2} - \xi_p \frac{r_{i+1/2}^2 - r_i^2}{2} \psi_{pqij,2S} \\ & + \frac{\epsilon_{q+1/2}^p}{w_{pq}} \frac{\Delta z_j \Delta r_i}{4} \psi_{p,q+1/2,ij,2} - \frac{\epsilon_{q-1/2}^p}{w_{pq}} \frac{\Delta z_j \Delta r_i}{4} \psi_{p,q-1/2,ij,2} \\ & + \frac{\Delta z_j (r_{i+1/2}^2 - r_i^2)}{4} \bar{\Sigma}_{t,ij,2} \psi_{pqij,2} = \frac{\Delta z_j (r_{i+1/2}^2 - r_i^2)}{4} Q_{ij,2}. \end{aligned} \quad (\text{B.8})$$

Corner 3:

$$\begin{aligned} & \mu_{pq} r_{i+1/2} \frac{\Delta z_j}{2} \psi_{pqij,3E} - \mu_{pq} r_i \frac{\Delta z_j}{2} \frac{\psi_{pqij,3} + \psi_{pqij,4}}{2} \\ & + \xi_p \frac{r_{i+1/2}^2 - r_i^2}{2} \psi_{pqij,3N} - \xi_p \frac{r_{i+1/2}^2 - r_i^2}{2} \frac{\psi_{pqij,2} + \psi_{pqij,3}}{2} \\ & + \frac{\epsilon_{q+1/2}^p}{w_{pq}} \frac{\Delta z_j \Delta r_i}{4} \psi_{p,q+1/2,ij,3} - \frac{\epsilon_{q-1/2}^p}{w_{pq}} \frac{\Delta z_j \Delta r_i}{4} \psi_{p,q-1/2,ij,3} \\ & + \frac{\Delta z_j (r_{i+1/2}^2 - r_i^2)}{4} \bar{\Sigma}_{t,ij,3} \psi_{pqij,3} = \frac{\Delta z_j (r_{i+1/2}^2 - r_i^2)}{4} Q_{ij,3}. \end{aligned} \quad (\text{B.9})$$

Corner 4:

$$\begin{aligned}
& \mu_{pq} r_i \frac{\Delta z_j}{2} \frac{\psi_{pqij,3} + \psi_{pqij,4}}{2} - \mu_{pq} r_{i-1/2} \frac{\Delta z_j}{2} \psi_{pqij,4W} \\
& + \xi_p \frac{r_i^2 - r_{i-1/2}^2}{2} \psi_{pqij,4N} - \xi_p \frac{r_i^2 - r_{i-1/2}^2}{2} \frac{\psi_{pqij,1} + \psi_{pqij,4}}{2} \\
& + \frac{\epsilon_{q+1/2}^p}{w_{pq}} \frac{\Delta z_j \Delta r_i}{4} \psi_{p,q+1/2,ij,4} - \frac{\epsilon_{q-1/2}^p}{w_{pq}} \frac{\Delta z_j \Delta r_i}{4} \psi_{p,q-1/2,ij,4} \\
& + \frac{\Delta z_j (r_i^2 - r_{i-1/2}^2)}{4} \bar{\Sigma}_{t,ij,4} \psi_{pqij,4} = \frac{\Delta z_j (r_i^2 - r_{i-1/2}^2)}{4} Q_{ij,4}.
\end{aligned} \tag{B.10}$$

We now define a number of matrices to combine Eqs. (B.6), (B.8), (B.9), and (B.10) in a single linear system.

Radial within-cell leakage matrix

$$\begin{aligned}
\Delta z_j r_i \begin{bmatrix} \frac{1}{2} & \frac{1}{2} & 0 & 0 \\ -\frac{1}{2} & -\frac{1}{2} & 0 & 0 \\ 0 & 0 & -\frac{1}{2} & -\frac{1}{2} \\ 0 & 0 & \frac{1}{2} & \frac{1}{2} \end{bmatrix} &= \Delta z_j \frac{r_{i+1/2} + r_{i-1/2}}{2} \begin{bmatrix} \frac{1}{2} & \frac{1}{2} & 0 & 0 \\ -\frac{1}{2} & -\frac{1}{2} & 0 & 0 \\ 0 & 0 & -\frac{1}{2} & -\frac{1}{2} \\ 0 & 0 & \frac{1}{2} & \frac{1}{2} \end{bmatrix} \\
\Delta z_j \frac{r_{i+1/2} + r_{i-1/2}}{4} &\begin{bmatrix} 1 & 1 & 0 & 0 \\ -1 & -1 & 0 & 0 \\ 0 & 0 & -1 & -1 \\ 0 & 0 & 1 & 1 \end{bmatrix}
\end{aligned}$$

We define $\gamma = \frac{r_{i-1/2}}{r_{i+1/2}}$ and recognize $r_{i+1/2}(1 + \gamma) = r_{i+1/2} + r_{i-1/2}$.

$$K_{i,j}^r = \frac{\Delta z_j r_{i+1/2}}{4} \begin{bmatrix} (1 + \gamma) & (1 + \gamma) & 0 & 0 \\ -(1 + \gamma) & -(1 + \gamma) & 0 & 0 \\ 0 & 0 & -(1 + \gamma) & -(1 + \gamma) \\ 0 & 0 & (1 + \gamma) & (1 + \gamma) \end{bmatrix} \quad (\text{B.11})$$

Axial within-cell leakage matrix

$$\frac{1}{2} \begin{bmatrix} r_i^2 - r_{i-1/2}^2 & 0 & 0 & r_i^2 - r_{i-1/2}^2 \\ 0 & r_{i+1/2}^2 - r_i^2 & r_{i+1/2}^2 - r_i^2 & 0 \\ 0 & -(r_{i+1/2}^2 - r_i^2) & -(r_{i+1/2}^2 - r_i^2) & 0 \\ -(r_i^2 - r_{i-1/2}^2) & 0 & 0 & -(r_i^2 - r_{i-1/2}^2) \end{bmatrix}$$

We can simplify with some rearrangement.

$$\begin{aligned} r_i^2 - r_{i-1/2}^2 &= \left(\frac{r_{i+1/2} + r_{i-1/2}}{2} \right)^2 - r_{i-1/2}^2 \\ &= \frac{r_{i+1/2}^2 + 2r_{i+1/2}r_{i-1/2} + r_{i-1/2}^2}{4} - r_{i-1/2}^2 \\ &= \frac{r_{i+1/2}^2 + 2r_{i+1/2}r_{i-1/2} - 3r_{i-1/2}^2}{4} \\ &= \frac{(r_{i+1/2} - r_{i-1/2})(r_{i+1/2} + 3r_{i-1/2})}{4} \\ &= \frac{\Delta r_i r_{i+1/2}}{4} (1 + 3\gamma) \end{aligned}$$

$$\begin{aligned}
r_{i+1/2}^2 - r_i^2 &= r_{i+1/2}^2 - \left(\frac{r_{i+1/2} + r_{i-1/2}}{2} \right)^2 \\
&= r_{i+1/2}^2 - \frac{r_{i+1/2}^2 + 2r_{i+1/2}r_{i-1/2} + r_{i-1/2}^2}{4} \\
&= \frac{3r_{i+1/2}^2 - 2r_{i+1/2}r_{i-1/2} - r_{i-1/2}^2}{4} \\
&= \frac{(r_{i+1/2} - r_{i-1/2})(3r_{i+1/2} + r_{i-1/2})}{4} \\
&= \frac{\Delta r_i r_{i+1/2}}{4}(3 + \gamma)
\end{aligned}$$

Substitution produces

$$K_{i,j}^z = \frac{\Delta r_i r_{i+1/2}}{8} \begin{bmatrix} 1 + 3\gamma & 0 & 0 & 1 + 3\gamma \\ 0 & 3 + \gamma & (3 + \gamma) & 0 \\ 0 & -(3 + \gamma) & -(3 + \gamma) & 0 \\ -(1 + 3\gamma) & 0 & 0 & -(1 + 3\gamma) \end{bmatrix} \quad (\text{B.12})$$

Radial out-of-cell leakage matrix

$$L_{i,j}^r = \Delta z_j r_{i+1/2} \begin{bmatrix} -\gamma & 0 & 0 & 0 \\ 0 & 1 & 0 & 0 \\ 0 & 0 & 1 & 0 \\ 0 & 0 & 0 & -\gamma \end{bmatrix} \quad (\text{B.13})$$

Axial out-of-cell leakage matrix

$$L_{i,j}^z = \frac{\Delta r_i r_{i+1/2}}{4} \begin{bmatrix} -(1 + 3\gamma) & 0 & 0 & 0 \\ 0 & -(3 + \gamma) & 0 & 0 \\ 0 & 0 & 3 + \gamma & 0 \\ 0 & 0 & 0 & 1 + 3\gamma \end{bmatrix} \quad (\text{B.14})$$

Collision matrix

$$T_{i,j} = \frac{\Delta r_i \Delta z_j r_{i+1/2}}{8} \begin{bmatrix} 1 + 3\gamma & 0 & 0 & 0 \\ 0 & 3 + \gamma & 0 & 0 \\ 0 & 0 & 3 + \gamma & 0 \\ 0 & 0 & 0 & 1 + 3\gamma \end{bmatrix} \quad (\text{B.15})$$

Angular redistribution matrix

$$R_{i,j} = \frac{\Delta r_i \Delta z_j}{2} \begin{bmatrix} 1 & 0 & 0 & 0 \\ 0 & 1 & 0 & 0 \\ 0 & 0 & 1 & 0 \\ 0 & 0 & 0 & 1 \end{bmatrix} \quad (\text{B.16})$$

We now formulate the linear system relating the angular fluxes of cell (i, j) .

$$\begin{aligned}
 & \mu_{p,q} L_{i,j}^r \begin{bmatrix} \psi_{pqij,1W} \\ \psi_{pqij,2E} \\ \psi_{pqij,3E} \\ \psi_{pqij,4W} \end{bmatrix} + \xi_p L_{i,j}^z \begin{bmatrix} \psi_{pqij,1S} \\ \psi_{pqij,2S} \\ \psi_{pqij,3N} \\ \psi_{pqij,4N} \end{bmatrix} + R_{i,j} \frac{\alpha_{q+1/2}^p \begin{bmatrix} \psi_{p,q+1/2,ij,1} \\ \psi_{p,q+1/2,ij,2} \\ \psi_{p,q+1/2,ij,3} \\ \psi_{p,q+1/2,ij,4} \end{bmatrix} - \alpha_{q-1/2}^p \begin{bmatrix} \psi_{p,q-1/2,ij,1} \\ \psi_{p,q-1/2,ij,2} \\ \psi_{p,q-1/2,ij,3} \\ \psi_{p,q-1/2,ij,4} \end{bmatrix}}{w_{pq}} \\
 & + [\mu_{p,q} K_{i,j}^r + \xi_p K_{i,j}^z + \bar{\Sigma}_t T_{i,j}] \begin{bmatrix} \psi_{pqij,1} \\ \psi_{pqij,2} \\ \psi_{pqij,3} \\ \psi_{pqij,4} \end{bmatrix} = \frac{1}{4\pi} T_{i,j} \begin{bmatrix} Q_{pqij,1} \\ Q_{pqij,2} \\ Q_{pqij,3} \\ Q_{pqij,4} \end{bmatrix}
 \end{aligned} \tag{B.17}$$

The out-of-cell leakage fluxes are determined by Eq. (3.32).

C Starting Angle Operators

The 4×4 linear operators for the starting angle equation are shown below.

Radial within-cell leakage matrix

$$K_{i,j}^r = \frac{\Delta z_j r_{i+1/2}}{4} \begin{bmatrix} -(1 + \gamma) & -(1 + \gamma) & 0 & 0 \\ (1 + \gamma) & (1 + \gamma) & 0 & 0 \\ 0 & 0 & (1 + \gamma) & (1 + \gamma) \\ 0 & 0 & -(1 + \gamma) & -(1 + \gamma) \end{bmatrix} \quad (\text{C.1})$$

Axial within-cell leakage matrix

$$K_{i,j}^z = \frac{\Delta r_i r_{i+1/2}}{8} \begin{bmatrix} 1 + 3\gamma & 0 & 0 & 1 + 3\gamma \\ 0 & 3 + \gamma & 3 + \gamma & 0 \\ 0 & -(3 + \gamma) & -(3 + \gamma) & 0 \\ -(1 + 3\gamma) & 0 & 0 & -(1 + 3\gamma) \end{bmatrix} \quad (\text{C.2})$$

Radial out-of-cell leakage matrix

$$L_{i,j}^r = \Delta z_j r_{i+1/2} \begin{bmatrix} \gamma & 0 & 0 & 0 \\ 0 & -1 & 0 & 0 \\ 0 & 0 & -1 & 0 \\ 0 & 0 & 0 & \gamma \end{bmatrix} \quad (\text{C.3})$$

Axial out-of-cell leakage matrix

$$L_{i,j}^z = \frac{\Delta r_i r_{i+1/2}}{4} \begin{bmatrix} -(1 + 3\gamma) & 0 & 0 & 0 \\ 0 & -(3 + \gamma) & 0 & 0 \\ 0 & 0 & 3 + \gamma & 0 \\ 0 & 0 & 0 & 1 + 3\gamma \end{bmatrix}$$

First collision matrix

$$T_{i,j}^1 = \frac{\Delta r_i \Delta z_j r_{i+1/2}}{8} \begin{bmatrix} 1 + 3\gamma & 0 & 0 & 0 \\ 0 & 3 + \gamma & 0 & 0 \\ 0 & 0 & 3 + \gamma & 0 \\ 0 & 0 & 0 & 1 + 3\gamma \end{bmatrix}$$

Second collision matrix

$$T_{i,j}^2 = \frac{\Delta r_i \Delta z_j}{2} \begin{bmatrix} 1 & 0 & 0 & 0 \\ 0 & 1 & 0 & 0 \\ 0 & 0 & 1 & 0 \\ 0 & 0 & 0 & 1 \end{bmatrix}$$

We now formulate the linear system relating the half-angle fluxes of cell (i, j) .

$$\begin{aligned} & \sqrt{(1 - \xi_p^2)} L_{i,j}^r \begin{bmatrix} \psi_{pqij,1W} \\ \psi_{pqij,2E} \\ \psi_{pqij,3E} \\ \psi_{pqij,4W} \end{bmatrix} + \xi_p L_{i,j}^z \begin{bmatrix} \psi_{pqij,1S} \\ \psi_{pqij,2S} \\ \psi_{pqij,3N} \\ \psi_{pqij,4N} \end{bmatrix} \\ & + \left[\sqrt{(1 - \xi_p^2)} K_{i,j}^r + \xi_p K_{i,j}^z + \bar{\Sigma}_t T_{i,j}^1 + \sqrt{(1 - \xi_p^2)} T_{i,j}^2 \right] \begin{bmatrix} \psi_{pqij,1} \\ \psi_{pqij,2} \\ \psi_{pqij,3} \\ \psi_{pqij,4} \end{bmatrix} = T_{i,j}^1 \begin{bmatrix} Q_{pqij,1} \\ Q_{pqij,2} \\ Q_{pqij,3} \\ Q_{pqij,4} \end{bmatrix} \end{aligned}$$

The out-of-cell leakage fluxes are determined by Eq. (3.37).

D Group Constant Generation with SCALE

One of the SCALE input files used to generate the two-group constants used in Sections 4.2 and 4.4 is shown in Listing D.1. It describes a rectangular area composed of graphite containing fuel and control material regions. The sizes of these regions were determined so as to approximate material volume fractions of the MSRE. Group constants at other temperatures were generated by modifying the fuel and moderator temperatures and densities. Listing D.1 is largely derived from a SCALE presented by Lindsay et al. [34]. Details on input syntax can found in Rearden and Jessee [78].

Listing D.1: SCALE input to generate MSRE group constants at 922 K used by QuasiMolto

```
=t-newt
MSRE
v7-238
read comp
,          Fuel
li -7      1      DEN=2.146      .1090    922      end
li -6      1      DEN=2.146      5e-6     922      end
f -19      1      DEN=2.146      .6680    922      end
be -9      1      DEN=2.146      .0627    922      end
u -235     1      DEN=2.146      .0167    922      end
u -238     1      DEN=2.146      .0344    922      end
,          Moderator
c -12      2      DEN=1.8600    1        922      end
,          Control
gd2o3      3      DEN=5.873      0.70    922      end
ATOM-a2o3  3      5.873 2 13027 2 8016 3 0.30 922  end
end comp

read celldata
latticecell squarepitch pitch=5 2 fuelr=1.33809 1 end
end celldata

read model
read parm
```

```
solntype=b1
collapse=yes
' prt broad=yes
prt mxsec=yes
end parm

read homog
1000 fuel 1 end
2000 mod 2 end
3000 control 3 end
end homog

read materials
mix=2 pn=2 end
mix=1 pn=1 end
mix=3 pn=1 end
end materials

read collapse 199r1 39r2 end collapse

read geom
global unit 10
cylinder 11 1.33809 origin x=2.5 y=2.5
cylinder 13 0.08 origin x=0.5 y=2.5
cuboid 12 5 0 5 0
media 1 1 11
media 2 1 12 -11 -13
media 3 1 13
boundary 12 30 30
end geom

read bounds
all=refl
end bounds

end model
end
```

E QD Boundary Conditions with P₁ Approximation

The QD boundary conditions are

$$\hat{n} \cdot \mathbf{J}|_{(r,z) \in \delta D} = \begin{cases} [\mathbb{C}(\phi - \phi^{\text{in}}) + J^{\text{in}}], & r \neq 0 \\ 0, & r = 0 \end{cases}, \quad (\text{E.1})$$

where

$$\mathbb{C} = \frac{\int_{\hat{n} \cdot \hat{\Omega} > 0} \hat{n} \cdot \hat{\Omega} \psi d\hat{\Omega}}{\int_{\hat{n} \cdot \hat{\Omega} > 0} \psi d\hat{\Omega}}, \quad (\text{E.2a})$$

$$\phi^{\text{in}} = \int_{\hat{n} \cdot \hat{\Omega} < 0} \psi d\hat{\Omega}, \quad (\text{E.2b})$$

$$J^{\text{in}} = \int_{\hat{n} \cdot \hat{\Omega} < 0} \hat{n} \cdot \hat{\Omega} \psi d\hat{\Omega}. \quad (\text{E.2c})$$

The P₁, i.e. diffusion, approximation to the angular flux is given in Eq. (E.3).

$$\psi \approx \frac{1}{4} \left(\phi + 3 \left(\hat{\Omega}_r J_r + \hat{\Omega}_z J_z + + \hat{\Omega}_\gamma J_\gamma \right) \right), \quad (\text{E.3})$$

where $(\hat{\Omega}_r, \hat{\Omega}_\gamma, \hat{\Omega}_z) = (\mu, \eta, \xi) = (\sin(\gamma) \cos(\omega), \sin(\gamma) \sin(\omega), \cos(\gamma))$. The angles γ and ω are shown in Figure 3.1. Substituting the P₁ approximation into the expression for the boundary conditions yields expressions independent of the MGHOT solution.

Top boundary Evaluating \mathbb{C} at the top boundary yields

$$\mathbb{C}(r, z = Z) = \frac{\int_0^{\pi/2} \int_0^{2\pi} \hat{\Omega}_z \left(\phi + 3 \hat{\Omega}_z J_z \right) d\hat{\Omega}}{\int_0^{\pi/2} \int_0^{2\pi} \left(\phi + 3 \hat{\Omega}_z J_z \right) d\hat{\Omega}}, \quad (\text{E.4})$$

$$\mathbb{C}(r, z = Z) = \frac{\int_0^{\pi/2} \int_0^{2\pi} \cos(\gamma) (\phi + 3 \cos(\gamma) J_z) \sin(\gamma) d\gamma d\omega}{\int_0^{\pi/2} \int_0^{2\pi} (\phi + 3 \cos(\gamma) J_z) \sin(\gamma) d\gamma d\omega}, \quad (\text{E.5})$$

$$\mathbb{C}(r, z = Z) = \frac{\frac{1}{2}\phi + J_z}{\phi + \frac{3}{2}J_z}. \quad (\text{E.6})$$

Substituting this expression for \mathbb{C} , assuming $\phi^{\text{in}} = J^{\text{in}} = 0$, and recognizing that $J_z(r, z = 0) > 0$ for a vacuum boundary yields

$$J_z \left(\phi + \frac{3}{2}J_z \right) = \phi \left(\frac{1}{2}\phi + J_z \right), \quad (\text{E.7})$$

$$J_z(r, z = Z) = \frac{1}{\sqrt{3}} \phi(r, z = Z). \quad (\text{E.8})$$

Bottom boundary Evaluating \mathbb{C} at the bottom boundary yields

$$\mathbb{C}(r, z = 0) = \frac{-\int_{\pi/2}^{\pi} \int_0^{2\pi} \hat{\Omega}_z \left(\phi + 3 \hat{\Omega}_z J_z \right) d\hat{\Omega}}{\int_{\pi/2}^{\pi} \int_0^{2\pi} \left(\phi + 3 \hat{\Omega}_z J_z \right) d\hat{\Omega}}, \quad (\text{E.9})$$

$$\mathbb{C}(r, z = 0) = \frac{-\int_{\pi/2}^{\pi} \int_0^{2\pi} \cos(\gamma) (\phi + 3 \cos(\gamma) J_z) \sin(\gamma) d\gamma d\omega}{\int_{\pi/2}^{\pi} \int_0^{2\pi} (\phi + 3 \cos(\gamma) J_z) \sin(\gamma) d\gamma d\omega}, \quad (\text{E.10})$$

$$\mathbb{C}(r, z = 0) = \frac{\frac{1}{2}\phi - J_z}{\phi - \frac{3}{2}J_z} \quad (\text{E.11})$$

Substituting this expression for \mathbb{C} , assuming $\phi^{\text{in}} = J^{\text{in}} = 0$, and recognizing that $J_z(r, z = 0) < 0$ for a vacuum boundary yields

$$-J_z(\phi - \frac{3}{2}J_z) = \phi(\frac{1}{2}\phi - J_z), \quad (\text{E.12})$$

$$J_z(r, z = 0) = -\frac{1}{\sqrt{3}}\phi(r, z = 0). \quad (\text{E.13})$$

Outside boundary: $r = R$ Evaluating \mathbb{C} at the outside boundary yields

$$\mathbb{C}(r = R, z) = \frac{\int_0^\pi \int_{-\pi/2}^{\pi/2} \hat{\Omega}_r (\phi + 3\hat{\Omega}_r J_r) d\hat{\Omega}}{\int_0^\pi \int_{-\pi/2}^{\pi/2} (\phi + 3\hat{\Omega}_r J_r) d\hat{\Omega}}, \quad (\text{E.14})$$

$$\mathbb{C}(r = R, z) = \frac{\int_0^\pi \int_{-\pi/2}^{\pi/2} \sin(\gamma) \cos(\omega) (\phi + 3\sin(\gamma) \cos(\omega) J_r) \sin(\gamma) d\gamma d\omega}{\int_0^\pi \int_{-\pi/2}^{\pi/2} (\phi + 3\sin(\gamma) \cos(\omega) J_r) \sin(\gamma) d\gamma d\omega}, \quad (\text{E.15})$$

$$\mathbb{C}(r = R, z) = \frac{\frac{1}{2}\phi + J_r}{\phi + \frac{3}{2}J_r} \quad (\text{E.16})$$

Substituting this expression for \mathbb{C} , assuming $\phi^{\text{in}} = J^{\text{in}} = 0$, and recognizing that $J_r(r = R, z) > 0$ for a vacuum boundary yields

$$J_r(\phi - \frac{3}{2}J_r) = \phi(\frac{1}{2}\phi - J_r), \quad (\text{E.17})$$

$$J_r(r = R, z) = \frac{1}{\sqrt{3}}\phi(r = R, z). \quad (\text{E.18})$$

